EFFICIENT LIGHT COUPLING FOR GRATING CAVITY USING ARSENIC TRISULFIDE GRATING COUPLER

A Dissertation

by

CHEN ZHANG

Submitted to the Office of Graduate and Professional Studies of
Texas A&M University
in partial fulfillment of the requirements for the degree of

DOCTOR OF PHILOSOPHY

Chair of Committee,	Christi K. Madsen
Committee Members,	Ohannes Eknoyan
	Jim Ji
	Alexey Belyanin
Head of Department,	Miroslav M. Begovic

May 2017

Major Subject: Electrical Engineering

ABSTRACT

In this dissertation, design, fabrication and measurement of arsenic trisulfide (As_2S_3) grating couplers have been demonstrated on both bulk lithium niobate ($LiNbO_3$) substrate and thin film $LiNbO_3$. Photonic design tools, including Fimmwave and Fimmprop, are used for optical modelling. Python scripts are used to optimize the results. Standard semiconductor processing techniques are employed to fabricate the proposed grating couplers. In particular, electron beam lithography (EBL) is used to pattern sub-micron fine features in these grating couplers. The grating couplers are measured using an optical vector analyzer.

As_2S_3 grating coupler on bulk $LiNbO_3$ substrate has a theoretical coupling loss of 2.55 dB, while the measured coupling loss is 3.75 dB. The bandwidth of this coupler is 80 nm. The reason for the measured loss being higher than the theoretical value is fabrication imperfection. As_2S_3 grating coupler on thin film $LiNbO_3$ has a theoretical coupling efficiency as high as 78.8% after optimization. A simplified grating coupler structure on thin film $LiNbO_3$ is fabricated and measured, with 6.3 dB coupling loss. Reflection response of a grating cavity is measured by this coupler. The fitted result shows 2.0 dB/cm propagation loss of the As_2S_3 cavity waveguide. If the cavity waveguide width is tapered to 0.4 μm, 82.3% of light can be confined in the $LiNbO_3$ layer. This high optical mode confinement factor in $LiNbO_3$, together with the excellent electro-optic (EO) property of $LiNbO_3$ crystal, makes such a grating cavity a promising high-speed, low-loss tunable filter.

An optical low-coherence interferometer (OLCI) setup is designed and built. The low-coherence source is generated by a supercontinuum source with a bandpass filter. Interference fringes occur when one of the arms includes a variable delay line. By Fourier transform of the fringes, the spectral density of the source is obtained and analyzed. The setup has been tested in the near-infrared wavelength range, and it can also be used to characterize mid-infrared optical passive devices.

DEDICATION

To my family

ACKNOWLEDGEMENTS

I would like to express deep gratitude to my committee chair Dr. Christi K. Madsen, for her guidance and encouragement. I would like to thank other committee members, Dr. Ohannes Eknoyan, Dr. Jim Ji and Dr. Alexey Belyanin, for their valuable advice on my research projects.

I would also like to thank Aggiefab staff, Larry Rehn, Robert Atkins, Jim Gardner and Dennie Spears for providing high-standard technical support.

Thanks also go to my current and former colleagues, Dwayne Macik, Yuan Bao, Dr. Yifeng Zhou, Dr. Xin Wang, Dr. Qi Chen, Dr. Jae Kim, Dr. Yuxiao Liu and Dr. Ran Huang.

I also want to extend my gratitude to Dr. Long Chang from Nanofabrication Facilities of University of Houston, for his fruitful discussion and valuable advice on EBL fabrication process.

I would acknowledge my funding agency MIRTHE for their financial support throughout my PhD study.

Finally, special thanks to my family and girlfriend for their love and support.

NOMENCLATURE

PIC	Photonic Integrated Circuit
WDM	Wavelength-Division Multiplexing
SOI	Silicon on Insulator
EO	Electro-Optic
IR	InfRared
DUT	Device-Under-Test
SMF	Single-Mode Fiber
MFD	Mode-Field Diameter
RIE	Reactive Ion Etching
DC	Duty Cycle
EIM	Effective Index Method
CMT	Coupled-Mode Theory
TMM	Transfer Matrix Method
FP	Fabry-Perot
OLCI	Optical Low-Coherence Interferometry
PECVD	Plasma-Enhanced Chemical Vapor Deposition
EBL	Electron Beam Lithography
PMMA	PolyMethyl MethAcrylate
MW	Molecular Weight
DOE	Design Of Experiments

FC	Faraday Cup
SEM	Scanning Electron Microscope
BOX	Buffer OXide
OVA	Optical Vector Analyzer
FWHM	Full Width at Half Maximum
FSR	Free Spectral Range
BCB	BenzoCycloButene
CPI	Common Path Interferometer
MZI	Mach-Zehnder Interferometer
APE	Annealed Proton Exchanged
FDM	Finite Difference Method
SOP	State Of Polarization
DFB	Distributed Feedback
PC	Polarization Controller
OSA	Optical Spectrum Analyzer
MUX	Multiplexer
DMUX	Demultiplexer
PD	PhotoDetector
ND	Neutral Density

CONTRIBUTORS AND FUNDING SOURCES

Contributors

This work was supervised by a dissertation committee consisting of Professor Christi K. Madsen, Professor Ohannes Eknoyan and Professor Jim Ji of the Department of Electrical and Computer Engineering, and Professor Alexey Belyanin of the Department of Physics and Astronomy.

All the work conducted for the dissertation was completed by the student independently.

Funding Sources

Graduate study was supported by Mid-infrared Technologies for Health and the Environment (MIRTHE).

TABLE OF CONTENTS

Page

ABSTRACT ii

DEDICATION iv

ACKNOWLEDGEMENTS v

NOMENCLATURE vi

CONTRIBUTORS AND FUNDING SOURCES viii

TABLE OF CONTENTS ix

LIST OF FIGURES xi

LIST OF TABLES xvi

CHAPTER I INTRODUCTION 1

1.1 Background 1
1.2 As_2S_3-on-$LiNbO_3$ platform 2
1.3 Light coupling for As_2S_3-on-$LiNbO_3$ platform 4
1.4 Review of the development of grating coupler 5
1.5 Motivations 6
1.6 Thesis organization 7

CHAPTER II THEORETICAL REVIEW* 8

2.1 Optics basics 8
2.2 Building blocks for integrated photonic design 12
2.3 Optical low-coherence interferometry 23

CHAPTER III FABRICATION PROCESS 26

3.1 Thin film preparation 26
3.2 Lithography 27

CHAPTER IV RESULTS AND DISCUSSION* 50

4.1 As_2S_3-on-$LiNbO_3$ grating coupler 50

Page

4.2 As_2S_3 grating coupler on thin film $LiNbO_3$ 61
4.3 Electro-optic probe for electric field measurement 77
4.4 OLCI setup for measurement on As_2S_3-on-$LiNbO_3$ platforms 97

CHAPTER V CONCLUSION 101

5.1 Summary 101
5.2 Future works 103

REFERENCES 105

APPENDIX A MATLAB CODE FOR EIM 113

APPENDIX B PYTHON SCRIPT INTERFACING WITH FIMMPROP 120

APPENDIX C EBL STEP-BY-STEP PROCEDURE 127

LIST OF FIGURES

Page

Fig. 1. As_2S_3 material dispersion. 9

Fig. 2. The cross sections of (A) slab waveguide, (B) rib waveguide, (C) ridge waveguide, and (D) cylinder waveguide. 9

Fig. 3. Generic grating coupler structure: (A) the top view; (B) the side view. The yellow color labels the substrate and the red color labels the grating material. 13

Fig. 4. The Side view illustration of how grating coupler works as an output port. 14

Fig. 5. The grating period vs. grating fill factor, at different values of waveguide thickness 15

Fig. 6. Partially etched grating coupler can reduce back reflection. 17

Fig. 7. Sidewall Bragg grating parameters. 17

Fig. 8. A grating cavity device. 20

Fig. 9. Effective refractive indices for different waveguide widths. 21

Fig. 10. Transmission spectra of sidewall Bragg gratings with different grating depths. 22

Fig. 11. The grating cavity response (blue) and the EO-tuned response (red). 23

Fig. 12. Configuration of an optical low-coherence interferometry. MUX: multiplexer; DMUX: demultimpexer; PD: photodetector; DUT: device under test. 24

Fig. 13. Hierarchical mask design example. (A) Component level: Apodized grating coupler; (B) Device level: grating coupler device with taper; (C) Chip level. 29

Fig. 14. Touch screen of the E-beam system 32

Fig. 15. Chamber pressure gauge rod position when (A) VG1>3×10^{-4} Pa; and (B) VG1<=3×10^{-4} Pa. 33

Page

Fig. 16. The picture of (1) the aperture-switching knob, (2)(3) lens translation knobs. The current setting is at aperture 2 (A2). 34

Fig. 17. SE image of BE mark. The bright cross is the BE mark, while the red lines are the center lines of the screen. 36

Fig. 18. Auto-calibration pop-up window. If it is the first calibration attempt, "automatic focusing" and "AE mark detection" also need to be checked in order for the system to decide the rough focus point. 37

Fig. 19. The pop-up window for std mark detection for alignment. "Std Mark Detection", "User mark detection" should be checked, and the stage coordinates of mark P should be typed in. 39

Fig. 20. The pop-up window for RG mark detection for alignment. "RG Mark Detection", "Auto update" should be checked, and P & Q coordinates should be typed in. 40

Fig. 21. Height difference between the AE, BE marks and the sample surface. The red dashed line shows the height level of the marks. 41

Fig. 22. Exposure window 43

Fig. 23. Job property and shotrank table. 45

Fig. 24. Stitching error due to missing the step of deflection correction after focus adjustment 46

Fig. 25. Stitching error caused by the stage error. 47

Fig. 26. The microscope image shows Ti liftoff incomplete. 48

Fig. 27. Pattern changed due to RIE. 49

Fig. 28. (A) Bragg gratings device configuration; (B) Zoom-in view inside dashed box, with grating coupler and taper parameters. 50

Fig. 29. Vertical coupling through grating coupler (side view). 51

Fig. 30. Electric field (Ex) plots of grating coupler (A) without Bragg reflector, and (B) with Bragg reflector. 52

Fig. 31. SEM images of (A) grating coupler; (B) grating coupler zoom-in; (C) sidewall Bragg grating; (D) Bragg grating zoom-in. 55

Page

Fig. 32. Microscope images of device with different RIE time (A) 4+1min; (B) 4+1+1+1min; (C) 4+1+1+1+1min; (D) (4+1+1+1+1) min+45s. 56

Fig. 33. Fabrication steps for the proposed device. 57

Fig. 34. Grating coupler measurement setup. 57

Fig. 35. (A) TE transmission response of the grating couplers; (B) Zoomed-in fringes at 1560-1565 nm. 58

Fig. 36. Reflection spectra and fitted curves for grating depths of (A) 400nm, and (B) 500nm. 59

Fig. 37. (A) Grating cavity transmission spectrum; (B) grating cavity reflection spectrum (blue) and fitted curve (red). 60

Fig. 38. Material stack of the thin film $LiNbO_3$ wafer. 63

Fig. 39. Two As_2S_3-on-$LiNbO_3$ film designs: (A) design 1; (B) design 2. 64

Fig. 40. Ex at 1550 nm for design 1. 65

Fig. 41. Coupling efficiency variation with different BOX thicknesses. 66

Fig. 42. Grating coupling efficiency with reflector and without reflector. 67

Fig. 43. The material stack for: (A) design 3; and (B) design 4. 69

Fig. 44. Fabrication of grating coupler design 1 (side view). 71

Fig. 45. Small sample mounted on EBL cassette. 72

Fig. 46. (A) The sample is mounted to the carrier substrate; (B) liftoff. 72

Fig. 47. Fabrication of grating coupler design 3 (side-view). 73

Fig. 48. Measurement of the thin film $LiNbO_3$ chip. 73

Fig. 49. Insertion loss of design 3 grating couplers with different lengths of As_2S_3 waveguides. 74

Fig. 50. (A) Reflected spectrum of a fabricated grating cavity device; (B) Zoom-in view. 75

Page

Fig. 51. Effective refractive index and confinement factor of the hybrid optical mode is changed with the change of As_2S_3 waveguide width. 76

Fig. 52. (a) TE fundamental mode; (b) TM fundamental mode. 78

Fig. 53. The geometry of the Ti-diffused CPI senor. 79

Fig. 54. Electric field contour solved by the EO solver. 79

Fig. 55. Ti-diffused sensor fabrication steps. 81

Fig. 56. Ti-diffused CPI sensor setup. 81

Fig. 57. As_2S_3-on-thin film $LiNbO_3$ hybrid mode. 83

Fig. 58. Two possible geometries of the hybrid EO waveguide structures. 84

Fig. 59. Transmission with different phase mismatch values. 88

Fig. 60. Initial D-fiber packaging attempt. 89

Fig. 61. Transmission spectra for different D-fiber LN slab coupling measurements. 90

Fig. 62. Tranmission spectrum and its linear region. 91

Fig. 63. Packaging of D-fiber LN slab coupler. 93

Fig. 64. Optical coupling region of the probe after packaging. 94

Fig. 65. Optical measurement of the probe with DFB laser and OSA. 94

Fig. 66. Normalized insertion loss with tunable laser, OVA, and DFB laser. 96

Fig. 67. Zoomed-in of tuning range of the DFB laser measurement, in linear scale. 97

Fig. 68. Low coherence source generation. 97

Fig. 69. Optical spectrum analyzer results: (A) with and without the ND filter; (B) with and without the bandpass filter. 98

Fig. 70. (A) Fringe patterns of the low-coherent light, and (B) measured and extracted source spectrum with bandpass filter. 99

Page

Fig. 71. Experimental measurements of a bandpass filter near 1550 nm: (A) phase response and (B) group delay. 100

LIST OF TABLES

Page

Table 1. Different thin film preparation methods. 26

Table 2. Different patterning technologies and their capabilities. 28

Table 3. Key parameters for both lithography modes. 33

Table 4. Field size and scan clock change.....42

Table 5. Optimized grating coupler parameters. 53

Table 6. Comparison of different methods to create thin film $LiNbO_3$. 63

Table 7. Comparison between design 1 and design 2. 68

Table 8. Grating coupler parameters for design 3. 69

Table 9. Fabrication cost vs. efficiency for all the designs. 70

Table 10. Fitting parameters for the grating cavity reflection response. 75

Table 11. Sensor parameters comparison among different design methods. 85

Table 12. Comparison among different sensors. 88

CHAPTER I

INTRODUCTION

1.1 Background

Information exchange is in constant demand in human society. The traditional way for data communication is to use coaxial cable to transfer low-frequency signals. In 1966, Dr. Charles K. Kao made a visionary statement that optical fiber would become a new form of communication medium, and he was awarded Nobel Prize in Physics [1]. Dr. Kao's achievement brought significant attention to optical communication. The advantages of optical communication over traditional low-frequency data communication include higher bandwidth, higher stability and lower cost.

At the nodes of an optical communication system, optical data need to be processed. The traditional method is to convert the optical signal into electrical signal, followed by the traditional electrical signal processing. While the electrical signal processing components are well developed, this method adds to the system cost, especially for long-distance data transfer where more nodes are involved.

On the other hand, all-optical signal processing is feasible because the optical signals do not need to be converted to the electrical signals [2]. Optical components are developed to meet the need for the optical communication systems. Photonic integrated circuit (PIC) is the integration of photonic components , first brought up by Millar in 1969 [3]. On one photonic chip, multi-functional modules are integrated, laying solid hardware foundation for optical communication.

In optical communication system, the analysis is often based on the wavelength domain of the signal. Optical filter is one of the key components for all-optical signal processing at wavelength domain. The function of an optical filter in general is to let some wavelengths pass and to reject the other wavelengths. There are various types of filters including low-pass filter, band-pass filter, high-pass filter, band-rejection filter and all-pass filter.

The most common application for the optical filters is wavelength-division multiplexing (WDM) system. In WDM system, the signals from different wavelengths regions (or channels) are combined at the signal generation terminal, and are separated at the signal receiving terminal. In order to separate closely-spaced channels without signal distortion, filters with high extinction ratio and a certain bandwidth are required.

Filters are constructed by optical interference. By introducing an optical phase change in one of the interference terms, the resonance wavelength of the filter can be shifted. This is the basic idea of tunable filter, and it has very promising applications such as imaging spectroscopy [4], gas sensing [5], and beam steering [6-8].

1.2 As_2S_3-on-$LiNbO_3$ platform

As the development of the photonics technologies keeps going, multiple photonic platforms start to show their respective advantages over the others. Silicon on insulator (SOI) platform has the most developed fabrication technologies. III-V semiconductor platform offers the capability of the integration of light source on chip and offers varieties of compounds. Lithium niobate ($LiNbO_3$) platform is advantageous when it

comes to high-speed electro-optic (EO) modulation. One needs to choose the right platform according to the specific application.

Arsenic trisulfide (As_2S_3) waveguide on $LiNbO_3$ substrate is a hybrid platform for both near-infrared (near-IR) and mid-infrared (mid-IR) applications. As_2S_3 is an amorphous chalcogenide material, which exhibits good optical properties in the infrared regime. The transparent window of As_2S_3 is 0.2 – 11 μm [9], enabling most of the near-IR and mid-IR applications. The nonlinear refractive index of As_2S_3 is two orders of magnitude greater than that of silica (SiO_2) [10], making it an ideal material for self-phase modulation applications. The third-order optical nonlinear susceptibility ($\chi 3$) of As_2S_3 is two orders of magnitude greater than that of SiO_2 [10], meaning that it is a good candidate for four wave mixing (FWM) wavelength conversion [11-13]. Additionally, standard semiconductor fabrication techniques can be applied to As_2S_3 patterning: As_2S_3 can be deposited using magnetron sputtering in a controlled manner [14], and it can be reactive ion etched [15].

$LiNbO_3$ serves as the substrate in this platform for the following reasons. First, $LiNbO_3$ has excellent EO property, with the maximum EO coefficient to be 30.8pm/V on z-axis [16]. This EO property has been used extensively in high-speed modulators and phased arrays [17, 18]. Second, the transparent window of $LiNbO_3$ is 0.35 – 5.0 μm [19], covering a good portion of mid-IR spectrum. $LiNbO_3$ is a birefringence crystal. At 1550nm, the ordinary refractive index is 2.21 and the extraordinary refractive index is 2.14 [20]. Third, low-loss channel waveguides can be fabricated through a titanium (Ti) thermal diffusion process or a proton exchange process. The resulting waveguide have a

similar mode size as standard single-mode fiber (SMF), rendering a potential coupling loss below 1 dB between the waveguide and the testing fiber [21].

1.3 Light coupling for As_2S_3-on-$LiNbO_3$ platform

In order to characterize the optical properties of the fabricated optical devices, the signal light should be coupled into the device first. D. Marcuse has given the coupling loss between two Gaussian modes, with Eq. (1) [22]:

$$L(dB) = 20 \times \log_{10}\left(\frac{2\omega_1\omega_2}{\omega_1^2 + \omega_2^2}\right) + 4.34 \times \left(-\frac{2d^2}{\omega_1^2 + \omega_2^2}\right) \quad (1)$$

where ω_1 and ω_2 are radii of two modes, and d denotes lateral shift between them.

The first term of Eq. (1) results from the mode mismatch. It vanishes with $\omega_1=\omega_2$. The second term shows that the coupling loss (in the unit of dB) of two Gaussian modes is proportional to d^2. When $d=\omega_1=\omega_2$, the resulted coupling loss (neglecting longitudinal separation and orientation offset) is -4.34 dB.

A typical setup to measure the device under test (DUT) consists of a standard SMF as signal input, DUT sitting on top of translational stage, and another SMF as signal output. This setup works well on testing the insertion loss of Ti-diffused waveguide, because Ti-diffused waveguide matches standard SMF in terms of fundamental mode.

However, a typical mode size of single-mode As_2S_3 waveguide on $LiNbO_3$ substrate is 3 μm × 0.3 μm. This mode size is less than 1/10 of the standard single mode fiber at the vertical direction. This mode mismatch gives rise to huge coupling loss.

Tapered fiber or lensed fiber can be used to convert the SMF mode into smaller mode that matches As_2S_3 waveguide mode better. However, alignment offset tolerance is small according to Eq. (1), making the method vulnerable at unstable environment. Additionally such aligning process is complicated and unrepeatable.

One way that has been proven working is to couple the light through Ti-diffused channel waveguide. Ti-diffused channel waveguide has a similar mode profile as in standard SMF, minimizing the coupling loss between them. Light is first coupled from SMF to Ti-diffused waveguide through butt coupling, then vertically coupled into As_2S_3 waveguide through two-stage taper. One drawback emerges due to the interface roughness between Ti-diffused region and As_2S_3 waveguide region, resulting in 5 dB/cm propagation loss in As_2S_3 waveguide. A similar manner is to use proton-exchanged waveguide to replace Ti-diffused channel waveguide. But this method has increased complexity of fabrication. A common disadvantage for both methods is they both require additional lithography steps involving alignment between different layers, resulting in low repeatability, low throughput and high cost of device fabrication.

1.4 Review of the development of grating coupler

Grating coupler was first proposed by the scientists from IBM in 1970 [23]. The test was on glass films, and the coupling efficiency was claimed to be $40 \pm 5\%$ from monitoring the intensity of all the beams leaving the grating. This method of coupling was simple and repeatable, and was widely applied in the thin-film devices.

D. Taillaert etc. from Ghent University has been leading on the grating coupler related works on SOI platform. In [24], the grating coupler on the semiconductor

platform (GaAs substrate, AlO_x waveguide material) has been demonstrated for the first time, with measured coupling efficiency 19%. Reflectors on both side and bottom of grating couplers have also been proposed, with coupling efficiency increased from 38% to 74%. In [25], apodized grating structure has been proposed and coupling efficiency has been claimed to be 1 dB, with 35 nm bandwidth for TE polarization light. Coupling loss is 3 dB per coupler without the reflector.

In order to further increase compactness of grating coupler with taper, curved grating coupler has been proposed [26]. The new structure has achieved eight-fold length reduction, compared to linear grating, without performance penalty.

1.5 Motivations

As_2S_3-on-$LiNbO_3$ is a promising hybrid platform, with demonstrated work that can be applied to signal processing [15, 27, 28], mid-IR source generation [13, 29] and sensing [30]. With the existing coupling methods, the fabrication cost is high with additional issues such as surface roughness and strict lithography alignment requirement.

In order to address these issues, the grating coupler is proposed on the As_2S_3-on-$LiNbO_3$ hybrid platform in this dissertation. The novel light coupling method enables a single patterning fabrication procedure, with minimum induced surface roughness that would help to improve the performance of multiple structures. The grating coupler can then be used to measure the cavity device, opening the door for the EO tunable filter development.

The design methodology of the grating coupler on As_2S_3-on-$LiNbO_3$ platform can also be applied to thin film $LiNbO_3$. Thanks to the recent development of thin film

$LiNbO_3$ technology, better EO performance can be achieved with $LiNbO_3$ [31]. Using the coupling method developed herein with As_2S_3 grating coupler, devices with superior EO properties can be developed in the future.

1.6 Thesis organization

In Chapter II, topics including optics mode theory, effective index method, coupled-mode theory, transfer matrix method, and the simulation methodology will be discussed. These theories and methods lay the foundation for the design of As_2S_3 grating coupler and other waveguide structures. The focus of this chapter is the design methodology of As_2S_3 grating coupler design, step-by-step.

In Chapter III, thin film preparation and patterning techniques will be covered, with the focus on electron beam lithography for sub-micron patterning. Trouble-shooting details are also documented in this section.

Chapter IV is the result discussions, consisting of four parts. Part 1 focuses on the design, fabrication and characterization of an As_2S_3 grating coupler, with appropriate amount of technique details. The grating coupler is used for measuring sidewall Bragg gratings and grating cavities. Part 2 compares different design structures for the grating coupler on thin film $LiNbO_3$ wafer. The fabrication procedures are discussed. The measurement results are demonstrated for one design, with initial cavity result discussions. Part 3 is about the design, packaging and testing of the $LiNbO_3$ based electric field probe. Part 4 discusses the details of the low-coherence interferometry setup, its capabilities, and the measurement results.

Chapter V consists of the conclusion and future works.

CHAPTER II

THEORETICAL REVIEW*

2.1 Optics basics

In order to fully understand the behavior of light in waveguide, the following parameters need to be specified: waveguide material, waveguide geometry, waveguide mode, and optical loss.

The refractive index of a material is defined by the ratio of the speed of light in vacuum to its speed in the material [32], and it is the most important parameter for the material. Dispersion is the phenomenon that light travels at different speed at different wavelengths in the same material. In other words, the refractive index of this material is wavelength-dependent. Reference [20] is a very convenient online resource for material refractive index based on Sellmeier equation [33]. Fig. 1 plots the refractive index of As_2S_3 at 1525 – 1575 nm, as an example.

---

* Part of this chapter is reprinted with permission from "Characterization of sidewall Bragg gratings using optical low-coherence interferometry with a broadband source," Chen Zhang, Xin Wang, and Christi K. Madsen, *Proc. SPIE* 9365, Integrated Optics: Devices, Materials, and Technologies XIX, 93651G 2015, copyright 2015 by SPIE; doi:10.1117/12.2080104; http://dx.doi.org/10.1117/12.2080104

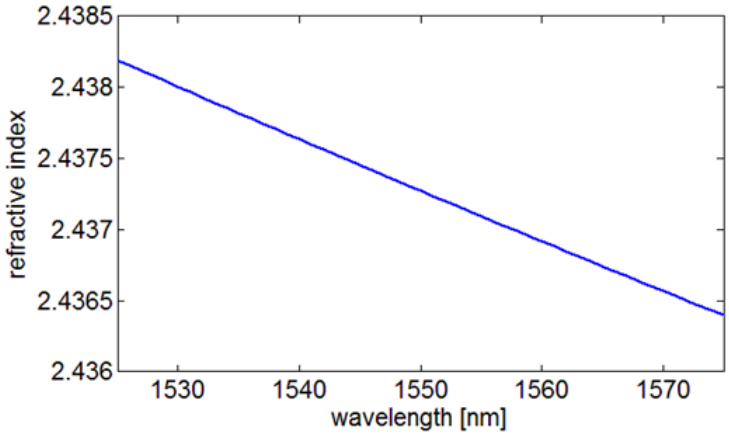

Fig. 1. As_2S_3 material dispersion.

There are several waveguide types in terms of waveguide geometry. They are slab waveguide, rib waveguide, ridge waveguide and cylinder waveguide. Fig. 2 below shows the cross section of each type.

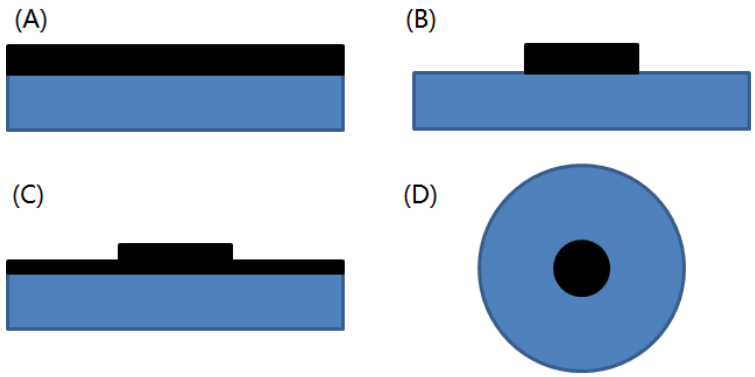

Fig. 2. The cross sections of (A) slab waveguide, (B) rib waveguide, (C) ridge waveguide, and (D) cylinder waveguide.

A slab waveguide is normally a layer of higher index thin film on top of a lower refractive index. Since the structure only forms one dimensional optical confinement, the slab mode is diffracted horizontally. One example of slab waveguide is Er-doped As_2S_3 thin film.

Rib waveguide is the most popular type of waveguide used in our group. The waveguide strip has higher refractive index than the substrate, so the waveguide mode has confinement both horizontally and vertically. Most of our waveguide structure is of this type, including As_2S_3 waveguide on $LiNbO_3$ substrate.

Ridge waveguide is also the type of waveguide structure that confines the optical mode on both dimensions. By varying the thickness of the shallow slab, additional freedom could be introduced into waveguide design. However, ridge waveguides requires additional attention during fabrication process, making it less practical and less cost-effective.

A typical example of the cylinder waveguide is the fiber. It is worth to note that the standard single-mode fiber has 8.2 μm diameter core and 125 μm diameter cladding. The mode-field diameter (MFD) at 1550 nm is 10.4 μm [34].

The light intensity in a waveguide has a unique power distribution at the cross-section of the waveguide. Each distribution is defined as one optical mode. When the waveguide width and height increases, the number of mode supported in the waveguide increases. In waveguide design, it is critical to have the waveguide supporting only one mode (also named “fundamental mode”). Two key parameters are of great importance for optical mode: effective refractive index and mode confinement.

For a certain optical mode, the effective refractive index, or $n_{eff}(\lambda)$, is calculated as the weighted arithmetic mean of the material indices for a specific mode in a certain waveguide structure, as in Eq. (2). Here, A is the area that the optical mode and A_i is the area that this mode overlaps with the material with refractive index of n_i. n_{eff} is the most critical optics parameter in the photonics design, because it directly determines the phase of the light. The simulation value of the effective refractive index of the As_2S_3 rib waveguide directly affect the grating period in grating coupler design, which will be covered in chapter 4.

$$n_{eff}(\lambda) = \frac{\sum A_i n_i(\lambda)}{A} \tag{2}$$

Mode confinement is how much of the light is overlapped with the core at the waveguide cross section. The importance of the mode confinement emerges when we want to take advantage of the property of the $LiNbO_3$ substrate of the As_2S_3-on-$LiNbO_3$ platform. In this case, a taper structure can be used to increase the mode overlapping with $LiNbO_3$ substrate to make the EO tuning of the light more effective.

Optical loss is a key parameter in photonics design. There are several contributing factors for optical loss: fiber-waveguide coupling loss, mode conversion loss, waveguide propagation loss and scattering loss.

Fiber-waveguide coupling loss is caused by the Fresnel reflection, as well as mode mismatch between the fiber mode and the waveguide mode. The Fresnel reflection can be reduced by applying index-matching gel between the fiber tip and the waveguide end facet. Mode-mismatch can be minimized when the input waveguide structure has the

mode shape that resembles the fiber mode the most. As a result, most of our devices were designed with a bus waveguide serving as both input and output ports. The bus waveguide interacts with the photonic structure through on-chip mode converters.

The mode-converter would contribute to the overall optical loss. There are several types of mode converters used in our group, most of which include a taper structure. Previous work on taper structure has been done in our group and low-loss taper structures have been achieved [35].

Waveguide loss consists of propagation loss and out-of-plane scattering loss. The waveguide loss is usually caused by fabrication imperfection, specifically reactive ion etching (RIE) step. Research has been conducted to minimize sidewall roughness [36].

Among all the loss factors, fiber-waveguide coupling loss and mode-conversion loss determines how much power of light could be coupled into the devices such as ring resonator and grating cavity. The waveguide loss is critical because it would affect the resonance of the cavity. Very low-loss waveguide is required in order to achieve high-efficiency non-linear tuning.

2.2 Building blocks for integrated photonic design

This section starts with the individual photonic structure design, including grating coupler, Bragg grating and waveguide taper. Then the individual structures can be combined to realize certain functionalities.

2.2.1 Grating coupler

Fig. 3 illustrates the generic grating coupler structure with both the top view and the side view. w_{GC} is the grating coupler width. Λ stands for the grating coupler period.

The grating coupler duty cycle (DC) is defined in Eq. (3), where d is the length of the grating section within each period. t is the thickness of the grating coupler material.

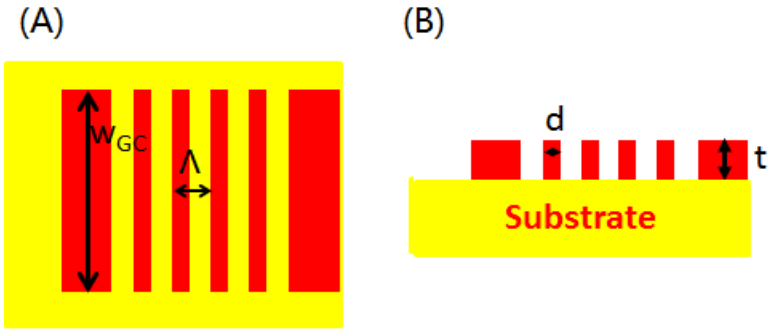

Fig. 3. Generic grating coupler structure: (A) the top view; (B) the side view. The yellow color labels the substrate and the red color labels the grating material.

$$DC = \frac{d}{\Lambda} \tag{3}$$

Fig. 4 shows how the grating coupler works for light coupling. Light is guided through the waveguide. A periodic refractive index perturbation is introduced to the grating area of the waveguide layer.

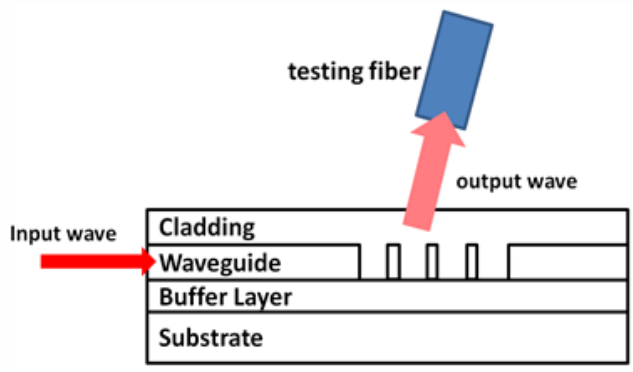

Fig. 4. The Side view illustration of how grating coupler works as an output port.

Light diffraction at the grating coupler is governed by Eq. (4) [23]:

$$\Lambda = \frac{\lambda}{n_{eff} - n_c \sin\theta} \tag{4}$$

where λ is the central wavelength (usually called the Bragg wavelength), n_{eff} is the effective refractive index of the grating coupler, n_c is the refractive index of the cladding fiber mode, and θ is the coupling angle from the normal.

As the starting point of the grating coupler design, effective index method (EIM) is used to calculate the effective index of the grating coupler. EIM simplifies the waveguide cross section into a single material with the refractive index of $_{neff}$. EIM can be implemented by either Matlab (APPENDIX A) or Fimmwave. Given the required coupling angle (typically 17°), one can have an initial set of grating coupler geometries of period and DC as the initial values for the modal simulation and optimization. For example, Fig. 5 plots the grating coupler period dependence on the duty cycle, with different material thicknesses. Here, the grating coupler material is As_2S_3, and the substrate is $LiNbO_3$. In this example, the grating coupler period of 1.1 μm, DC of 0.5

and As_2S_3 thickness of 500 nm would be selected as the initial values of modal simulation, in order to leave enough room for the grating fill factor optimization and to maximize the minimum feature size for ease of fabrication

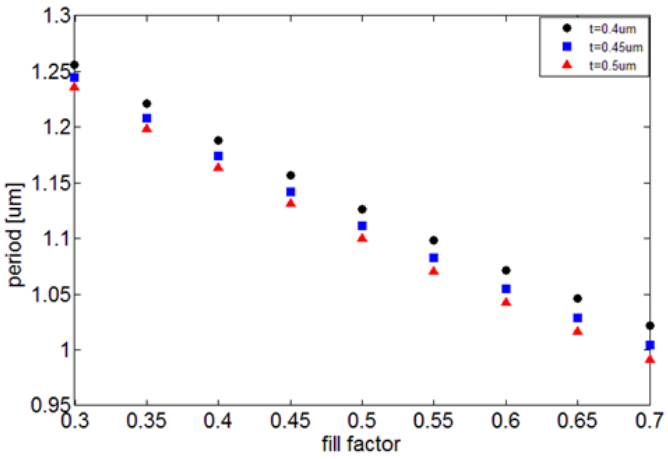

Fig. 5. The grating period vs. grating fill factor, at different values of waveguide thickness

Fimmprop from Photon Design Inc. is used to simulate the optical field. With plain wave as an input, the software is able to simulate the output optical field. By using Matlab or Python, we are able to calculate the overlapping integral between the grating coupler output and a standard SMF, as well as the normalized power output with respect to the input light. The optimization criterion is to maximize the product of these two terms. The optimization script is attached in APPENDIX B.

For the single-layer uniform grating coupler, the coupling efficiency is limited by the following factors: substrate leakage, back reflection and mode-mismatch. Several

design techniques can be applied to increase the grating coupler efficiency by addressing one of the above issues.

Substrate leakage means that a portion of the input light will be directed to the substrate direction and lost. The specific technique to minimize this loss is to introduce a reflector between the substrate and the grating coupler. On silicon on insulator (SOI) platform, this technique has been widely employed. Specifically, SiO_2 and Si thin film pairs has been used as "Bragg reflector" to replace the metal reflector and the coupling efficiency is increased from 60% to more than 90% [25]. In the design of Bragg reflector, the higher the refractive index contrast is, the higher the reflection would be, at the cost of narrower grating coupler bandwidth. The more layers in the Bragg reflector would also result in higher reflection, with the same drawback of bandwidth. From the fabrication point of view, more layer means higher fabrication cost; and introducing a different material in the Bragg reflector section with the sole purpose of increasing the grating coupler efficiency would also mean higher fabrication cost. So a good Bragg reflector design should take into account all the factors.

Back reflection is the inherent issue of the grating structure, which can be partially addressed by having the grating layer partially etched, as shown in Fig. 6. The reported efficiency boost by applying this technique is 78% [37]. However, the controlled etching technique is very difficult to realize.

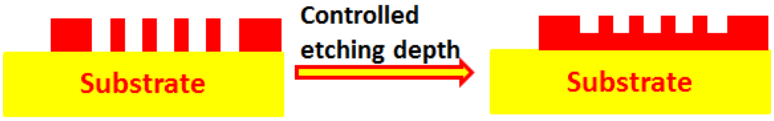

Fig. 6. Partially etched grating coupler can reduce back reflection.

Mode-mismatch quantifies the difference between the grating coupler output and the Gaussian approximation in SMF. Mode-mismatch can be minimized by tweaking the first several periods of the grating coupler (the period is counted from the left-hand side of Fig. 4) to make the mode more resembles Gaussian shape. In [25], the overlapping integral between these two modes is almost 100%.

2.2.2 Sidewall Bragg grating

Sidewall Bragg grating is also formed by periodical corrugation of the waveguide structure. The grating parameters used for fabrication are defined in Fig. 7. Here, w_0 is the width for the single-mode waveguide. $w_1$and w_2 are widths for longer and shorter grating teeth, respectively. Λ_B represents Bragg grating period. $\Delta w=(w_1-w_2)/2$ define the grating depth, which is directly related to the grating coupling strength.

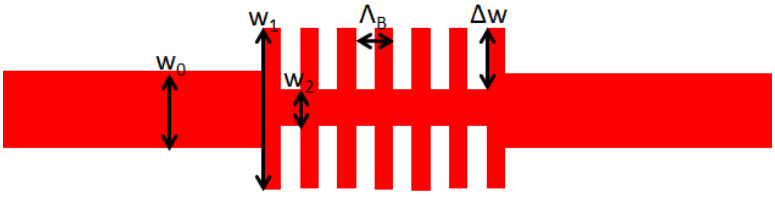

Fig. 7. Sidewall Bragg grating parameters.

The differences between a sidewall Bragg grating and a grating coupler are:

(1) Geometry. A grating coupler is formed through surface corrugation, while a sidewall Bragg grating is formed through sidewall corrugation.

(2) Functionality. A grating coupler is used to couple the light between the waveguide-based structure and the test fibers, while a sidewall Bragg grating is used for wavelength filtering.

Coupled-mode theory (CMT) explains how the two spatially overlapping optical modes are interacted. And it guides the design of sidewall Bragg grating. The mode coupling between two counter-propagation waves is governed by Eq. (5) [38] :

$$\begin{aligned} \frac{d}{dz}A_1 &= -j\kappa A_2 e^{j\Delta\beta z} \\ \frac{d}{dz}A_2 &= j\kappa^* A_1 e^{-j\Delta\beta z} \end{aligned} \tag{5}$$

Here, κ is coupling coefficient, indicating how strong the two waves are coupled; A_1 and A_2 are the wave amplitudes; $\Delta\beta = \beta_1 - \beta_2$ is the phase mismatch between two waves. Solving for the coupling equation, the coupling efficiency can be expressed by κ and Δβ using Eq. (6). It is straightforward that the coupling efficiency is maximized when phase mismatch is zero.

$$\eta = \frac{|\kappa|^2 \sinh^2 sL}{s^2 \cosh^2 sL + \left(\frac{\Delta\beta}{2}\right)^2 \sinh^2 sL} \tag{6}$$

Coupling coefficient κ is the most important parameter in sidewall Bragg grating design. Generally, the coupling coefficient increases with the grating depth Δw, as well as the number of grating periods N.

Transfer matrix method (TMM) is the method that breaks down any grating structure into cascaded segments, with each segment expressed by a 2 by 2 matrix. The matrices of the waveguide and the refractive index step are as follows [39]:

$$T_w = \begin{bmatrix} e^{j\beta L} & 0 \\ 0 & e^{-j\beta L} \end{bmatrix}$$
$$T_s = \begin{bmatrix} \frac{n_1 + n_2}{2\sqrt{n_1 n_2}} & \frac{n_1 - n_2}{2\sqrt{n_1 n_2}} \\ \frac{n_1 - n_2}{2\sqrt{n_1 n_2}} & \frac{n_1 + n_2}{2\sqrt{n_1 n_2}} \end{bmatrix} \quad (7)$$

Here, β is the propagation constant of the input light, L is the length of the segment, n_1 is the input refractive index, and n_2 is the output refractive index. With these two basic matrices, one could derive any grating matrix T by cascade all the matrices using Matlab.

$$T = T_1 T_2 \bullet\bullet T_n \quad (8)$$

The resulting matrix is also a 2 by 2 matrix. The overall relationship between input and output waves can be written as in Eq. (9). Here, E_{in_f} and E_{in_b} denote the forward and backward waves from the input side, while E_{out_f} and E_{out_b} denote the forward and backward waves from the output side.

$$\begin{bmatrix} E_{in\_f} \\ E_{in\_b} \end{bmatrix} = T \begin{bmatrix} E_{out\_f} \\ E_{out\_b} \end{bmatrix} \quad (9)$$

As a result, the reflection (R) and transmission (T) responses of the grating structure can be calculated by Eq. (10).

$$R = \left(\frac{E_{in\_b}}{E_{in\_f}} \right)^2$$
$$T = \left(\frac{E_{out\_f}}{E_{in\_f}} \right)^2 \quad (10)$$

2.2.3 Taper

The grating coupler has the typical width of 12 μm, while the sidewall Bragg grating has the maximum width of 2 μm. The bridge that builds connection between these two building blocks is adiabatic taper.

Adiabatic taper is optically lossless taper. The taper is adiabatic when the tapering region is longer than a threshold value [40]. From the design perspective, it is beneficial to make the taper long enough to eliminate the taper loss. However, this would make the whole device bulky. One way to shrink the size of the taper is to replace the regular grating coupler with curved grating coupler [26].

2.2.4 FP cavity construction and analysis using TMM

The most important application of sidewall Bragg grating is to use two gratings to construct a Fabry-Perot (FP) cavity. A generic structure that consists of grating coupler, sidewall Bragg grating, taper and straight waveguide is shown in Fig. 8.

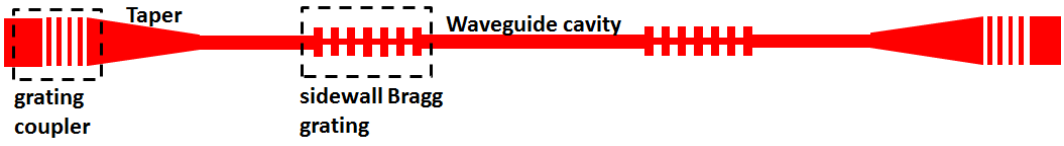

Fig. 8. A grating cavity device.

This grating cavity can also be analyzed through TMM. For instance, we choose As_2S_3 waveguide with the width variation from 0.9 μm to 1.1 μm. The thickness is 400 nm. In order to get the segment matrices, EIM is employed to solve for the effective refractive indices at these waveguide widths, as shown in Fig. 9.

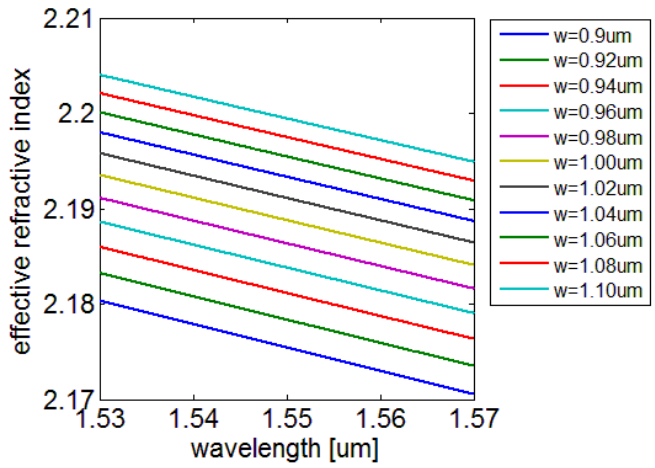

Fig. 9. Effective refractive indices for different waveguide widths.

Fig. 10 plots different transmission spectra of the sidewall Bragg gratings with different grating depths range from 40 nm to 200 nm. It can be seen that the resonance wavelength is shifted towards the shorter wavelength direction as the grating depth increases, because gratings effective refractive index decrease as grating depth increases with fixed average grating width.

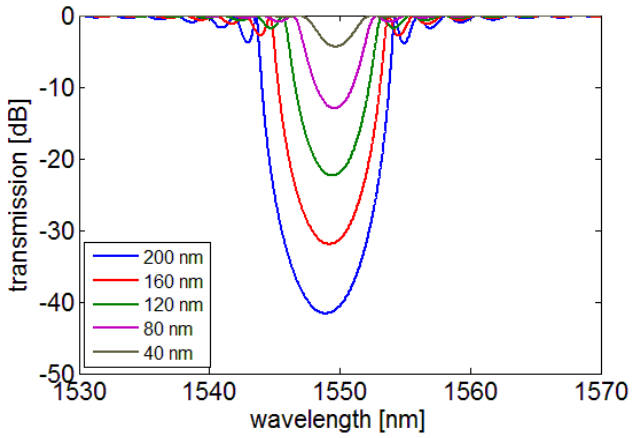

Fig. 10. Transmission spectra of sidewall Bragg gratings with different grating depths.

If such Bragg gratings are on both ends of a straight waveguide, a FP cavity is constructed. Since our platform is based on $LiNbO_3$, the cavity response can be EO-tuned due to the excellent EO property of $LiNbO_3$. Fig. 11 shows the tuned grating cavity response. The grating cavity length is 1 mm. The grating depth is 80 nm with 500 period on both ends of the cavity. The refractive index change of 0.0002 is assumed for the optical mode in the cavity. It can be concluded that 0.52π phase shift is achieved in this case.

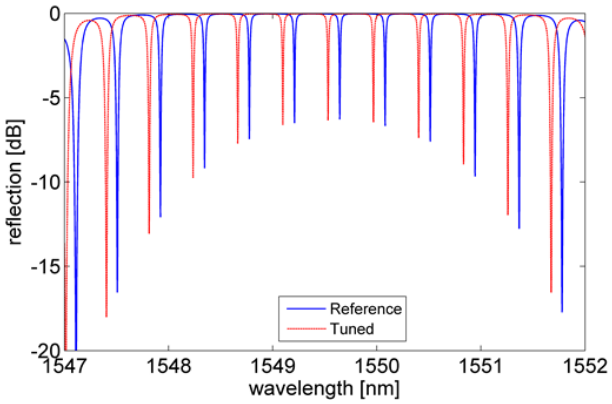

Fig. 11. The grating cavity response (blue) and the EO-tuned response (red).

2.3 Optical low-coherence interferometry

Optical low-coherence interferometry (OLCI) uses a continuous-wave broadband source and a variable-delay interferometer to obtain a spatially-localized fringe pattern, as illustrated in Fig. 12. A low coherence source is split into two paths by a coupler. One path contains a DUT, and the other path contains a variable optical path. When the variable optical path is varied linearly, a fringe pattern can be detected at the output end. When the interference fringe pattern is Fourier transformed, the spectral density of the source is obtained [41].

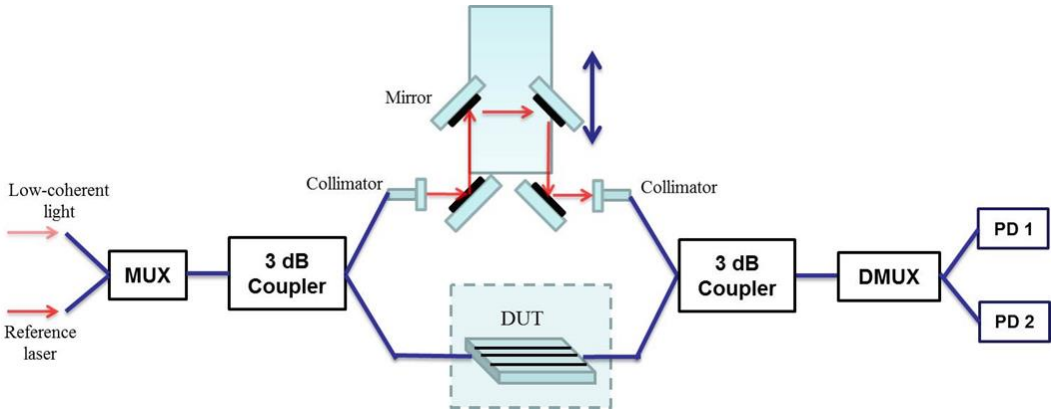

Fig. 12. Configuration of an optical low-coherence interferometry. MUX: multiplexer; DMUX: demultimpexer; PD: photodetector; DUT: device under test.

Assuming that the source in Fig. 12 has a spectral density S(f), DUT has a amplitude response A(f) and phase response φ(f), and the variable-delay path has a phase change term of θ. The output signal in frequency domain would be given by Eq. (11):

$$I(f) = \frac{S(f)}{4}\left[1 + |A(f)|^2 + 2A(f)e^{-j(\varphi(f)+\theta)}\right] \tag{11}$$

Since the variable-delay optical path is often realized by translating opposing mirrors in the air, θ can be expressed by Eq. (12):

$$\theta = 2\pi f \frac{v\tau}{c} \tag{12}$$

where v is the mirror translation speed, and τ is the stage translation time.

Integrate I(f) over frequency of the source is expressed by Eq. (13):

$$I = \int\left[\frac{S(f)}{4} + \frac{S(f)}{4}|A(f)|^2 + \frac{S(f)}{2}A(f)e^{-j(\varphi(f)+\theta)}\right]df \tag{13}$$

where the first two terms are not time-related. Rewrite this integral, keeping only the time-dependent terms:

$$I(\tau)=\int \frac{S(f)}{2}A(f)e^{-j\varphi(f)}e^{-j2\pi f\frac{v\tau}{c}}df \tag{14}$$

Plug in g(f) and t with the following expression:

$$\begin{aligned} g(f)&=\frac{S(f)}{2}A(f)e^{-j\varphi(f)} \\ t&=\frac{v\tau}{c} \end{aligned} \tag{15}$$

The integral could be expressed by:

$$I(t)=\int g(f)e^{-j2\pi ft}df \tag{16}$$

This equation has a basic Fourier transform form. If I(τ) is inverse Fourier transformed in Eq. (17). The DUT's magnitude and phase response, as well as the spectral density of the source, can be solved.

$$\mathcal{F}^{-1}\left[I(t)\right]=\int I(t)e^{j2\pi ft}dt=\frac{S(f)}{2}A(f)e^{-j\varphi(f)} \tag{17}$$

A simplified scenario can be quickly checked, with no DUT inserted to the arm, which means:

$$\begin{aligned} A(f)&=1 \\ \phi(f)&=0 \end{aligned} \tag{18}$$

In this case, the spectral response could be extracted directly by inverse Fourier transform the output fringe pattern, as discussed above.

CHAPTER III

FABRICATION PROCESS

3.1 Thin film preparation

Thin film preparation is the first step for device fabrication. There are multiple ways to prepare thin films: sputtering, electron beam evaporation and plasma-enhanced chemical vapor deposition (PECVD). Table 1 compares different methods regarding their applications.

Table 1. Different thin film preparation methods.

Thin film method	Target materials	Applications
Sputtering	SiO_2, Al_2O_3, As_2S_3; Ti, Al, W, Er	High deposition rate and high quality dielectric and metal deposition.
Electron beam evaporation	Ti, Cr, Al,	Metal deposition with high requirement on directionality.
PECVD	SiO_2, Si_3N_4	Stoichiometric SiO_2 and Si_3N_4 with high film quality.
Spin-coating	SU8, PMMA	Polymer films for lithography.

Sputtering is the most common thin film preparation method in our group. The available targets include 3 dielectric materials (SiO_2, Al_2O_3, As_2S_3) and 4 metal materials (Ti, Al, W, Er).

When small features require metal liftoff, electron beam evaporation is needed, to avoid sidewall deposition. Chromium (Cr) is a common material for this purpose, while titanium (Ti) is also an option. During the electron beam evaporation process, high energy (~10KeV) electron beam is directed to the metal pellets in a ceramic crucible. The metal material is completely melted and the molecules in the vapor travel in a vertical straight line to hit the samples, resulting in anisotropic deposition.

PECVD is a chemical method to deposit dielectrics. For good quality films (SiO_2 and Si_3N_4), the deposition is usually carried out at a higher temperature (~350 °C). Since As_2S_3 has a low transition temperature, the sample is not suitable for PECVD if it already has As_2S_3 material on it. Despite this limitation, PECVD is still very useful, especially for nitride compound (AlN or Si_3N_4).

Spin-coating can be used to coat liquid form materials, most of which are polymers. A following step is usually performed to solidify the coated layer. It is either thermal treatment or UV curing, depending on the type of polymer.

3.2 Lithography

Patterning is the key step to define the geometries of the devices. Different patterning techniques are available for different applications. The main lies in the minimum feature size achievable by each method. Table 2 compares different patterning technologies and their specifications. Due to the feature size requirement and availability

of the machine, electron beam lithography (EBL) is used for grating and grating coupler patterning.

Table 2. Different patterning technologies and their capabilities.

Technology	Minimum feature size	Yield	Mask requirement
Photolithography (contact)	2 μm	Medium	Yes
Photolithography (projection)	50 nm	High	Yes
EBL	Sub-10 nm	Low	No

JOEL JBX 5500FS electron beam writer in University of Houston Nanofabrication Facility is used for patterning, in order to deliver the feature size as small as sub-200nm.

3.2.1 Mask drawing

The flexibility of mask layout is one big advantage of EBL over photolithography. Klayout is used to prepare GDSII mask files for EBL. The concept of hierarchical design is employed in the mask design process. The mask layout consists of three levels: component level, device level, and chip level. On component level, the basic building blocks such as gratings, tapers, and waveguides are layout into individual

cells. On device level, each device cell consists of one combination of the component level cells. On the chip level, each chip cell consists of multiple device cells. Fig. 13 shows example on each level of a hierarchical design. Multiple chip cells can be included in a single EBL exposure, which will be covered in the later section.

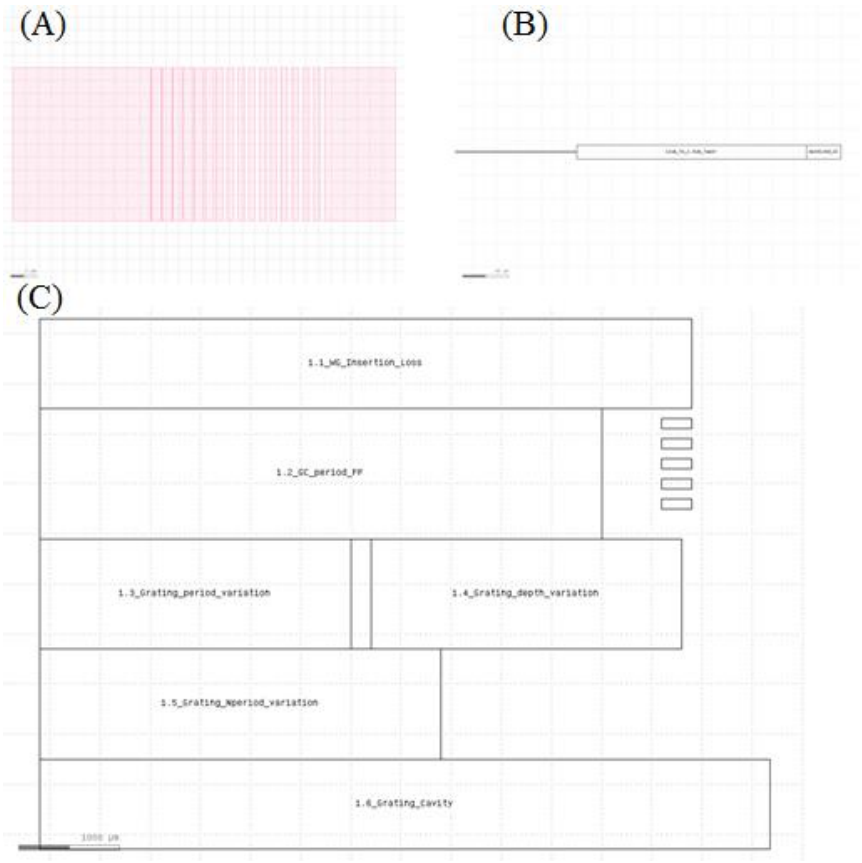

Fig. 13. Hierarchical mask design example. (A) Component level: Apodized grating coupler; (B) Device level: grating coupler device with taper; (C) Chip level.

Data type should be defined during mask drawing. It is a very useful concept when it comes to employing multiple doses in one single chip cell. One example that

requires more than one data type is the correction for electron proximity effect. Electron proximity effect is the broadening of the electron beam, caused by the electron scattering. By assigning different data types to components with different pattern densities, the proximity effect can be partially resolved at the exposure step, which will be covered in the later section.

Due to fabrication imperfection, it is never the case to have the device with exactly the dimensions as designed. This will become a problem when there is a tight restriction on the device performance. One way to compensate for this geometry offset is to tweak the mask patterns. For example, the grating period is directly related to the resonance wavelength in the transmission spectrum. With the fabrication imperfection, the resonance wavelength can be shifted by up to 20 nm. If the period of the grating is increased by 5 nm, the resonance wavelength can be shifted to the design value.

3.2.2 Resist preparation, spin-coating and soft-baking

Polymethyl methacrylate (PMMA) from MicroChem Corp. is used as the positive resist for EBL. There are different molecular weight (MW) and different solvent products available. The spin curve is available in reference [42]. We use the mixture of 950C 9% PMMA and the corresponding thinner, with the volume ratio 1:3.

The PMMA solution is spin-coated onto the sample at 2500 rpm for 1 minute. The ramp is 1250 rpm/s. Then the sample is soft-baked on a hotplate at 180°C for 2 minutes to vaporize the solvent. It is worth noting that the sample should be directly in contact with the hotplate, without Al foil in between, in order to make sure that the resist is baked above the critical transition temperature. One issue follows is that the plastic

tweezers that normally used to handle the $LiNbO_3$ sample would be melted contacting the surface of 180° hotplate. One way to avoid the tweezers melting is to use a pair of metal tweezers to gently sweep the $LiNbO_3$ sample from the center to the edge of the hotplate after 2 minutes and use an Al foil to pick up the sample.

3.2.3 Machine calibration

After properly coated with PMMA, the sample is loaded onto the cassette. The cassette is the sample hold for the EBL system, and it is designed carefully so that the calibration marks and the sample surface have a known height distance. Before the cassette is loaded into the EBL load lock, an "X" is marked at the left corner of the sample surface, for focusing purpose.

The touch screen (Fig. 14) by the load lock shows the pressure details for both the load lock and the main chamber. After the cassette is locked in the load lock, press and hold "EVAC" button. It normally takes 5-10 minutes for vacuum gauge 2 (VG2) to reach 4×10^{-3} Pa before the sample is allowed to be loaded to the main chamber. It is worth noting that it would take longer if the sample or the cassette contains too much moisture. So it is important that the sample is properly soft-baked and the sample loading process is as quick as possible.

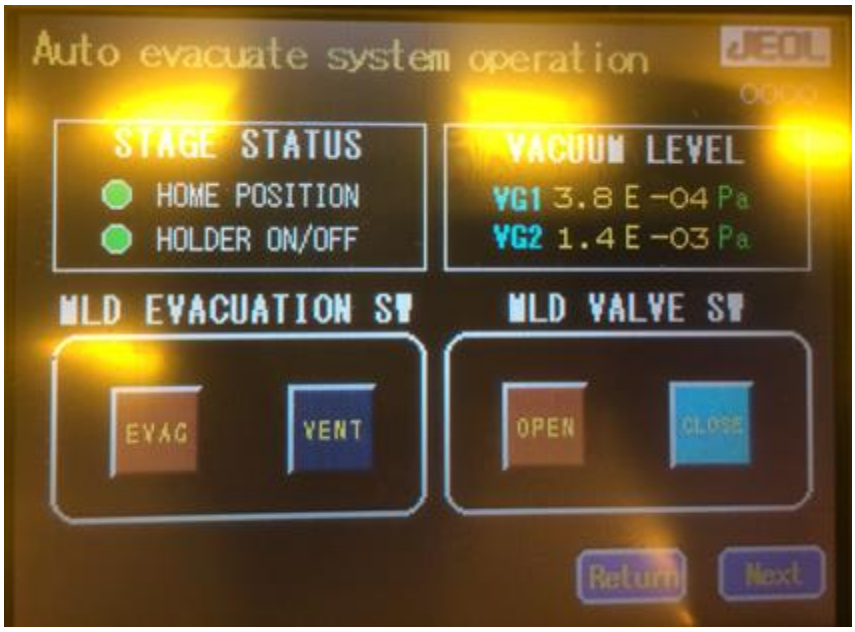

Fig. 14. Touch screen of the E-beam system

Once the sample is loaded into the main chamber, the “HOLDER ON/OFF” indicator turns green, and it takes another 5-10 minutes for vacuum gauge 1 (VG1) to reach 3×10^{-4} Pa. The indicator for the chamber to be ready is when the pressure gauge rod is sticking out (Fig. 15). The “HOME POSITION” indicator in Fig. 14 shows whether the cassette is at home position (green) or not (black). ONLY when the cassette is at the home position is it allowed to unload it from the chamber.

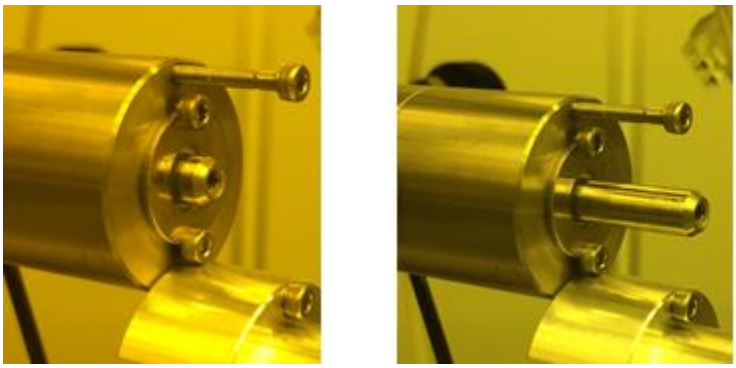

Fig. 15. Chamber pressure gauge rod position when (A) VG1>3×10^{-4} Pa; and (B) VG1<=3×10^{-4} Pa.

Three key parameters need to be specified for the system at the beginning of EBL procedure: mode, aperture, and beam current.

(1) Mode. There are two modes available for this EBL system: mode 2 and mode 4. The key parameters for each mode are listed in Table 3 below:

Table 3. Key parameters for both lithography modes.

	Mode 2	Mode 4
Field size	1 mm × 1 mm	100 μm × 100 μm
Sub-field size	10 μm × 10 μm	1 μm × 1 μm
Scan step	5 nm	0.5 nm
Resolution	Low	High

The main difference between these two modes is that mode 2 has the field size of 1 mm with low resolution, while mode 4 has the field size of 100 μm with high resolution. In order to pattern 200 nm grating features with good resolution, mode 4 must be used.

(2) Aperture. There are four apertures for this system. Aperture 2 (A2) is used. The knob for the apertures is by the E-beam column, as shown in Fig. 16 below.

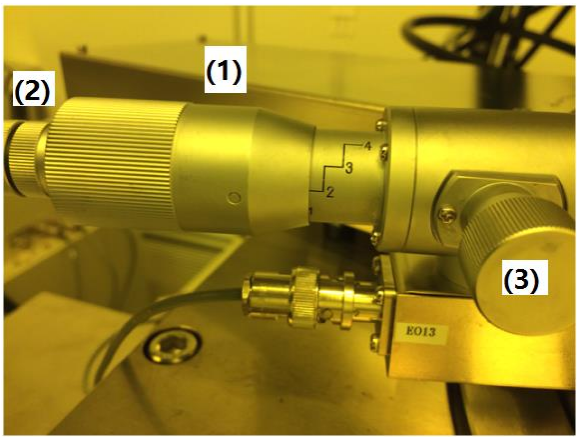

Fig. 16. The picture of (1) the aperture-switching knob, (2)(3) lens translation knobs. The current setting is at aperture 2 (A2).

(3) Beam current. Beam current is directly related to the quality of the EBL pattern and the exposure time. It takes roughly twice the time to write a specific pattern with the same electron dosage using 1 nA, compared to 2 nA beam current setting. On the other hand, 1 nA beam current produces higher quality features than 2 nA beam current does. It requires design of experiments (DOE) to decide what current to use, since the E-beam exposure result is normally pattern-specific. In our case, 1 nA is used.

In order to set the writing mode (mode 4), aperture (A2), and beam current (1 nA) as discussed above, the calibration file “M4-A2-1nA” should be selected before calibration is performed. It is worth noting that it takes up to 2 hours for the beam current to stabilize if the mode is switched. So it is necessary to notify the facility in advance (through online reservation system) that mode 4 would be used.

The very first step of EBL operation is to calibrate the electron beam. Manual calibration should be performed once, in order to bring the machine to a reasonably calibrated state [43]. There are three steps in manual calibration. The first step is to use Faraday cup (FC) to measure the beam current, to make sure that the current reading agrees with the calibration file. If there is a minor disagreement, adjust “LENS 2/3” value to make the current reading exactly 1 nA. This value should not be changed by more than a few hundred, unless something has gone wrong, in which case the lab manager should be notified.

The next step in manual calibration is to correct deflection using BE mark. BE mark is an EBL cross mark to correct deflection, shown in Fig. 17. By moving the stage, the center of the BE mark should be close to the center of the screen, which is defined by the crossing of the two red lines in Fig. 17.

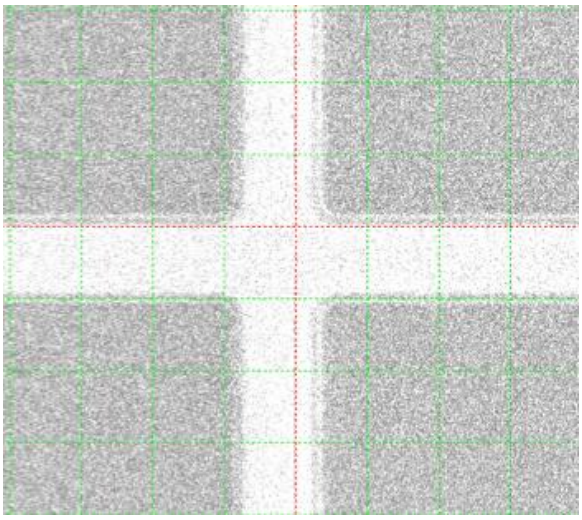

Fig. 17. SE image of BE mark. The bright cross is the BE mark, while the red lines are the center lines of the screen.

After centering the BE mark, it is also necessary to check if the aperture is aligned by checking the WOBB tab. The two knobs to adjust X and Y translations of the aperture can be found in Fig. 16 as well. The aperture is centered when the BE mark is defocusing without shifting during wobbling.

AE mark is another EBL mark for automatic focus. AE mark should be centered after BE mark in the similar manner.

Automatic calibration can be performed following the manual calibration procedure discussed above. It is worth to note that the manual calibration is only required for the first sample. The rest of the samples can start from here. Fig. 18 shows the calibration screen from the system software. For the first exposure, it is necessary to check “Current Measurement”, “Std. Mark Detection”, “Automatic Focusing”, and “Deflection Correction”, as well as both AE and BE marks. For the following samples,

"Automatic Focusing" and AE mark do not need to be checked, since the focus value has already been brought within the tolerance after the first auto-calibration.

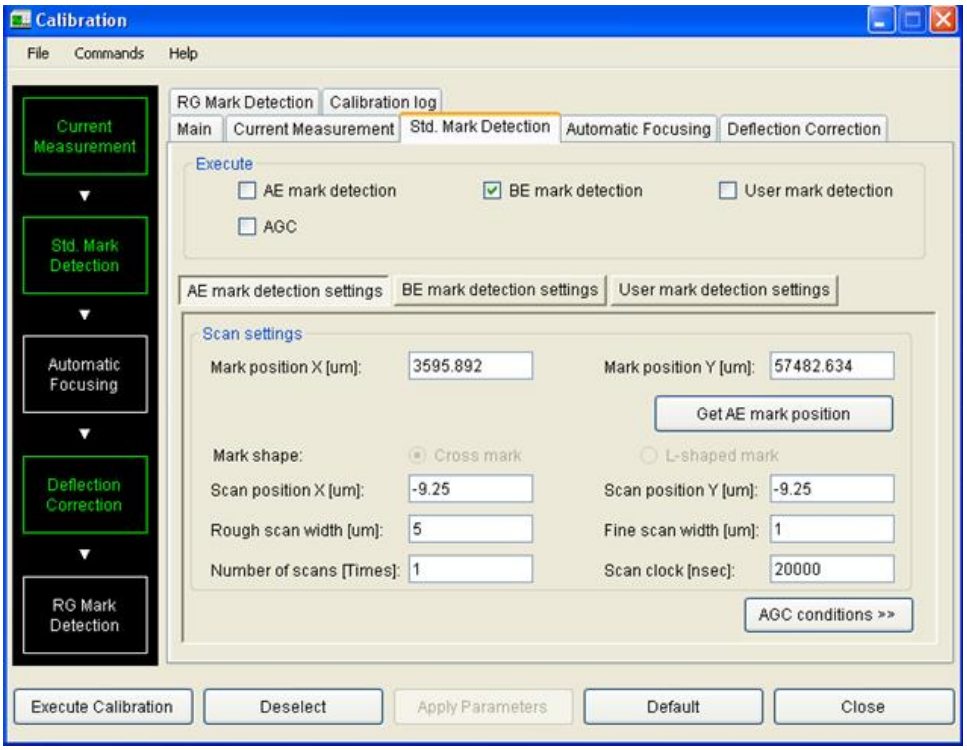

Fig. 18. Auto-calibration pop-up window. If it is the first calibration attempt, "automatic focusing" and "AE mark detection" also need to be checked in order for the system to decide the rough focus point.

Click "Execute Calibration" to proceed with auto-calibration. It takes 2 minutes for the system to calibrate. The electron beam would scan over the small area across the AE and BE marks, at the location specified by the manual calibration step.

3.2.4 Alignment

After calibration, the quality of the beam is optimized. At this point, if the position of the pattern is specified, alignment procedure should be performed. In this case, a pair of tungsten (W) crosses, as well as the center coordinates of the pattern relative to the W cross, is required.

The first step for alignment is to manually find the location of one of the crosses on the sample. Usually we try to find the upper cross, and we define it as mark P. This step is the most time consuming, especially for the first sample. One way to make this step faster is to accurately estimate the location of the mark P relative to the top left corner of the cassette, because the stage coordinates of that corner is known, and it is stored in the system. After this step, the stage coordinates of mark P should be recorded

Once mark P is located, std. mark detection should be performed. The window for this step is shown in Fig. 19. The stage coordinates from the previous step should be typed in mark positions (X and Y) columns under “user mark detection setting” tab. The purpose of this step is for the system to find the accurate coordinates for mark P. After clicking “execute”, the accurate stage coordinates of mark P should be recorded.

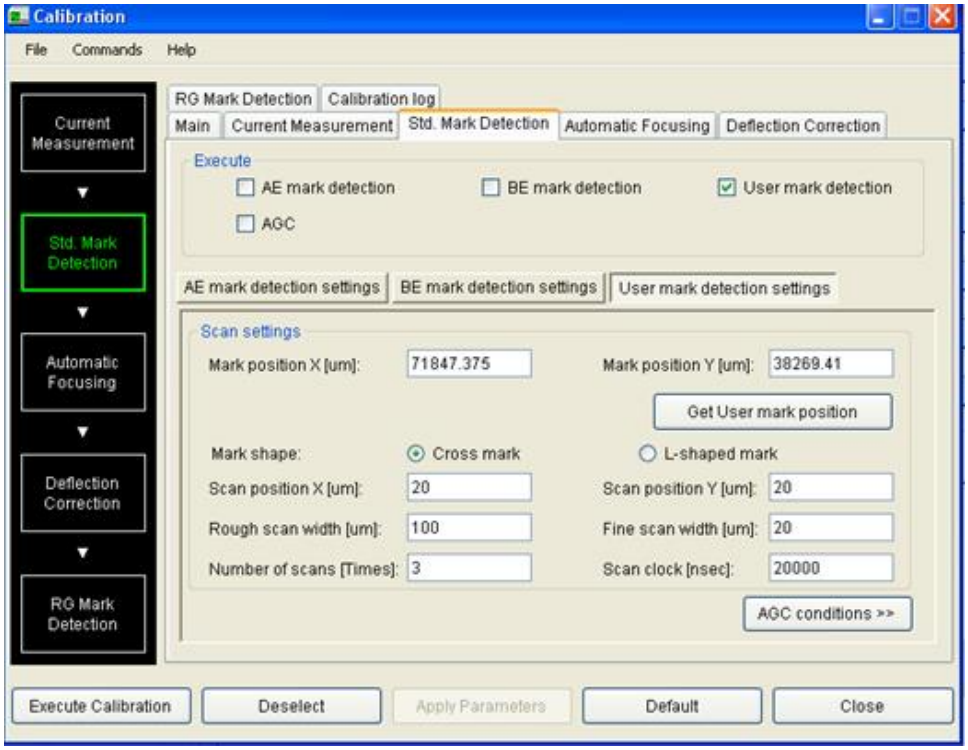

Fig. 19. The pop-up window for std mark detection for alignment. “Std Mark Detection”, “User mark detection” should be checked, and the stage coordinates of mark P should be typed in.

The next step is for the system to find mark Q. The window for this step is shown in Fig. 20. Here it is necessary convert the stage coordinates into exposure coordinates for mark P using “EBW helper” tool available on the PC desktop. Basically these two coordinate systems are differed by a constant displacement with different sign notations. Different columns of the software require one of the two coordinate systems. If P and Q are designed with the same y coordinate, the exposure coordinate for Qx is the same as Px, while Qy is Py minus the y distance between the two marks. If the sample rotation offset is within 1°, the system should be able to find Q and the actual rotation of the

sample will be calculated after “execute” is pressed. This actually angular offset will be taken into account by the system during exposure.

Since the system is not able to rotate the stage to compensate for the angular offset, it has very tight restriction for this value. If the sample is loaded with a rotation angle larger than 1°, the system would not proceed, in which case the sample need to be unloaded and the angle need to be carefully adjusted.

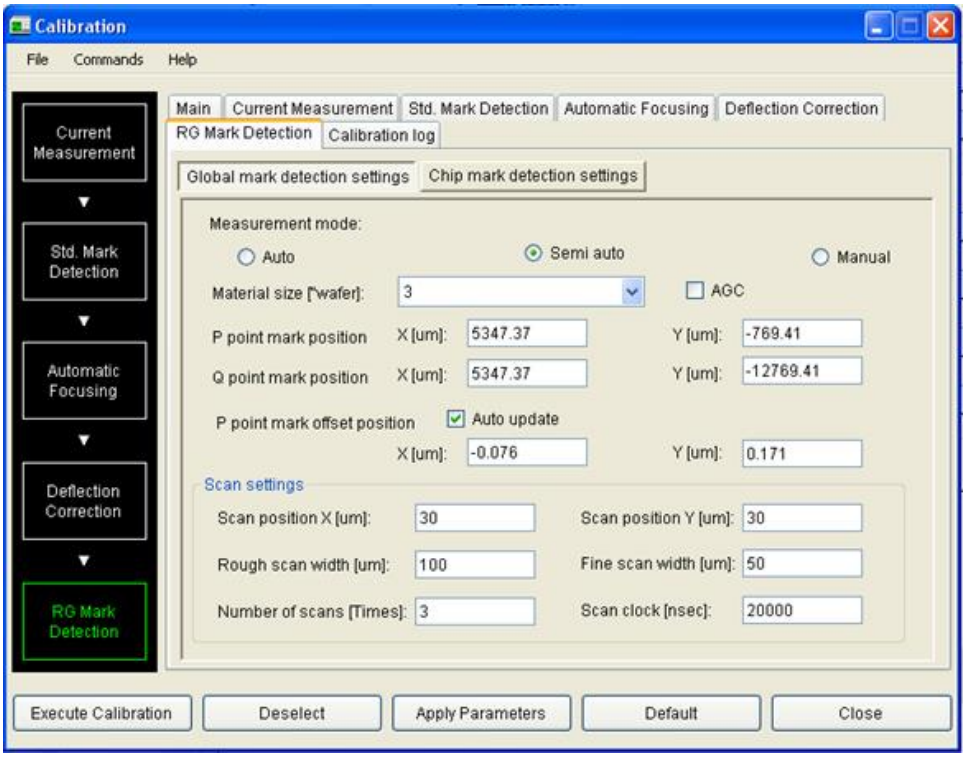

Fig. 20. The pop-up window for RG mark detection for alignment. “RG Mark Detection”, “Auto update” should be checked, and P & Q coordinates should be typed in.

3.2.5 Focus adjustment and deflection correction

After the auto-calibration step, the electron beam is focused on the mark surface, with perfect beam quality. However, the sample surface is at a different height (shown below in Fig. 21). It is thus necessary to adjust the focus again due to this height difference, before exposure.

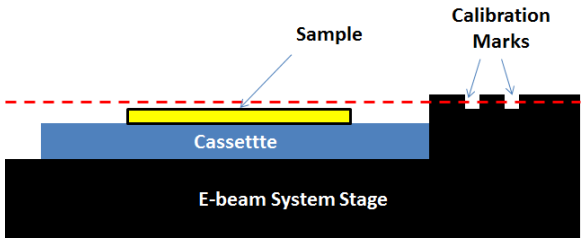

Fig. 21. Height difference between the AE, BE marks and the sample surface. The red dashed line shows the height level of the marks.

According to the user manual from University of Nano-Fabrication Facility, it is suggested that the focus value should be increased by 100 in mode 4. A more accurate method is to directly focus the beam onto the sample surface. For samples that contain W alignment marks, the beam should be focus on the alignment mark. For samples that do not require alignment, the beam should be focused on the "X" mark near the top left corner of the sample.

When conducting focus adjusting, it is usually convenient to change the scan window and the scan clock at different stages. For example, when you are trying to find the alignment mark, you need to maximize the scan window (100,000 for this system);

when you are trying to focus accurately on the mark, you need to obtain the most zoomed-in view, or the smallest scan window (5000 for this system). The scan width and scan clock values at different situations are listed in Table 4:

Table 4. Field size and scan clock change.

Situation	Default value	Wobbling	Finding the mark	Focusing
Scan width	10,000	10,000	100,000	5000
Scan clock	2500	500	2500	5000

Once the focus value is changed by manual focus after auto-calibration, it is necessary to re-run the calibration with “Deflection Correction” and “BE mark” checked, to correct for the field size change caused by focus value change. In other words, the automatic calibration should be performed again with the setting in Fig. 18.

The complete calibration procedure is summarized in APPENDIX C.

3.2.6 Exposure

The sample should be exposed to the electron beam, in the manner specified in the “Exposure” screen, as shown in Fig. 22. The system is capable of handling multiple jobs, with each job containing multiple data types, for a single exposure. The system is designed in the manner that “job 1” is exposed, and then “job 2”, and so on. The introduction of “job” enables you to expose the same pattern with different doses, while

the introduction of “data type” enables you to expose with modulated dose at different area of a single pattern.

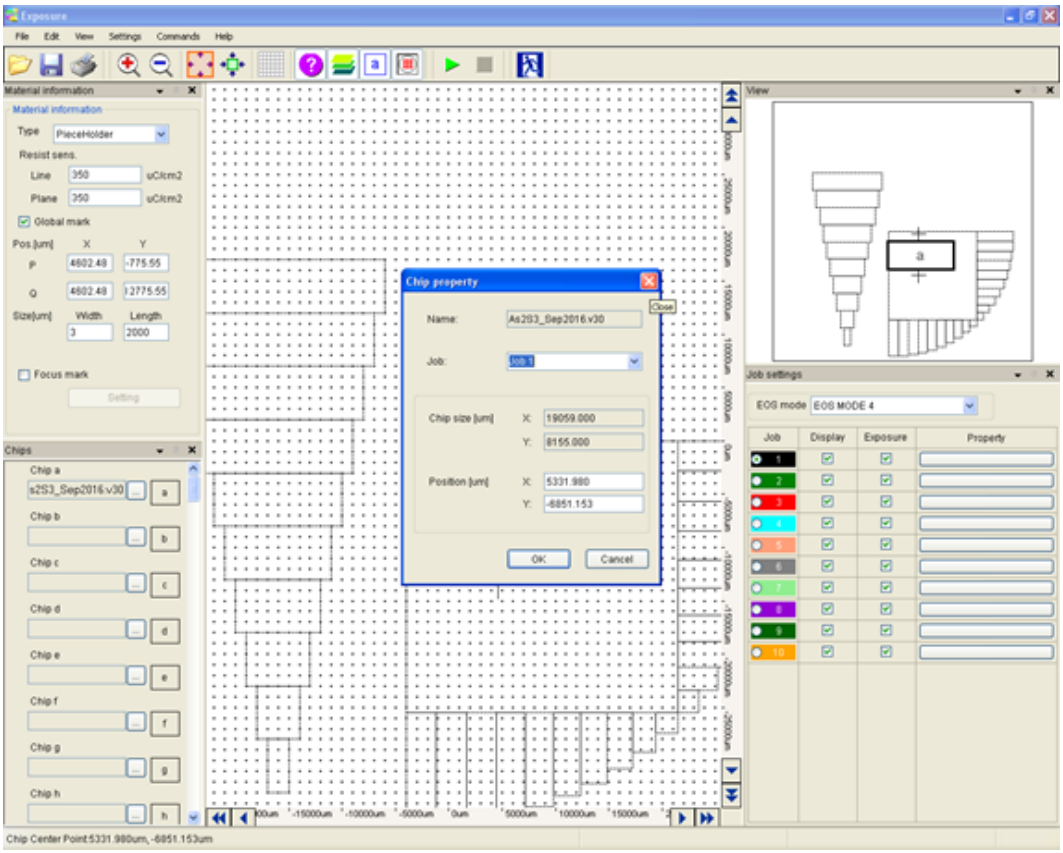

Fig. 22. Exposure window.

In “material information” section, it is necessary to specify type of the cassette and the base dose. If the alignment is required for the exposure, “Global mark” should be checked and the exposure coordinates of P and Q should be typed in. The width and length of the alignment marks also need to be specified, which only affect the alignment marks drawn on the screen.

In “Chips” section, multiple chips can be included. Each chip stands for one pattern. One or more chips can be dragged to the desired exposure area. Chip property needs to be specified for each chip, by right-click the chip. The “Job” pull-down menu allows the user to assign the chip to different jobs (mostly for dose test). “Position” asks for the coordinates of the chip center.

In “job settings” section, “job property” needs to be specified for each job included for this exposure. For each job, you can specify “pitch”, “shortrank table” and “calibration file”. “Pitch” is a secondary variable compared to “dosage”, meaning the distance between the neighboring beam dwelling points. The minimum value of “pitch” is also determined by the “EBW Helper”. “Shortrank table” is where you need to specify the dose for different data types. For example, if the base dose is set to be 300 $\mu C/cm^2$, and the modulation coefficient is 16.7 for data type 0 and 0 for data type 1, the dose for the area with data type 0 would be $300\times(1+16.7\%)=350\ \mu C/cm^2$, and the dose for the area with data type 1 would be the same as the base dose.

“Calibration file” should agree with the beginning of calibration procedure. It is worth noting that the selection of “default calibration file” (available in the pull-down menu) would cause the system to crash.

In our case, “pitch” should be set to 12 nm, and “calibration file” should be set to “M4_A2_1nA”, as shown in Fig. 23.

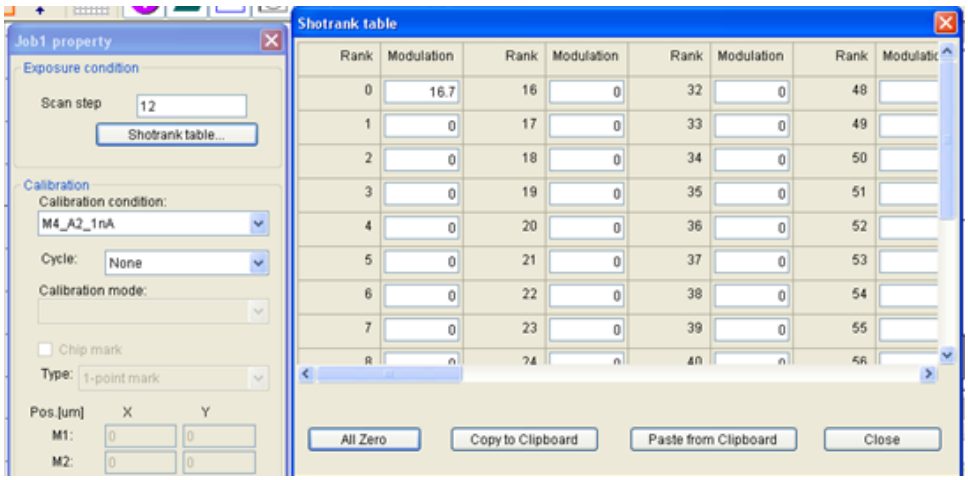

Fig. 23. Job property and shotrank table.

3.2.7 Development

After exposure, the sample is developed in the developer made from 100 mL IPA and 50 mL DI water for 1 minute with agitation. Then the sample is rinsed with DI water and blown dry with N_2 gun. It is critical that the developer is mixed fresh for each sample, to ensure the sample is well developed.

3.2.8 Post-exposure steps

An ashing procedure is carried out to remove the residue PMMA at the exposed area. Plasmalab System 100 from Oxford Plasma Technology is used. The RF power is 50W. The process temperature is 24°C and the process pressure is 10 mT. The oxygen flow rate is 20 sccm. The process time is 10 seconds.

Lesker PVD 75 electron beam evaporator is used to deposit 30 nm Ti as a mask layer for the pattern. The deposition rate is 1.0 A/s. Then the sample is submerged into a beaker with Acetone for 3 minutes, facing down. Then the beaker is transferred into a

sonicator to do 3 minutes sonication. After sonication, only the pattern area has the 30 nm Ti on the top, while the rest area is liftoff because PMMA is resolved in Acetone.

3.2.9 Trouble-shooting

(1) Metal peeling-off: The purpose of the Ti layer before EBL is to provide a conductive layer for the electrons to dissipate. Normally this layer is deposited using AJA sputtering system for 10 minutes. The thickness is measured to be around 45 nm. If the thickness of the Ti layer decreases, it is likely that the metal peels off during soft-baking step, or liftoff step.

(2) Stitching error: When the focus value of the E-beam writer is changed, it is necessary to re-run the "deflection correction" calibration procedure (as shown in Fig. 18). Otherwise, the system would not have the write-field size corrected accurately to 100 μm. As a result, the stitching error may occur in the form of "dent" or "gap" at the boundaries of each write field, shown in Fig. 24.

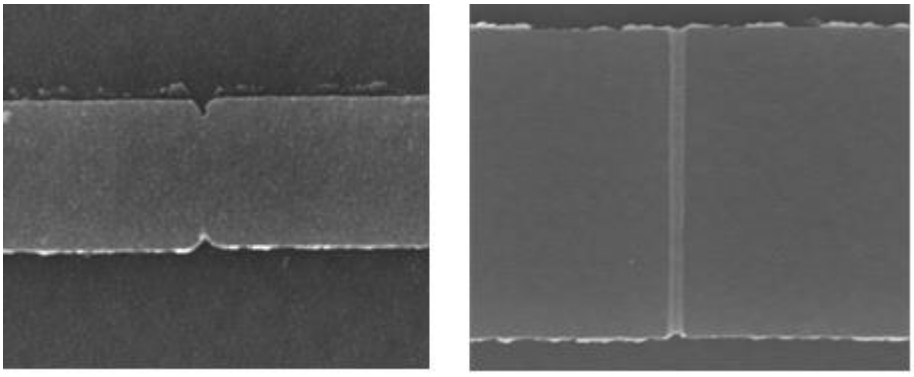

Fig. 24. Stitching error due to missing the step of deflection correction after focus adjustment

Another reason for the stitching error to occur is that the system is not capable of field-stitching. The most accurate mechanical stage has the translation accuracy of 1 μm. The stitching-enabled EBL system would have additional laser calibration to correct for the stage error, resulting in nanometer-scale stage accuracy. Fig. 25 below shows the random stitching error from the Tescan EBL system that does not have laser calibrated stage.

Fig. 25. Stitching error caused by the stage error.

(3) Liftoff time. For different materials as RIE mask layer, the liftoff time is significantly different. For example, when Cr is used as the mask layer, the liftoff step is 6 min in total, including 3 min sonication. When the Ti is used as the mask layer for the first time, the liftoff is incomplete, as shown in Fig. 26. So it is necessary to confirm under microscope that the metal is completely liftoff for each sample, especially when a new metal material is used.

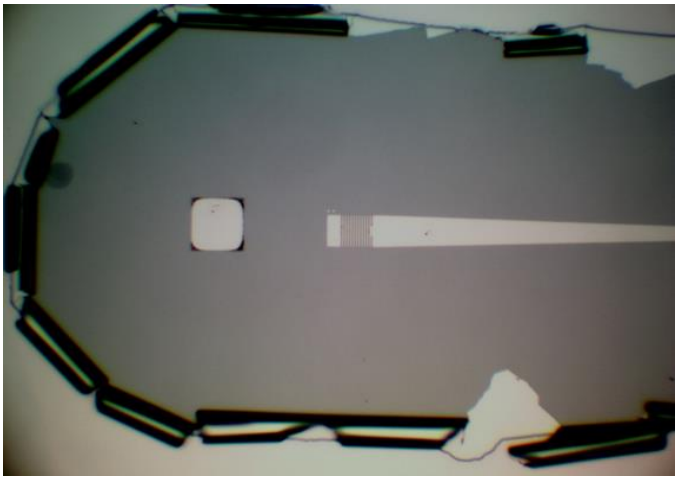

Fig. 26. The microscope image shows Ti liftoff incomplete.

(4) SEM changes the quality of the film. Theoretically, scanning electron microscope (SEM) step is non-destructive, as long as the liftoff step is complete. However, moisture in the SEM chamber may change the quality of the sample surface at the imaging area. Fig. 27 shows that the center area of the grating coupler is examined through SEM before RIE. Since the SEM alters the metal density, the RIE rate at the SEM-exposed area is changed, thus leaving a noticeable dot at the grating coupler area. So SEM should take place at the least desirable areas, or even at designated SEM pattern area.

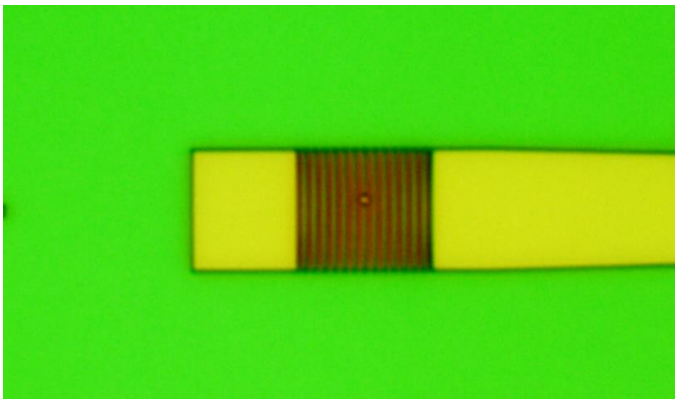

Fig. 27. Pattern changed due to RIE.

CHAPTER IV

RESULTS AND DISCUSSION*

4.1 As_2S_3-on-$LiNbO_3$ grating coupler

4.1.1 Device simulation

Fig. 28(A) illustrates the device configuration (top view), and Fig. 1(B) shows the grating coupler parameters. Here w_0 is the waveguide width at the narrow end of the adiabatic taper, whereas w_{GC} is the grating coupler width. Λ stands for the grating period.

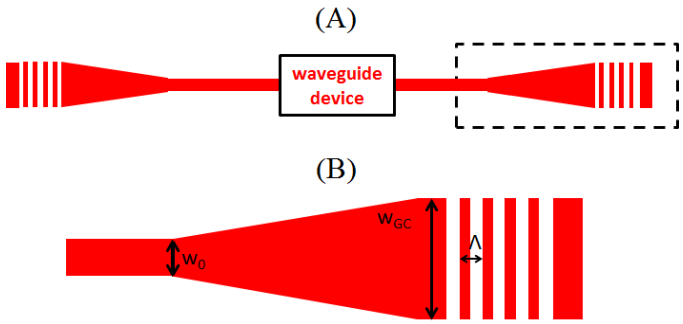

Fig. 28. (A) Bragg gratings device configuration; (B) Zoom-in view inside dashed box, with grating coupler and taper parameters.

---

* Part of this chapter is reprinted with permission from "Demonstration of an As_2S_3-on-$LiNbO_3$ grating coupler and its application of measuring a grating-based filter," Chen Zhang and Christi K. Madsen, *IEEE* Photonics Journal, 8(6) 2016, copyright 2016 by IEEE; DOI 10.1109/JPHOT.2016.2616220;

Part of this chapter is reprinted with permission from "Characterization of sidewall Bragg gratings using optical low-coherence interferometry with a broadband source," Chen Zhang, Xin Wang, and Christi K. Madsen, *Proc. SPIE* 9365, Integrated Optics: Devices, Materials, and Technologies XIX, 93651G 2015, copyright 2015 by SPIE; doi:10.1117/12.2080104; http://dx.doi.org/10.1117/12.2080104

Fig. 29 shows the material stack of the proposed grating coupler. X-cut bulk $LiNbO_3$ is the substrate. As_2S_3 and SiO_2 serve as the high and low refractive index material for Bragg reflector, respectively. The Al_2O_3 layer serves as the buffer oxide (BOX) layer, as well as the RIE stop layer. Another As_2S_3 layer on top of the BOX layer is the waveguide layer. A SiO_2 protective layer is used to prevent As_2S_3 from being oxidized.

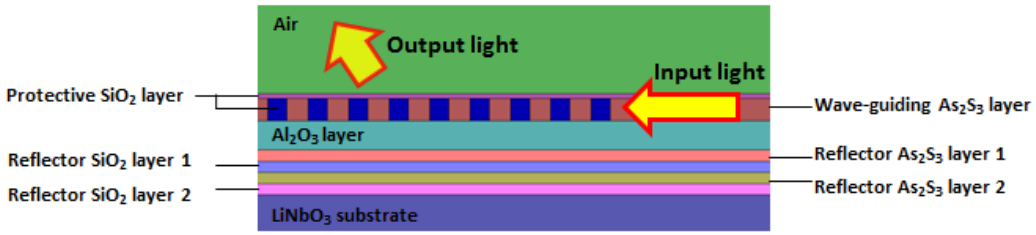

Fig. 29. Vertical coupling through grating coupler (side view).

Coupling efficiency is defined by Eq. (19) [25]:

$$\eta = \eta_{power} \times \eta_{overlap} \tag{19}$$

where η_{power} represents the percentage of the light that is encompassed by the area of SMF, while $\eta_{overlap}$ represents how much of the output light matches the Gaussian approximation of the SMF.

A complex effective index solver is used for 2-D grating coupler simulation. A Bragg reflector is used in order to minimize the light leakage into the substrate. Fig. 30 shows the output TE field of the grating coupler with and without a 4-layer Bragg

reflector at the bottom of the grating coupler. With the reflector, η_{power} is increased from 25.8% to 60.9%.

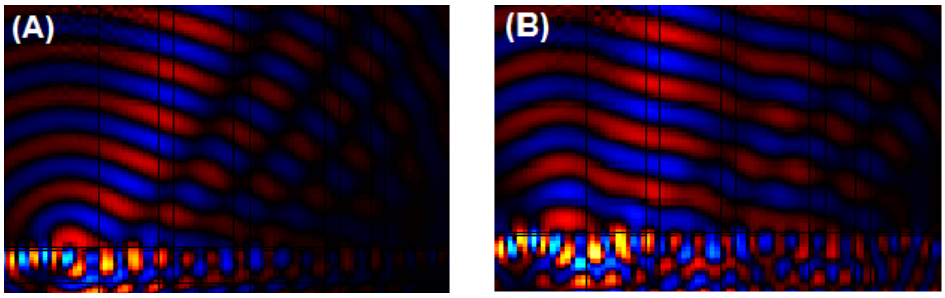

Fig. 30. Electric field (Ex) plots of grating coupler (A) without Bragg reflector, and (B) with Bragg reflector.

After iteration and convergence simulation, the optimized grating coupler parameters are finalized in Table 5. The coupling efficiency is calculated to be 55.6% at 1550 nm, with the bandwidth of 80 nm. The first three periods have different duty cycles in order to optimize $\eta_{overlap}$. Further improvement on the coupling efficiency could be achieved if amorphous silicon is used instead of As_2S_3 for the Bragg reflector, since amorphous silicon has a higher refractive index than As_2S_3, at the cost of depositing one more material in the fabrication process.

Table 5. Optimized grating coupler parameters.

Parameter	Value
Reflector SiO_2 layer 1 & 2 thickness	0.25 μm
Reflector As_2S_3 layer 1 & 2 thickness	0.25 μm
Al_2O_3 layer	0.65 μm
Wave-guiding As_2S_3 layer thickness	0.5 μm
Protective SiO_2 layer thickness	1.0 μm
Number of periods	11
Period	1.05 μm
Duty cycle of first three periods	0.76, 0.67, 0.48
Duty cycle of other periods	0.52

4.1.2 Device fabrication

A $LiNbO_3$ crystal wafer (x-cut y-propagation) is used as a substrate. After wafer dicing, the following thin film layers are deposited using AJA 1500 deposition system: 250 nm SiO_2, 250 nm As_2S_3, 250 nm SiO_2, 250 nm As_2S_3, 650 nm Al_2O_3, 500 nm As_2S_3, 100 nm SiO_2, and 45 nm Ti. The Ti layer serves as a conductive layer for EBL process.

PMMA C2 solution is used as E-beam resist. The spin speed is 2500 rpm, with 2 seconds ramping time. The soft-baking is carried out on a hotplate, at 180 °C for 2 min. A JOEL JBX 5500FS electron beam writer is used for patterning, in order to deliver sub-micron features. The acceleration voltage for this system is 50 kV. The beam current is 1

nA. The exposure dosage is 350 μC/cm^2. After exposure, the sample is developed for 1 minute in PMMA developer made from 100 mL IPA mixed with 50 mL DI water.

10-second ashing procedure is carried out using a Plasmalab System 100 (from Oxford Plasma Technology) to remove the residue PMMA at the corners of exposed areas. An E-beam evaporator (from Kurt J. Lesker Company) is then used to deposit 30 nm of Ti, followed by a lift-off step in Acetone.

SEM is employed to check the patterns non-destructively. Fig. 31 shows the SEM images for sample RC967, at one grating coupler region (A1) and one sidewall Bragg grating region (A44). For the grating coupler region, the linewidth is slightly wider than the design value due to electron proximity effect. With the same dose, the grating area turns out perfect.

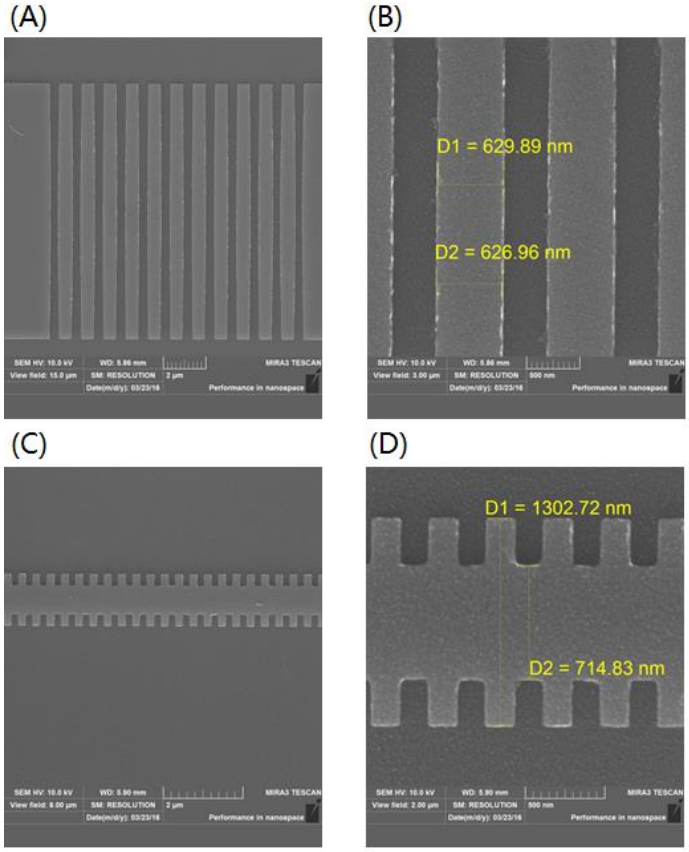

Fig. 31. SEM images of (A) grating coupler; (B) grating coupler zoom-in; (C) sidewall Bragg grating; (D) Bragg grating zoom-in.

After SEM, RIE is performed. The RIE time should be long enough to remove the As_2S_3 waveguide layer outside the pattern area. At the pattern area, the As_2S_3 waveguide layer should be preserved while the Ti layer should be completely removed. Fig. 32 shows the microscope images after 5 min, 7 min, 8 min and 8 min 45 s into RIE, respectively. It can be seen that at the beginning, the Ti layer is still remaining on the top of the grating coupler, so the pattern looks “shiny”. As the RIE goes on, the Ti layer is completely etched. And the grating coupler color transitions to dark, then yellow, which

is the color of the As_2S_3 wave-guiding layer.

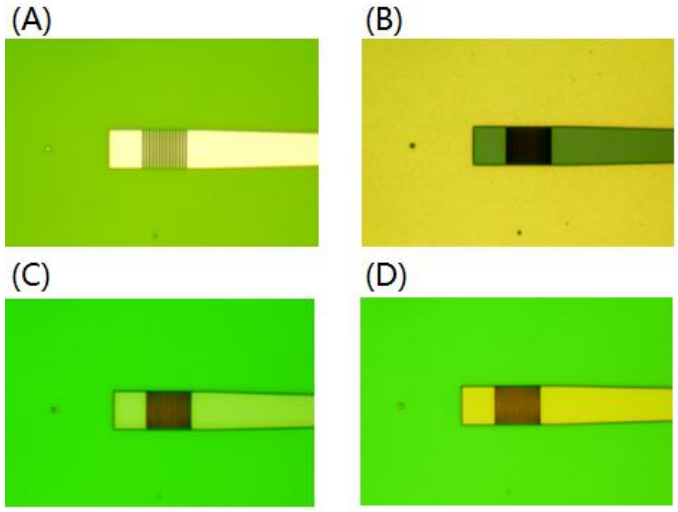

Fig. 32. Microscope images of device with different RIE time (A) 4+1min; (B) 4+1+1+1min; (C) 4+1+1+1+1min; (D) (4+1+1+1+1) min+45s.

The last fabrication step is to sputter 100 nm of SiO_2 cladding on top of the sample. To sum up fabrication steps, Fig. 33 shows the fabrication flowchart.

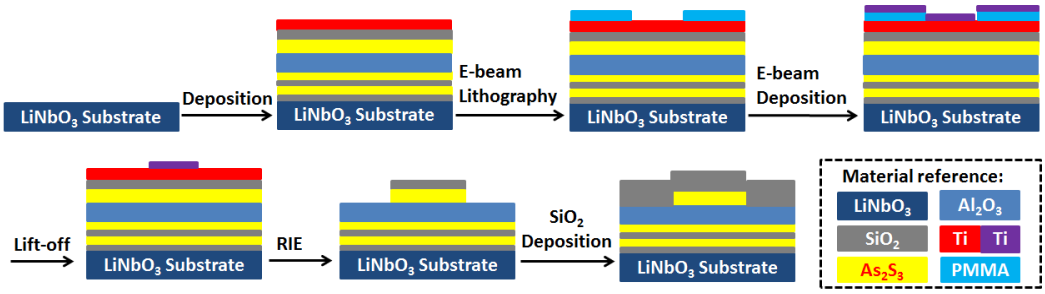

Fig. 33. Fabrication steps for the proposed device.

4.1.3 Device characterization and data analysis

Fabricated devices are characterized using the measurement setup shown in Fig. 34. A LUNA optical vector analyzer (OVA) is used to characterize the fabricated grating couplers. The coupling angle is set to 17°.

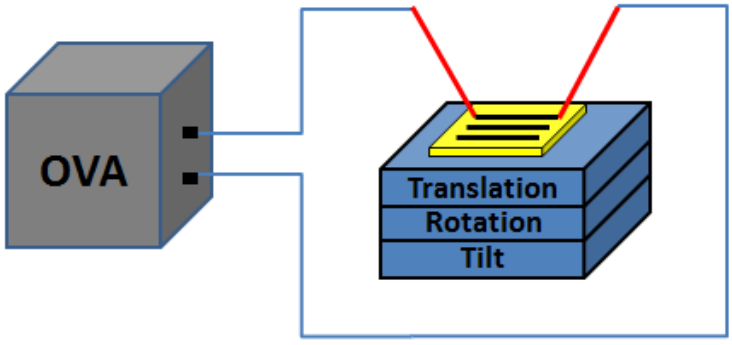

Fig. 34. Grating coupler measurement setup.

Fig. 35(A) shows the TE transmission spectrum of a 2 mm long waveguide with grating couplers on both ends. The insertion loss is 7.9 dB for TE polarization at 1563 nm. One reason for the transmission peak to shift towards longer wavelength direction is

that the grating coupler DC is larger than its designed value after lithography, causing n_{eff} to be larger. The loss results from grating couplers loss, adiabatic tapers loss, and waveguide loss. Fig. 35(B) is a zoomed-in version around the transmission peak. The 1 dB fringes are caused by the reflection of grating couplers. Back reflection is a common issue for fully etched grating coupler [24]. This issue can be partially resolved by tweaking the duty cycle of the first several periods of the grating coupler.

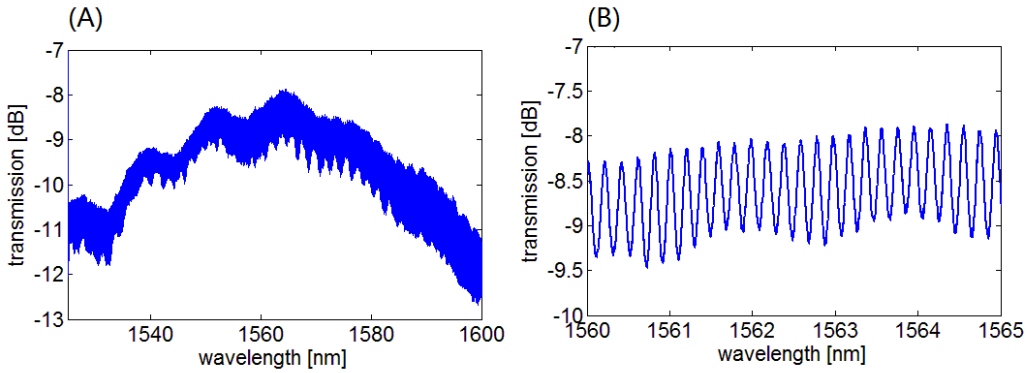

Fig. 35. (A) TE transmission response of the grating couplers; (B) Zoomed-in fringes at 1560-1565 nm.

Different Bragg grating structures are implemented in the "waveguide device" region in Fig. 3(A) and the devices are characterized through the As_2S_3 grating couplers. Fig. 36 is the plot of the TE reflection spectra of the fabricated Bragg gratings. Here, the number of periods is 1000, with period 356 nm. The waveguide width is 1.5 μm. The grating depths are 400 nm and 500 nm, respectively. The blue curves are extracted from the measurement results, with the grating coupler interference removed. The red curves are derived from CMT and fitting parameters are grating period, coupling coefficient and

the average effective refractive index of the grating area. From the fitted results, the coupling coefficient is 6.0 mm^{-1} for 400 nm deep gratings and 10.0 mm^{-1} for 500 nm deep gratings. The coupling coefficient is higher than previous results published on the same platform [15], due to the stronger refractive index perturbation from the different grating geometry.

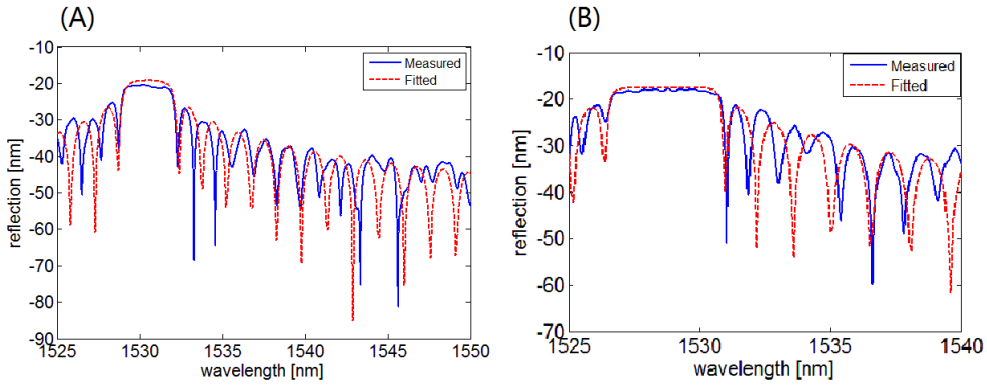

Fig. 36. Reflection spectra and fitted curves for grating depths of (A) 400nm, and (B) 500nm.

A Bragg grating cavity can be implemented by cascading two segments of Bragg gratings with a waveguide cavity in between them. Such a cavity is also characterized using the As_2S_3 grating couplers. Fig. 37(A) shows the TE transmission spectrum of the fabricated grating cavity, with the cavity length 1 mm. On each end of the cavity, the sidewall Bragg grating has a 356 μm coupling length and a 300 nm grating depth. The full width at half maximum (FWHM) at the resonance wavelength of 1532 nm is 0.0375 nm and the free spectral range (FSR) is 0.36 nm. The measurement spectral resolution is 0.0025 nm. The roundtrip loss of the cavity is calculated to be 47.7% from Eq. (20) [44],

where 1-ρ is the roundtrip loss.

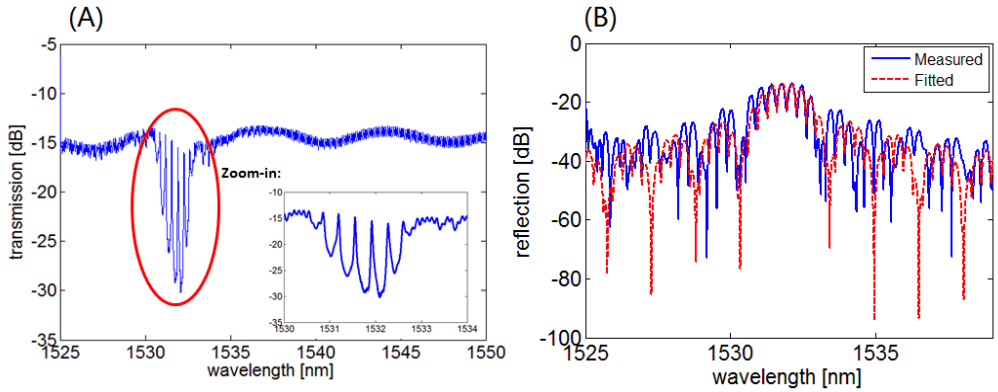

Fig. 37. (A) Grating cavity transmission spectrum; (B) grating cavity reflection spectrum (blue) and fitted curve (red).

$$\frac{FSR}{FWHM} = \frac{\pi}{2\arcsin\left(\frac{1-\sqrt{\rho}}{2\sqrt[4]{\rho}}\right)} \tag{20}$$

Fig. 37(B) shows the TE reflection spectrum of the same grating cavity, with the fitted result. The extracted waveguide propagation loss from the curve-fitting is 2.0 dB/cm. Given the cavity roundtrip loss of 47.7%, the grating reflection at the resonance wavelength is 92.1%.

Assuming the waveguide loss is wavelength-independent, and neglecting the loss introduced by the adiabatic tapers, the grating coupler loss is calculated to be 3.75 dB. The main reason for the value to differ from the theoretical value is due to the fabrication imperfection of the Al_2O_3 layer and the grating coupler patterning distortion due to electron beam proximity effect. Improvement on Al_2O_3 deposition and

characterization is on-going. And proximity correction can be applied in order to minimize the grating coupler distortion from the patterning step.

4.1.4 Summary

In summary, an As_2S_3 grating coupler with a Bragg reflector between the waveguide layer and the substrate is demonstrated. The fabrication procedure consists of a single lithography step and a single etching step, making it a cost-efficient and highly repeatable process. The resulting grating coupler loss is estimated to be 3.75 dB per coupler, which is comparable to results for silicon photonics. Sidewall Bragg gratings and grating cavity results are also demonstrated using the same coupling method. The coupling coefficient for 0.356 mm Bragg gratings with 500 nm grating depth is 10.0 mm^{-1}. The Bragg grating cavity filter was fabricated, with transmission FWHM at the resonance wavelength to be 0.0375 nm.

The proposed As_2S_3 grating coupler opens door to numerous application on As_2S_3-on-$LiNbO_3$ platform with low fabrication cost. Compared to SOI platform, the As_2S_3-on-$LiNbO_3$ platform has up to 90 times higher modulation speed as well as much lower loss [18]. So the grating coupler on such platform is a real enabler for high-speed, low-loss beam steering using integrated optics.

4.2 As_2S_3 grating coupler on thin film $LiNbO_3$

4.2.1 Thin film $LiNbO_3$ substrate

The technology development of thin film $LiNbO_3$ enables ultra-compact electro-optic (EO) devices such as photonic crystal EO modulator and EO switch [31, 45-47]. With the device size reduction, the modulator gain-bandwidth product is maximized.

Thin film $LiNbO_3$ is created by using ion implantation, or ion slicing, to create crystal damage at the desired depth of bulk $LiNbO_3$ wafer, followed by wet etching or thermal annealing. The most cost-effective way to create such thin film is to use wet etching to exfoliate the film [48]. The typical film size acquired using this method is 10 μm thick, and 1 cm × 3 mm in area. Then the film can be bonded to Si substrate through epoxy. Thermal annealing can also be used for exfoliation, which would result in sub-micron thickness film. And full wafer process has been demonstrated using this method [31].

The above methods both require a bonding procedure. One way to create $LiNbO_3$ film-based device without bonding is to create suspended $LiNbO_3$ devices through ion beam enhanced etching [49].

To compare these three methods, the first two methods required a sample bonding step, which will complicate fabrication procedure. The third method doesn't require bonding, but it requires multiple ion implantation attempts, which will make the fabrication cost higher. The final product of method 2 is of the desired thickness and capable of wafer-scale fabrication, whereas method 3 can only produce micron-level width. Table 6 compares the three methods in terms of fabrication complexity, fabrication cost, film thickness and area, and device design flexibility.

Table 6. Comparison of different methods to create thin film $LiNbO_3$.

	Ion slicing + wet etching	Ion slicing + thermal annealing	ion beam enhanced etching
Fabrication complexity	Bonding required	Bonding required	2 ion implantation steps
Fabrication cost	Fair	Fair	Very high
Film thickness	10 μm	Sub-micron	Sub-micron
Film area	1 mm × 3 mm	Wafer scale	50 μm × 1 μm
Device design	Flexible	Flexible	limited by area

In order to reduce fabrication cost, $LiNbO_3$ thin film on Si wafer is directly purchased, and the wafer material stack is shown in Fig. 38.

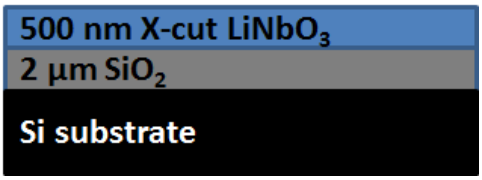

Fig. 38. Material stack of the thin film $LiNbO_3$ wafer.

4.2.2 Device simulation

The parameters for As_2S_3 grating coupler on thin film $LiNbO_3$ is the same as the definition in section 4.1.1 (Fig. 3). The side views of two design structures are shown in

Fig. 39. Fig. 39(A) shows the optimized design, where all the optimization techniques including apodizing grating periods, Bragg reflector and As_2S_3 controlled etching, are applied. Design 2 in Fig. 39(B) does not apply the controlled As_2S_3 etching technique.

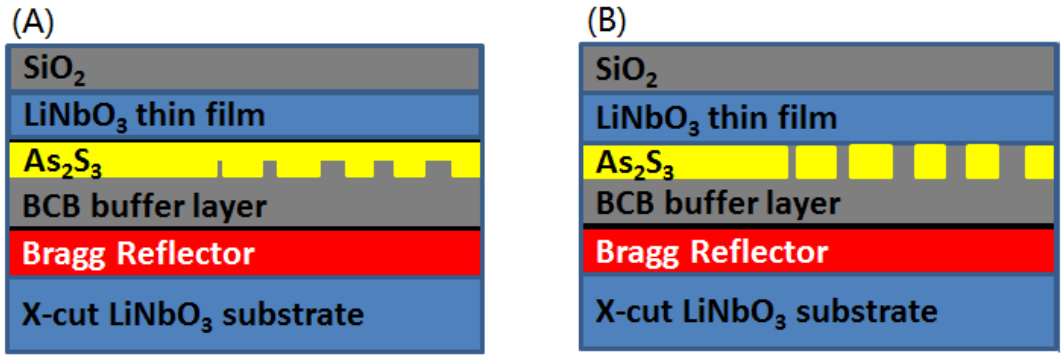

Fig. 39. Two As_2S_3-on-$LiNbO_3$ film designs: (A) design 1; (B) design 2.

The Bragg reflector consists of three As_2S_3 and SiO_2 thin film pairs, in order to minimize the light leaked through the sample. The fine controlling of the buffer layer is also critical for constructive interference between the top and bottom diffractive light.

Benzocyclobutene (BCB) can be used as the buffer layer material. BCB has been widely applied to low temperature wafer level bonding, with good adhesion, easy fabrication, repeatable thickness and refractive index control [50, 51]. According to The Dow Chemical Company documents [52], Cyclotene (3022-46) should be used, with curing temperature 250°C for 60 minutes. The film refractive index after curing is 1.535 at 1550 nm.

500 nm As_2S_3 thin film layer serves as the waveguide and grating coupler material for design 1. The film is deposited and patterned on top of the commercially available $LiNbO_3$ thin film substrate, as discussed in the previous section. Then the patterned thin film $LiNbO_3$ wafer is bonded with BCB-covered wafer, followed by BCB curing procedure. For design 2, 400 nm As_2S_3 thin film is deposited. Other parameters are the same as in design 1.

The simulation is carried out using Fimmprop. For TE polarization light, the coupling efficiency is maximized at 14° coupling angle. The electric field for the TE polarization is shown in Fig. 40 below.

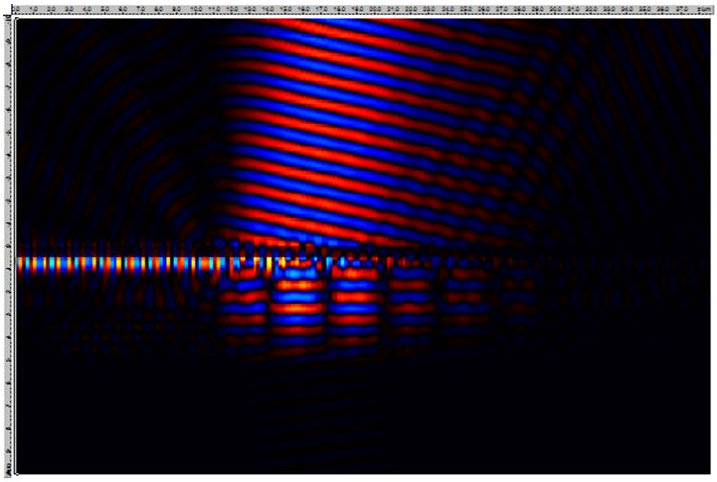

Fig. 40. Ex at 1550 nm for design 1.

Fig. 41 shows the coupling efficiency of the grating couplers with different BCB thicknesses. It can be seen that the as the BCB thickness increases, coupling efficiency changes periodically, bonded by 0 and 0.8. The reason for this periodicity is that the

BCB thickness determines whether the diffracted light from the top of the BCB and the bottom of the BCB interfere constructively, or destructively, or in between.

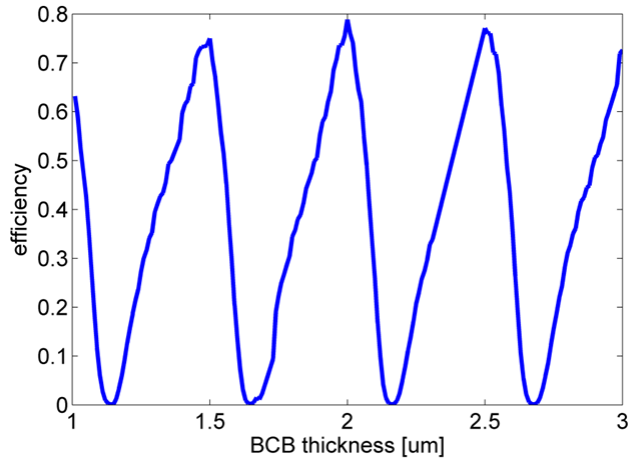

Fig. 41. Coupling efficiency variation with different BOX thicknesses.

Fig. 42 below shows the grating coupler spectral response. The solid curve is the spectral response of the optimized structure with the Bragg reflector on the bottom, while the dashed curve is the spectral response of the same grating parameters without the Bragg reflector on the bottom. It is worth noting that the peak coupling efficiency (80.6%) is at 1545 nm rather than 1550 nm for design 1, because there are a lot of variables for the design, and each variable is discrete in the simulation with practical considerations. The limitation for the coupling efficiency is around 82% with this Bragg reflector, where the overlap efficiency is approaching 1. The 3-dB bandwidth for design 1 is 60 nm.

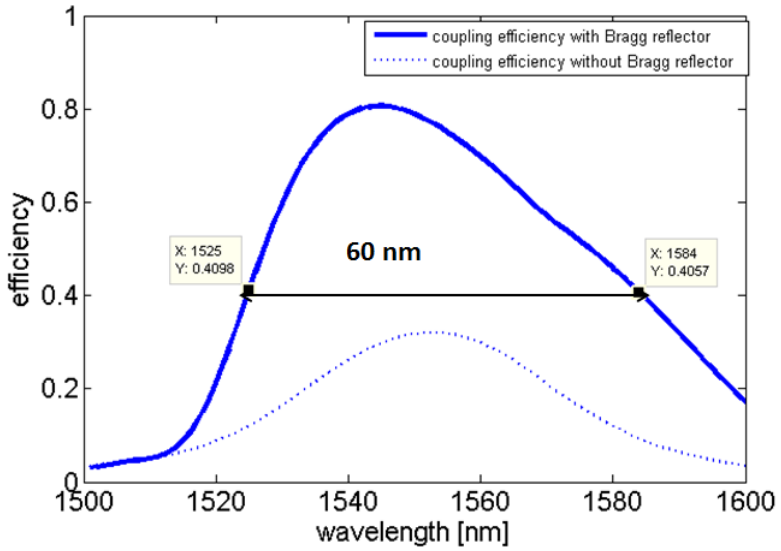

Fig. 42. Grating coupling efficiency with reflector and without reflector.

Design 1 employs As_2S_3 waveguide layer controlled etching, in order to maximize the coupling efficiency of the grating coupler. This etching requirement adds to fabrication cost. On the other hand, the fabrication of design 2 is simplified in the sense that As_2S_3 layer is etched all the way. The coupling efficiency is decreased to 58.0% in this case. The coupling angle is changed due to the fact that effective index of the grating coupler is changed. Table 7 shows the key parameters for both designs.

Table 7. Comparison between design 1 and design 2.

	Design 1	Design 2
As_2S_3 thickness in Bragg reflector	130 nm	
SiO_2 thickness in Bragg reflector	340 nm	
BCB thickness (n=1.535)	2 μm	
As_2S_3 thickness for grating layer	500 nm, 100 nm	400nm
Thin film $LiNbO_3$ thickness	500 nm	
Grating coupler period	850 nm	
Grating coupler duty cycle	0.94, 0.82, 0.70, 0.59	0.90, 0.85, 0.75, 0.59
Number of periods	2, 2, 2, 16	2, 2, 2, 11
Coupling angle from normal	14°	11°
Coupling efficiency	78.8%	58.0%

If further sacrifice of coupling efficiency is acceptable, the grating couplers can be positioned directly on the commercial thin film $LiNbO_3$ substrate. The material stack is shown in Fig. 43 below, for both cases. Here, they are named design 3 and design 4, respectively.

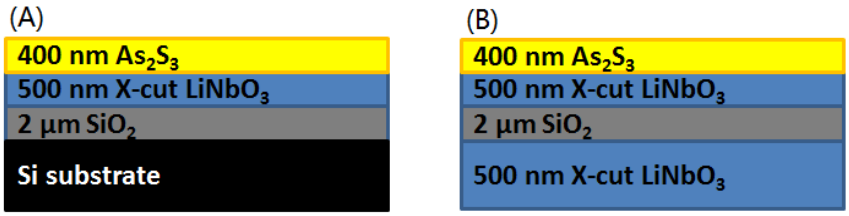

Fig. 43. The material stack for: (A) design 3; and (B) design 4.

After design optimization, the design parameters for design 3 are listed in Table 8.

Table 8. Grating coupler parameters for design 3.

Parameter	Value
As_2S_3 thickness	400 nm
Grating coupler period	850 nm
Number of periods	2,2,2,10
Duty cycle*	0.88, 0.82, 0.7, 0.59
Coupling angle	14°

The efficiency comparison among different designs is listed in Table 9. By comparing design 1 and design 4, the coupling efficiency is reduced by 38% without the Bragg reflector and controlled etching technique. Design 3 with Si substrate gives

slightly better result than design 4 with $LiNbO_3$, owing to the larger refractive index contrast between Si substrate and SiO_2.

Table 9. Fabrication cost vs. efficiency for all the designs.

	Design 1	Design 2	Design 3	Design 4
Deposition layers	10	10	4	4
Requires BCB bonding	Yes	Yes	No	No
Requires controlled etching	Yes	No	No	No
Requires substrate removal	Yes	Yes	No	No
Coupling efficiency	78.8%	58.0%	53.0%	49.8%

4.2.3 Fabrication procedure

The fabrication flow chart for design 1 is shown in Fig. 44. The top part of the grating coupler device start with As_2S_3 deposition (along with SiO_2 & Ti protective layer deposition) on $LiNbO_3$ thin film substrate. Then The EBL is used to define the grating coupler pattern. During RIE step, the etching time should be controlled so that the shallow layer has 400 nm As_2S_3 removed, while the pattern area preserve the 500 nm As_2S_3.

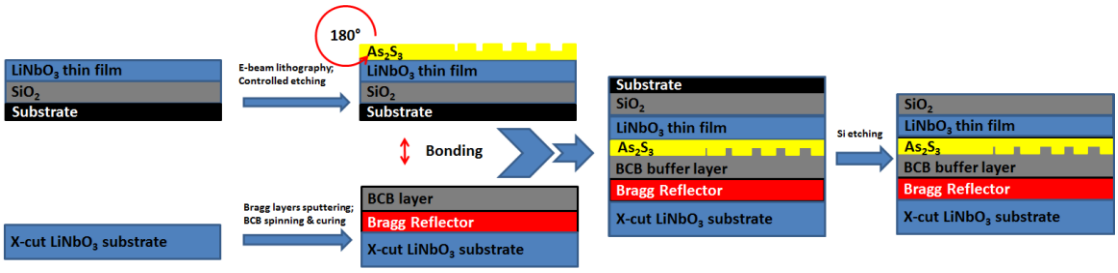

Fig. 44. Fabrication of grating coupler design 1 (side view).

The bottom part of the grating coupler device starts with deposition of As_2S_3 and SiO_2 thin films as the Bragg reflector, according to Table 7. Then the BCB solution is spin-coated and curing temperature 250°C for 60 minutes. Then more BCB solution is spin-coated, before the top part covers the solution, with As_2S_3 in contact with BCB. Then the whole device is cured at the same environment, for it to be well bonded. The last step is to remove the Si substrate for optical testing.

Compared to the complex fabrication procedure for design 1, design 3 is much easier to realize. The fabrication of design 3 starts with cleaning the sample using Q-tip with Acetone, Methanol, and IPA, in this order. Then the sample is deposited with 400 nm As_2S_3, 130 nm SiO_2 and 40 nm Ti. Then EBL is used to pattern the sample. Since the sample comes in 10 mm × 10 mm squares, the margin for sample mounting should be minimized (1 mm) in order to save enough space for the pattern. The orientation of the sample requires extra attention, since the design is on y-propagation $LiNbO_3$ thin film, as shown in Fig. 45. Before exposure, it is critical to specify the accurate coordinates of the pattern, to make sure that it falls right at the center of the sample, where the PMMA layer has uniform thickness.

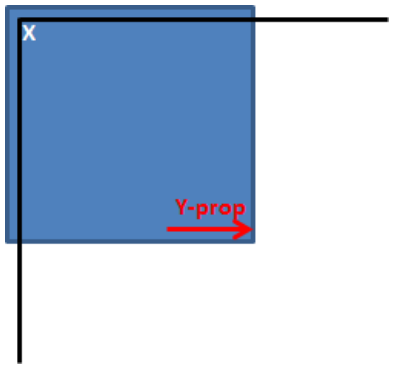

Fig. 45. Small sample mounted on EBL cassette.

The developing step after exposure has been covered in section 3.2.7. Here the only difference is that since the sample is small and light, it is not convenient to use a Teflon boat. A pair of flat-head tweezers should be used to hold the corner of the sample, and gentle agitation should also be applied.

After ashing and Ti evaporation, the small sample needs to be mounted to the carrier substrate by Kapton tape during liftoff procedure (Fig. 46).

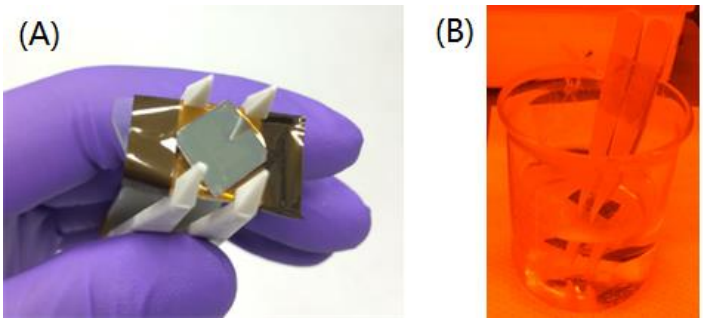

Fig. 46. (A) The sample is mounted to the carrier substrate; (B) liftoff.

The above discussion focuses on the fabrication steps that are different from section 4.1.2. A complete fabrication flow chart for design 3 is shown in Fig. 47.

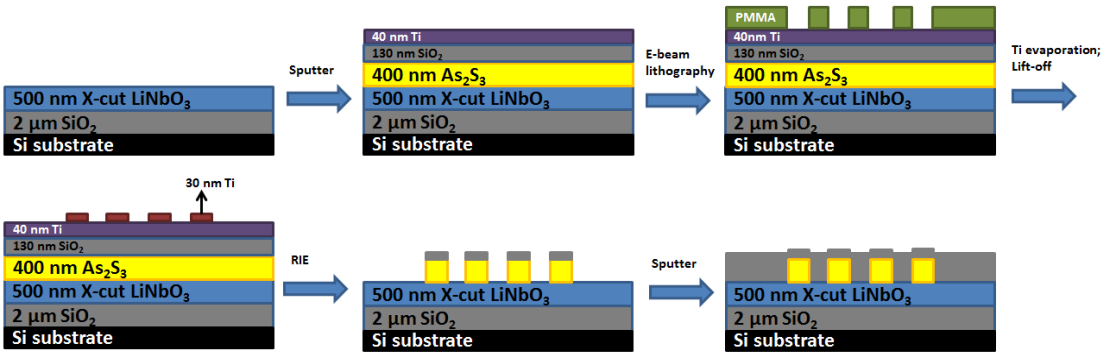

Fig. 47. Fabrication of grating coupler design 3 (side-view).

4.2.4 Results and discussions

The measurement setup is the same as the one described in section 4.1.3, except that the coupling angle is 14° from the vertical direction. The sample is put ton top of a larger silicon wafer for easier transfer, as shown in Fig. 48.

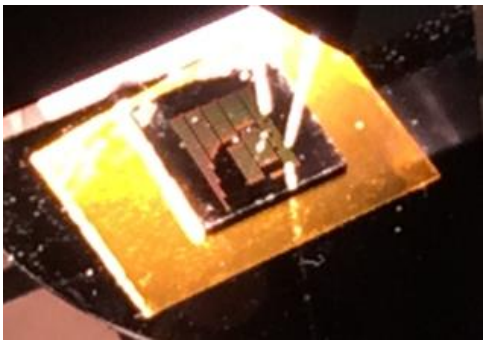

Fig. 48. Measurement of the thin film $LiNbO_3$ chip.

Fig. 49 shows the insertion loss of 2 mm long, 1.0 μm wide As_2S_3 waveguide with different duty cycles, using design 3 grating coupler. Here, the grating coupler period is 0.85 μm. Due to the fabrication imperfection, the peak transmission wavelength is shifted to the shorter wavelength range. As a rough estimation, the propagation loss at 1540 nm (the measured transmission peak) is 2.0 dB/cm. Assuming the mode conversion loss in both tapers is negligible and the waveguide loss is wavelength-independent, the lowest fabricated grating coupler loss is calculated to be 6.3 dB at 1540 nm.

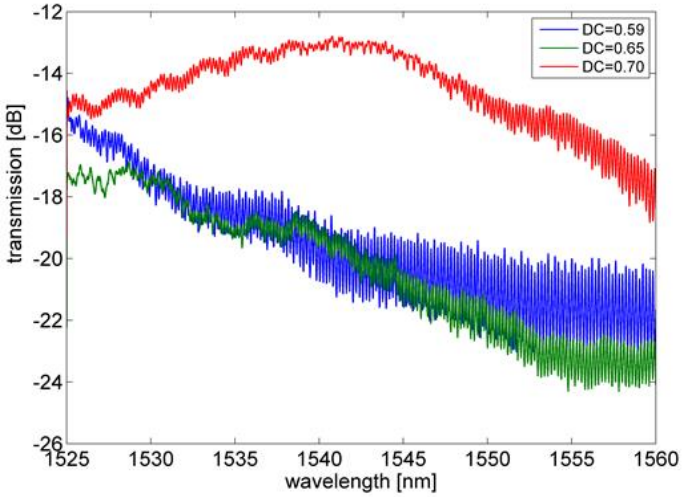

Fig. 49. Insertion loss of design 3 grating couplers with different lengths of As_2S_3 waveguides.

Design 3 can be used to measure grating cavity structure on a thin film $LiNbO_3$ wafer. With electrode patterned on both sides of the cavity waveguide, it becomes EO tunable filters. The grating cavity reflection response can be extracted by truncation of

the time domain device reflection (including grating coupler), followed by inverse Fourier transformation. Fig. 50 shows the reflected spectrum of one fabricated FP cavity extracted in this manner. This device is constructed by 1000 periods of sidewall Bragg gratings, with period of 360 nm and grating depth of 200 nm. The cavity length is 3 mm and the cavity width is 1 μm. The fitted result in Fig. 50 is calculated by implementing CMT and TMM with the fitting parameters listed in Table 10.

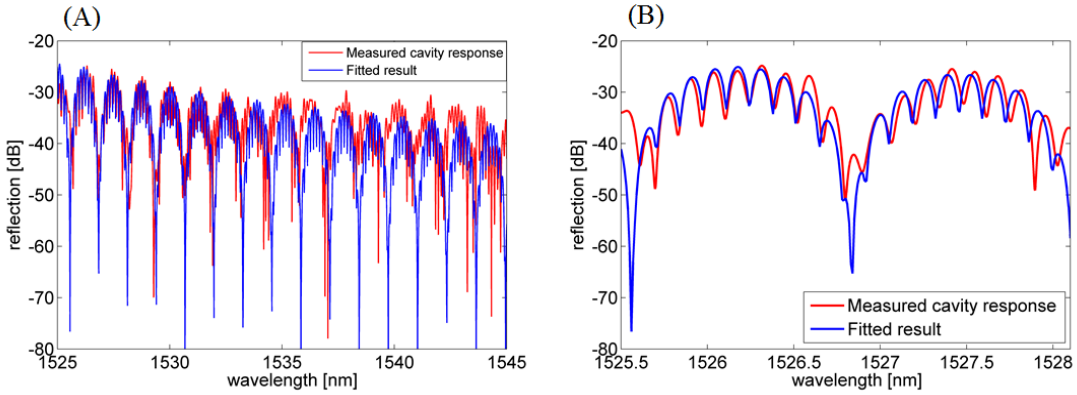

Fig. 50. (A) Reflected spectrum of a fabricated grating cavity device; (B) Zoom-in view.

Table 10. Fitting parameters for the grating cavity reflection response.

Fitting parameter	Value
Coupling coefficient	0.85 mm^{-1}
Effective refractive index	2.11
Group refractive index	2.6
Waveguide loss	2 dB/cm

Mode confinement factor in $LiNbO_3$ layer is a key parameter. The higher confinement factor in $LiNbO_3$ layer means higher EO tuning efficiency of the grating cavity, since $LiNbO_3$ crystal is the only EO tunable material in this structure. By decreasing As_2S_3 waveguide width, confinement efficiency in $LiNbO_3$ thin film can be effectively increased, as shown in Fig. 51. At 400 nm waveguide width, the confinement factor as high as 82.3% is achieved.

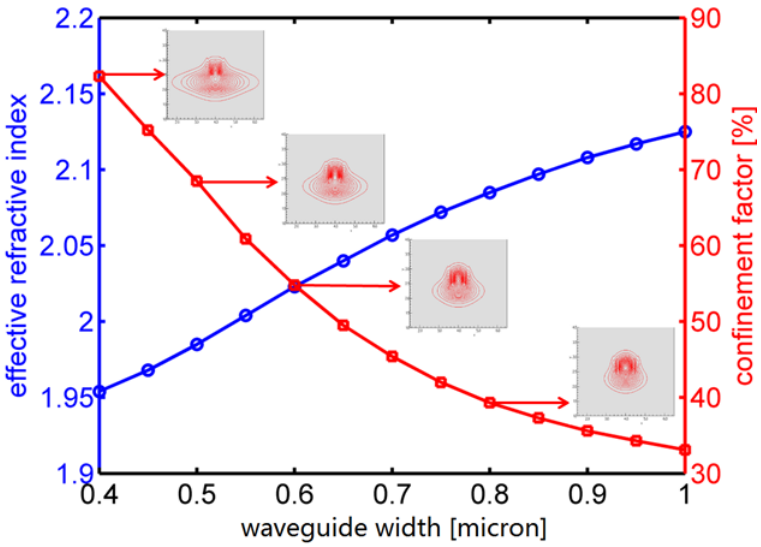

Fig. 51. Effective refractive index and confinement factor of the hybrid optical mode is changed with the change of As_2S_3 waveguide width.

Several improvements can be made towards lowering the grating coupler insertion loss. First, the grating period and DC need to be tweaked from the design values based on the current experimental results, since the actually materials and their refractive indices are off from the material database to some extent. Second, longer taper

could be included in order to further reduce mode-conversion loss. Third, the throughput of the devices should be higher in order to draw more convincing conclusions from larger device population.

4.3 Electro-optic probe for electric field measurement

4.3.1 Background

Strong electric field (E-field) measurement is needed in power system and military applications. One method of E-field measurement is to use EO material such as $LiNbO_3$ crystal. By quantifying the change of refractive index of $LiNbO_3$ crystal with the presence of E-field, one could calculate the amplitude of that field.

There are several types of E-field probes that are based on $LiNbO_3$ crystal: common path interferometer (CPI), Mach-Zehnder interferometer (MZI), evanescence field coupler, etc. Two approaches are especially feasible on $LiNbO_3$ substrate: Ti-diffused waveguide CPI and annealed proton exchanged (APE) waveguide MZI.

E-field probes based on Ti-diffused waveguide CPI require a linear light input into the single-mode waveguide. When there is no E-field, the output light has a certain polarization state that is determined by the waveguide refractive indices on both TE and TM polarizations. When E-field is applied along y-axis, the refractive indices on both polarizations are changed by different values, resulting in a different polarization state output light. APE-based probes do not require a linear light input because APE waveguide does not support TM mode. By electrically shielding one arm of MZI and expose the other arm into a strong E-field, the output light would be intensity modulated. The following sections are going to discuss them in more details.

4.3.2 Ti-diffused CPI E-field probe

Fig. 52 shows the fundamental modes for both polarizations in Ti-diffused waveguide that supports only one TE mode and one TM mode. The refractive index of TE fundamental mode is 2.140394. The refractive index of TM fundamental mode is 2.211325.

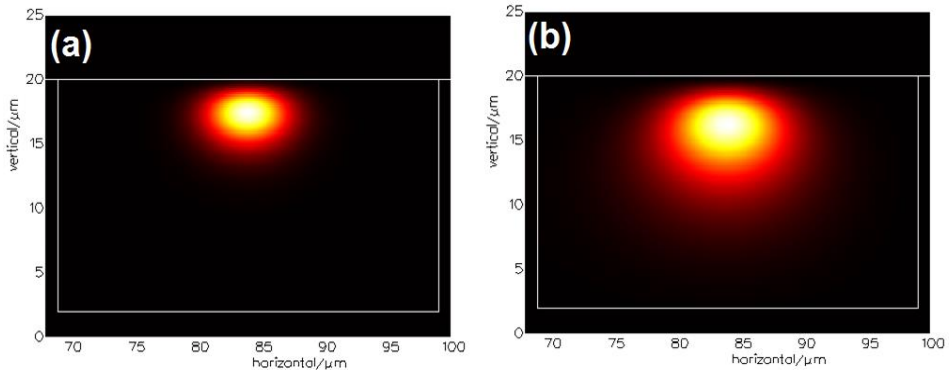

Fig. 52. (a) TE fundamental mode; (b) TM fundamental mode.

Coplanar strip electrodes are used to create the E-field. Aluminum (Al) is chosen as electrode material and Al thickness is 500 nm. The ground pad is 80 μm wide. Another 8 μm wide Al pad is placed 8 μm away from the ground pad and connected to -10V. Fig. 53 shows the cross-section of the Ti-diffused CPI probe.

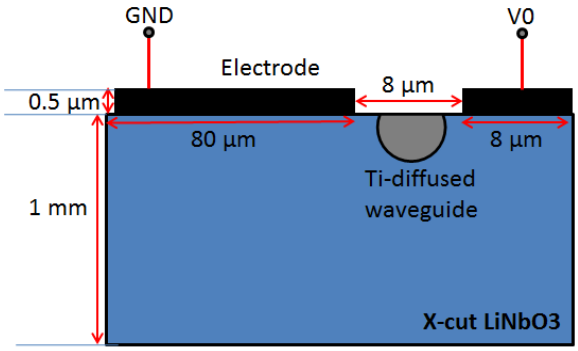

Fig. 53. The geometry of the Ti-diffused CPI senor.

Fimmwave EO solver from Photon Design Inc. is used to calculate the electric field generated by the coplanar strip electrodes and to simulate the optical property change of the $LiNbO_3$ substrate. The E-field contour is shown in Fig. 54. The maximum E-field strength generated is 1.1 MV/m. The average E-field strength at the TE fundamental mode area is approximately 0.23 MV/m.

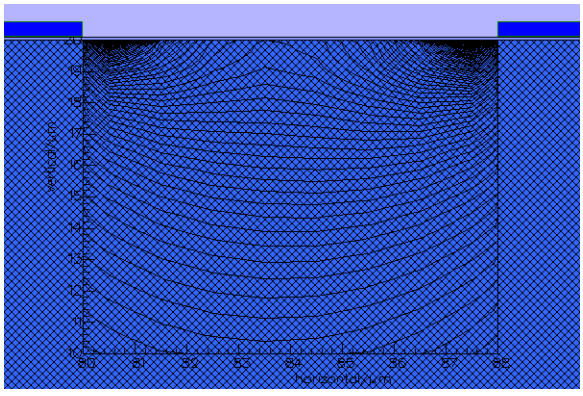

Fig. 54. Electric field contour solved by the EO solver.

Then finite difference method (FDM) is used to calculate the effective index change for both TE (Δn_{TE}) and TM (Δn_{TM}) polarizations under this electric field. Optical path length difference between TE and TM polarization is thus given by the following equation:

$$OPD_{pol} = (\Delta n_{TE} - \Delta n_{TM}) \times L_{pad} \tag{21}$$

where L_{pad}=6 mm (determined by the photo mask) is the length of the electrode. The relative phase shift can be calculated:

$$\Delta\varphi = \frac{OPD_{pol}}{\lambda} \times 2\pi \tag{22}$$

In our case, the phase shift between TE and TM polarizations caused by the applied E-field is:

$$\Delta\varphi = \frac{(\Delta n_{TE} - \Delta n_{TM}) \times L}{\lambda} \times 2\pi = 0.23\pi \tag{23}$$

As a result, the π phase shift voltage can be calculated:

$$V_{\pi} \times L = \frac{1}{0.23} \times 5V \times 6mm = 0.13Vm \tag{24}$$

Fig. 55 illustrates the fabrication steps for Ti-diffused E-field probe. First, an X-cut Z-propagation $LiNbO_3$ wafer is diced. Then 95 nm Ti film is DC sputtered, shown in Fig. 55(A). Photolithography is then conducted in order to define Ti strip for diffusion, shown in Fig. 55(B). After RIE and resist stripping, the sample looks like Fig. 55(C). Then the sample is placed in furnace at 1035°C for 10 hours in a wet breathing air atmosphere. Fig. 55(D) shows the sample after diffusion. 160 nm SiO_2 is then sputtered for isolation, and 500 nm Al is sputtered as electrode material. A second

photolithography step is carried out to open window for Al electrodes. RIE is then performed to define the electrodes shapes, followed by resist stripping. The complete device is illustrated in Fig. 55(H).

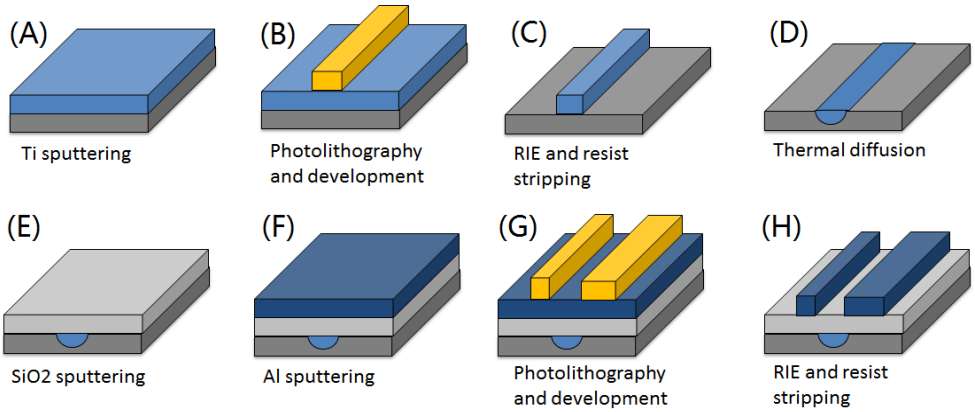

Fig. 55. Ti-diffused sensor fabrication steps.

Polarization analyzer SK010PA-IR can be used to detect the polarization state change of the input light. The measurement setup is shown in Fig. 56.

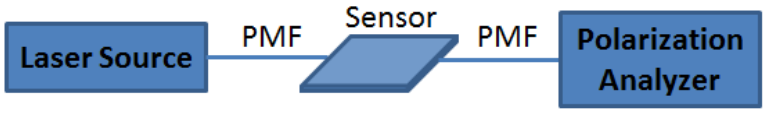

Fig. 56. Ti-diffused CPI sensor setup.

State of polarization (SOP) accuracy of the polarization analyzer is $\pm 0.2°$ on Poincare sphere [53]. Angle of the elliptically polarized light is given by [54]:

$$\chi = 0.1^\circ \tag{25}$$

Ellipticity angle can also be expressed by phase delay between TE and TM polarizations due to EO tuning:

$$\chi = \tan^{-1}\left(\frac{\sqrt{(E_x \cos\frac{\pi-\Delta\varphi}{2})^2 + (E_y \cos\frac{\pi+\Delta\varphi}{2})^2}}{\sqrt{E_x^2 + (E_y \cos\Delta\varphi)^2}} \right) = \tan^{-1}\left(\frac{\Delta\varphi_{\min}}{\sqrt{2}} \right) \tag{26}$$

As a result, $\Delta\varphi_{\min} = 7.8\times10^{-4}\pi$ is the minimum detectable polarization dependent phase difference. Minimum and maximum detectable E-field strength is then given by [55]:

$$E_{\min} = \frac{\Delta\varphi_{\min}\lambda\varepsilon_{33}}{\pi n_e^3 r_{33} L} = 18.69\,kV/m \tag{27}$$

$$E_{\pi} = \frac{\lambda\varepsilon_{33}}{n_e^3 r_{33} L} = 26.45\,MV/m \tag{28}$$

4.3.3 Thin film $LiNbO_3$ CPI probe

An alternate way to create mode confinement in $LiNbO_3$ is to use As_2S_3 strip waveguide on top of thin film $LiNbO_3$ CPI probe. In section 4.2, grating couplers on thin film $LiNbO_3$ is discussed. They can be used to couple into the As_2S_3 strip waveguide with low loss.

In bulk $LiNbO_3$, there has been thorough research on As_2S_3-$LiNbO_3$ hybrid mode. Similar research is still on-going for thin film $LiNbO_3$. As_2S_3 provides mode confinement for input light at 1550nm, while still a portion of light is in the thin film $LiNbO_3$ to take advantage of EO property of $LiNbO_3$. Fig. 57 shows the As_2S_3-on-thin

film $LiNbO_3$ hybrid mode with the waveguide width to be 1.0 μm. In this case, the mode confinement in the thin film $LiNbO_3$ is 28.5%.

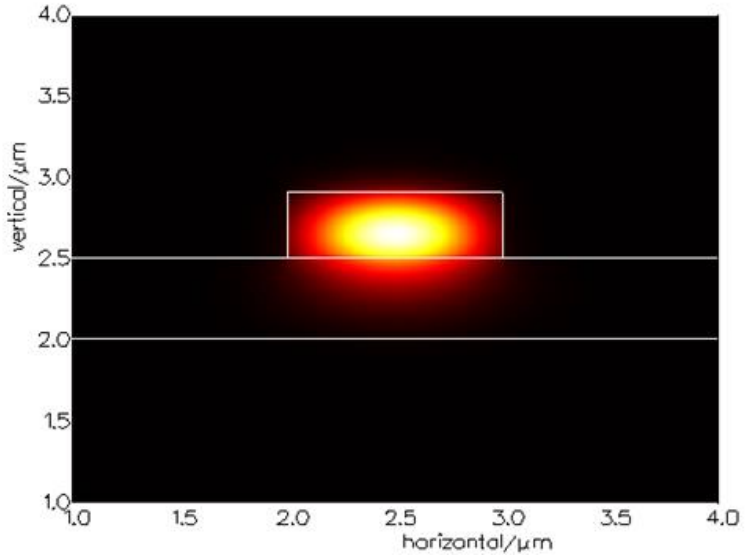

Fig. 57. As_2S_3-on-thin film $LiNbO_3$ hybrid mode.

Fig. 58 shows two possible geometries of the hybrid waveguide structures. Fig. 58(A) is the X-cut thin film $LiNbO_3$ with coplanar electrode configuration; Fig. 58(B) is the Z-cut thin film $LiNbO_3$ with sandwich electrode configuration. Both electrode configurations take advantage of r_{33} EO coefficient of $LiNbO_3$, with maximum EO tuning capability.

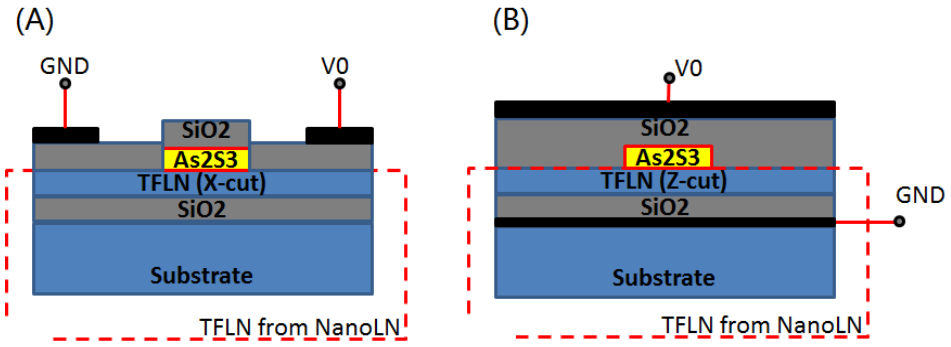

Fig. 58. Two possible geometries of the hybrid EO waveguide structures.

It is critical to design As_2S_3 waveguide geometry so that the hybrid structure only supports one TE mode and one TM mode. In this specific case, minimum waveguide thickness should be chosen so that TM fundamental mode exists in such waveguide. On X-cut thin film $LiNbO_3$, As_2S_3 waveguide should be 0.5 μm thick and 1.6 μm wide, whereas on Z-cut thin film $LiNbO_3$, As_2S_3 waveguide is 0.55 μm thick and 1.6 μm wide. Similar EO simulation is performed on both configurations. The results are summarized in Table 11.

Table 11. Sensor parameters comparison among different design methods.

Method	Ti-diffused waveguide with co-planar electrode CPI	X-cut thin film $LiNbO_3$ with co-planar electrodes CPI	Z-cut thin film $LiNbO_3$ with parallel electrodes CPI
Voltage	5 V	5 V	5 V
Electrode separation	8 μm	8 μm	3.25 μm
Electrode length	6 mm	6 mm	6 mm
TE phase shift	0.000039	0.00001	0.000003
TM phase shift	0.000009	0.000005	-0.000009
Electric field strength	625 kV/m	625 kV/m	1.54 MV/m
$V\pi \times L$	0.13 V▪m	0.02 V▪m	0.052 V▪m

It can be seen that although Z-cut thin film $LiNbO_3$ CPI has smallest electrode separation, the phase shift is not as big as bulk $LiNbO_3$ CPI design, although both cases utilize r_{33} EO coefficient of $LiNbO_3$. The main reason is that the confinement factor of light in As_2S_3 is high in order for single TE mode and single TM mode to exist in the hybrid waveguide.

4.3.4 $LiNbO_3$ slab coupled D-fiber probe

The critical question to answer for $LiNbO_3$-based E-field probe is how to couple the light into $LiNbO_3$, or how to have greater portion of light mode overlap with $LiNbO_3$, in order to have higher probe sensitivity. The previous two design methods use direct end-coupling and vertical grating coupler, respectively, to make the light interacting with the $LiNbO_3$ material, either the bulk substrate or the thin film layer.

The previous two sections discuss the feasibility of realizing E-field probe with integrated photonic structures. As a result, such probes inherit the merits of the integrated photonics: compact, mature and well developed fabrication steps. However, the cost of fabrication, especially material deposition, lithography and high-temperature diffusion, is high.

Motivated by cost reduction, we seek a different coupling method to enable efficient light interaction with $LiNbO_3$ crystal. Prism coupling method was first introduced in 1970 [56-58]. It is a powerful tool to characterize thin film through evanescence coupling. The first demonstration of side-polished fiber [59], or the so-called "D-fiber", enables the fiber mode to be evanescence-coupled to a thin film. Evanescence coupling makes optical testing easier than prism coupling method. Gibson et al have applied the D-fiber into E-field sensing [60-62] and were able to achieve sensitivity as high as 1.6 μW▪m/MV using $LiNbO_3$ slab coupling with D-fiber.

The coupling between a $LiNbO_3$ slab waveguide and a D-fiber is approximated by the following equation [60]:

$$\lambda_m = \frac{2t}{m}\sqrt{n_{LN}^2 - n_f^2} \tag{29}$$

where λ_m is the resonance wavelength; m is the order of slab mode; t is the slab thickness; n_{LN} and n_f are refractive indices of the $LiNbO_3$ and the fiber mode, respectively.

If we plug in $LiNbO_3$ refractive indices for both polarizations, with the thickness of the $LiNbO_3$ slab to be t=275 μm, transmission FSR for both polarizations can be calculated:

$$\begin{aligned} \Delta\lambda_{TE}(\lambda = 1550nm) &= 2.8nm \\ \Delta\lambda_{TM}(\lambda = 1550nm) &= 2.6nm \end{aligned} \tag{30}$$

The relationship between the transmission and the phase mismatch is expressed in Eq. (31) [60]. Here, c is the coupling coefficient; Δk is the phase mismatch for different wavelengths.

$$T = 1 - \frac{C^2}{C^2 + \Delta k^2 / 4} \tag{31}$$

Fig. 59 is the plot for Eq. (31). It can be concluded that the FWHM decreases with weaker coupling. However, the minimum coupling length is inversely proportional to the coupling coefficient [60]. This means that if the design goal is to have the deep, sharp transmission notch, longer coupling length and smaller coupling coefficient is desired.

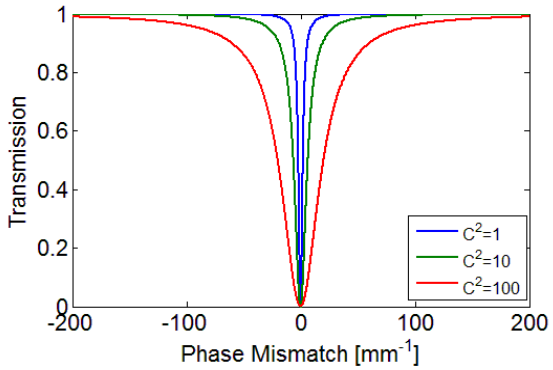

Fig. 59. Transmission with different phase mismatch values.

Table 12 compares the sensors based on the three methods previously described. Note that the fabrication cost for the first two methods are high. The challenge for method 3 is packaging fragile D-fiber with $LiNbO_3$ slab.

Table 12. Comparison among different sensors.

Method	Ti-diffused $LiNbO_3$ CPI sensor	CPI sensor in [55]	Resonance between D-fiber and slab [62]
Waveguide length	6 mm	20 mm	10 mm
Eπ	24.04 MV/m	2.15 MV/m	20 kV/m
Sensitivity	18.69 kV/m	10 kV/m	200 V/m
Fabrication procedure	2 lithography steps; Ti diffusion.	2 lithography steps; Ti diffusion.	0 lithography step; D-fiber bonding.
Critical issues	Low sensitivity	Electrode design	D-fiber fragile

In order to initially demonstrate the coupling between the $LiNbO_3$ slab and the D-fiber, we built the following test setup in Fig. 60. Here, the polished surface of the D-fiber is facing upwards and 1 – 2 μm from the fiber core; liquid index matching gel (n=1.45) is applied between the glass slide and the $LiNbO_3$ slab. The x-cut $LiNbO_3$ slab is 275 μm thick and 4 mm long.

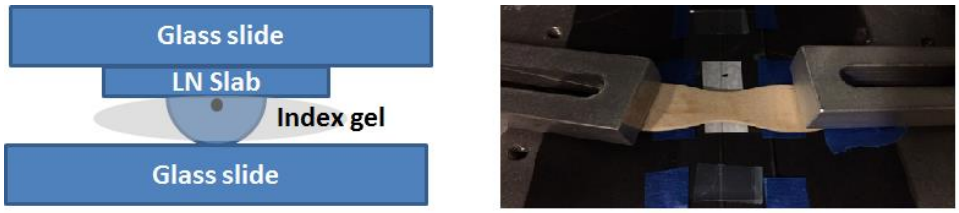

Fig. 60. Initial D-fiber packaging attempt.

Initial test results with this structure are shown in Fig. 61. A polarization-resolved wavelength scan shows the transmission relative to the reference configuration. LUNA OVA is used for measurement. The reference measurement is taken without the $LiNbO_3$ slab. Measurement 2 and 3 have the same coupling region, with different coupling strengths (by applying different pressures). Measurement 1 is taken at a different coupling location along the D-fiber from Measurements 2 and 3. The coupling strength between the D-fiber and the $LiNbO_3$ slab is dependent on the coupling region, as well as pressure applied to the coupling region. The slab mode coupling is evident from the transmission spectra. Around 1550 nm, the FSR for measurement 2 is 2.58 nm (TM) and 2.69 nm (TE); the FSR for measurement 3 is 2.55 nm (TM) and 2.62 nm (TE).

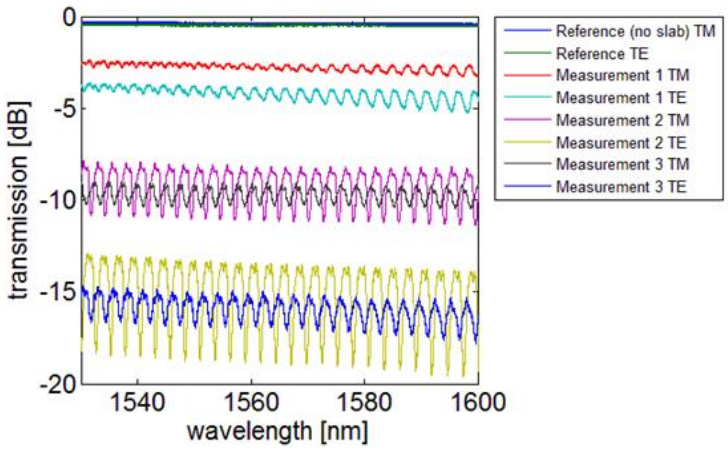

Fig. 61. Transmission spectra for different D-fiber LN slab coupling measurements.

Several conclusions can be drawn here: First, without $LiNbO_3$ slab, insertion loss values for both polarizations are low (~0.5 dB) and there is no polarization separation despite of the asymmetry D-fiber. Secondly, the measurement result, particularly the insertion loss, is dependent on the coupling region. Thirdly, different pressure (within reasonable range) does not affect the insertion loss too much; instead it causes the FWHM of the notches to vary a lot and the resonance wavelength to shift. The measurement has excellent time stability.

When the external voltage is applied to the sensor, the equation needs to be re-written in the following form:

$$\lambda_m = \frac{2t}{m}\sqrt{(n_{LN} + \frac{1}{2}n_z^3 r_{33} E_z)^2 - n_D^2} \qquad (32)$$

where r_{33}=30.8 pm/V can be taken advantage of only for TE polarization in our case (or for TM polarization with Z-cut $LiNbO_3$ slab). The wavelength shift at the resonance wavelength can be derived by taking derivative on both sides of Eq. (32):

$$\Delta\lambda_m = \frac{t}{m}\frac{(n_z + \frac{1}{2}n_z^3 r_{33}E_z)n_e^3 r_{33}\Delta E_z}{\sqrt{(n_z + \frac{1}{2}n_z^3 r_{33}E_z)^2 - n_D^2}} = k\Delta E_z \tag{33}$$

The zoomed-in spectrum around 1550 nm of measurement 2 for TE polarization is shown in Fig. 62, with the linear-unit y axis.

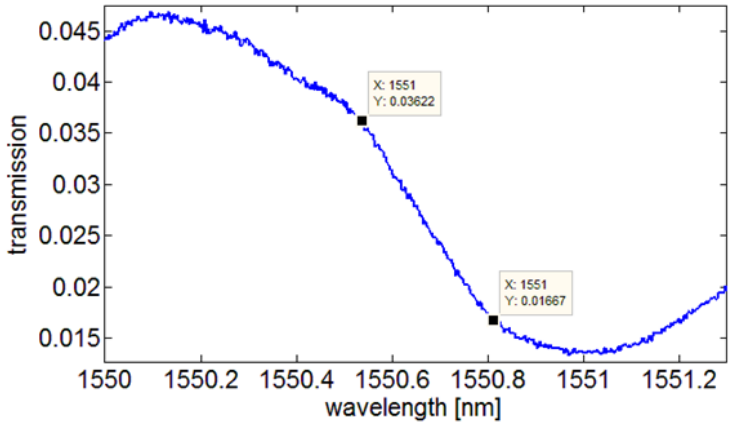

Fig. 62. Tranmission spectrum and its linear region.

The linear wavelength range is 0.2725 nm, with the transmission varying from 3.62% to 1.67%. The output power change with variable applied E-field is thus given by Eq. (34), where P_L is the laser power.

$$\Delta p = \frac{k\Delta E_z}{0.2725nm} \times P_L(3.62\% - 1.67\%) \tag{34}$$

If n_z=2.1376, E_z=675 kV/m, and m=557 are plugged in,

$$\Delta p = 1.446\times10^{-8}\, m/V \times P_L \times \Delta E_z \tag{35}$$

The dynamic range for this sensor is determined by the linear wavelength range is calculated in Eq. (36).

$$\Delta E_{\max} = \frac{\Delta \lambda_{linear}}{k} = 1.35 MV / m \tag{36}$$

The sensitivity can be quantified using the ratio of output laser power change to the E-field change. If the laser power is chosen to be 80 μW (corresponding to the quiescent power 2.1 μW in the work in [62]), the sensitivity (S) is calculated:

$$S = \frac{\Delta p}{\Delta E_z} = 1.156 \mu W \bullet m / MV \tag{37}$$

This result is smaller than the value 1.6 μW▪m/MV reported by Gibson et al. The direct cause of the difference is that the transmission in [62] has a steeper slope (8.1 μW/nm) than our measurement (5.72 μW/nm). So it is critical to maximize the slope value during the packaging process. Another way to potentially increase the slope is to have a thinner $LiNbO_3$ slab so that the coupling mode should have less interference with each other due to larger transmission FSR.

The next step is to develop a stable and repeatable packaging strategy for this E-field probe. SolidWorks is used to design a 2-part package to enclose the optical coupling area of the probe, with UV-sensitive epoxy at the gap between $LiNbO_3$ slab and polished surface of D-fiber. Fig. 63 below shows the top and bottom part of the package design. The four holes are for Nylon screws to hold the two pieces together. The screws enable tunable pressure at four corners for better evanescence coupling.

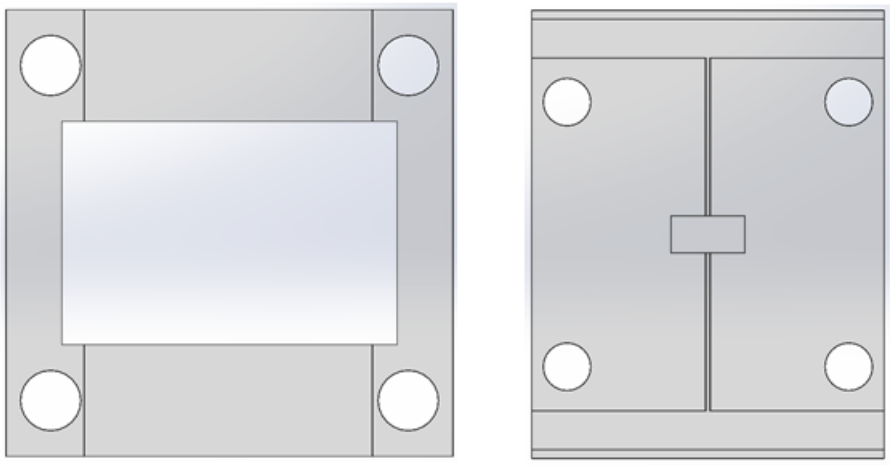

Fig. 63. Packaging of D-fiber LN slab coupler.

Norland optical adhesive is used to fill the coupling region between a side-polished fiber and an X-cut $LiNbO_3$ slab with 275 μm thickness. After best coupling is reached by careful adjusting each of the four Nylon screws, we shine UV lamp through the top window to cure the epoxy. Since the coupling region is bonded by cured epoxy as well as four screws, the time stability of the probe is good. Fig. 64 is the picture of the coupling region of the probe after packaging.

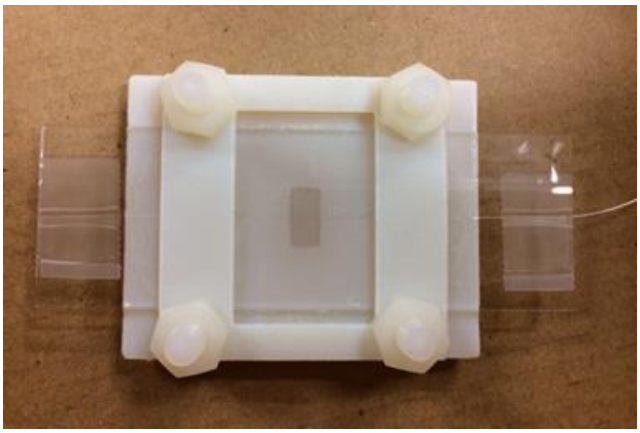

Fig. 64. Optical coupling region of the probe after packaging.

Since OVA is not suitable for low-cost measurement, we try to use distributed feedback (DFB) laser to scan the wavelength range that gives the best probe sensitivity. Fig. 65 shows the measurement configuration.

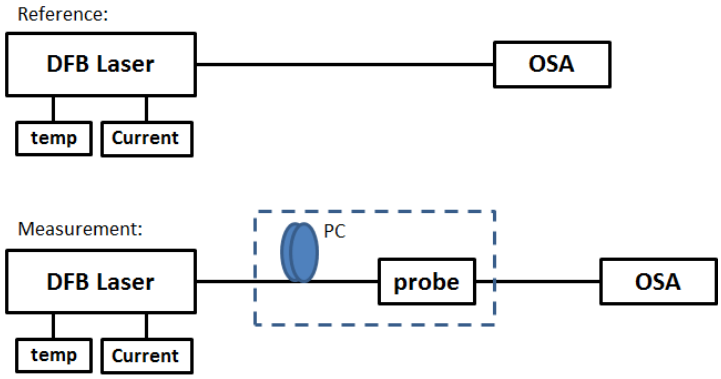

Fig. 65. Optical measurement of the probe with DFB laser and OSA.

We uses DFB laser as the source, because we can tune its wavelength through thermal control, as well as current control. Additional, it offers the future possibility of

probe miniaturization. Due to the fact that both wavelength tuning methods would result in output power change, a reference measurement is done at every data point in order to calculate the insertion loss of the probe. A polarization controller (PC) is inserted in front of the probe, providing additional capability of sensitivity improvement by changing the polarization state of input laser light. We use optical spectrum analyzer (OSA) as a temporary option, which would be replaced by a photodiode at the target wavelength in the future.

The thermal tuning of the DFB laser is applied first, so that the steepest slope of the spectral response of the probe can be used for high sensitivity of the probe. Then current tuning is applied for data acquisition. Fig. 66 shows the DFB measurement result, compared to the tunable laser and OVA measurements. Here, the insertion losses are normalized. It can be observed that the rising trend of DFB laser measurement result agrees with both tunable laser measurement and OVA measurement at 1531.42 – 1531.5 nm wavelength range. It can also be observed that DFB measurement has much steeper slope, because the input polarization state is better tuned.

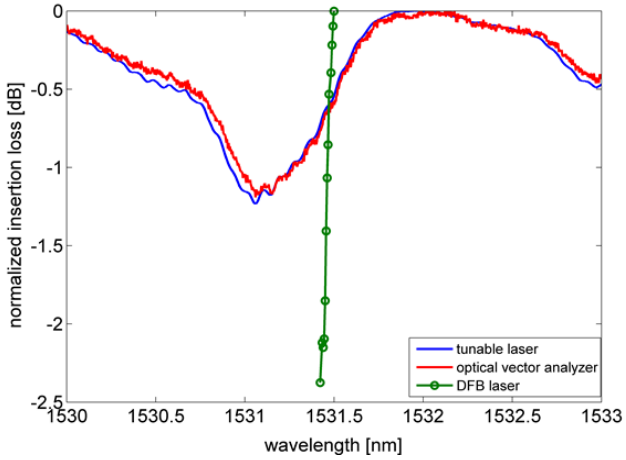

Fig. 66. Normalized insertion loss with tunable laser, OVA, and DFB laser.

Probe sensitivity can be calculated using the DFB measurement result in linear scale, as shown in Fig. 67. The slope can be written as the ratio of transmission to wavelength change, which is directly related to probe sensitivity. Assuming the laser power of 2.1 μW (the same as in [62]), the sensitivity of this probe can be quantified by the linear transmission slope, which is 10.5 μW/nm. This value is higher than 8.1 μW/nm reported in [62], indicating that the sensitivity of this probe is 29.6% higher than 1.6 μW▪m/MV.

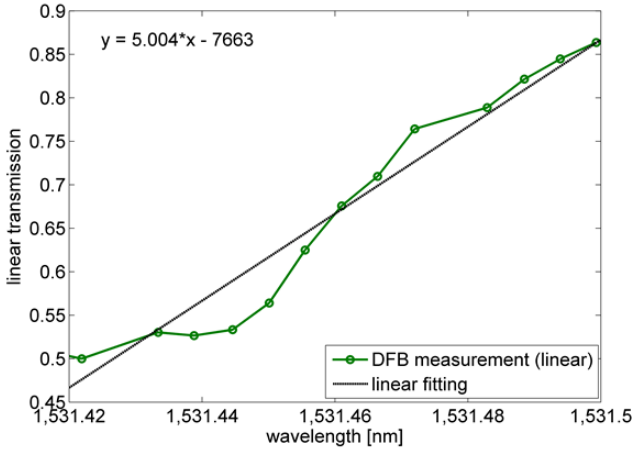

Fig. 67. Zoomed-in of tuning range of the DFB laser measurement, in linear scale.

4.4 OLCI setup for measurement on As_2S_3-on-$LiNbO_3$ platforms

In Fig. 12, low-coherent light on the top-left corner is generated from a supercontinuum source passing through a neutral density filter and a bandpass filter, as shown in Fig. 68. A 1315 nm reference laser is added from the other input to calibrate the translation speed of the mirrors.

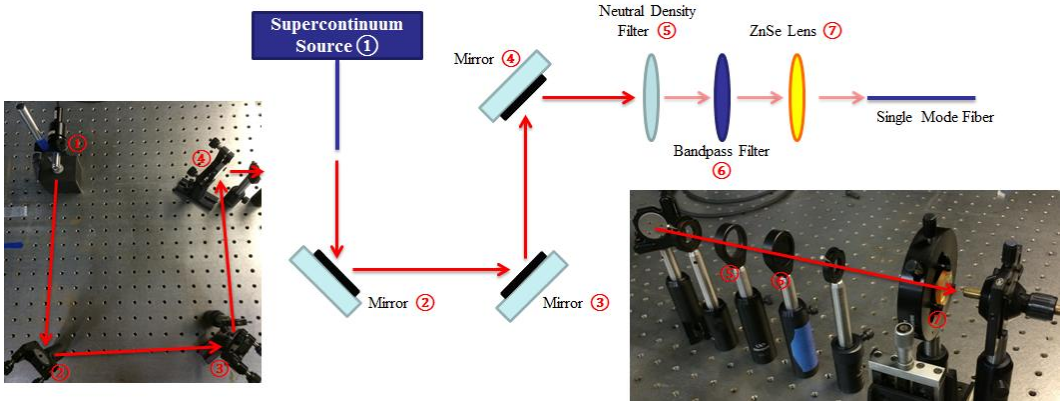

Fig. 68. Low coherence source generation.

The beams are combined at the input using a multiplexer (MUX). The combined beam is split by a 3 dB coupler. One beam from the coupler goes through a collimator, a variable delay line, and is coupled back to another collimator. The other beam from the coupler goes through a fixed length of SMF. A DUT can be inserted in the reference arm. The two beams are then combined by another 3 dB coupler at the output. The combined beam is separated by wavelength using a de-multiplexer (DMUX), and different wavelengths are detected using different photodetectors (PD).

Fig. 69 show the optical spectrum analyzer results of following cases: without any filter, with only the neutral density (ND) filter, and with a ND filter and a bandpass filter. The neutral density filter used is made of KG2 glass, and it attenuates the pass-through light by 5 dB. The reason to introduce a neutral density filter into this system is to avoid detector saturation. The bandpass filter has a center wavelength of 1550 nm, and FWHM of 40 nm.

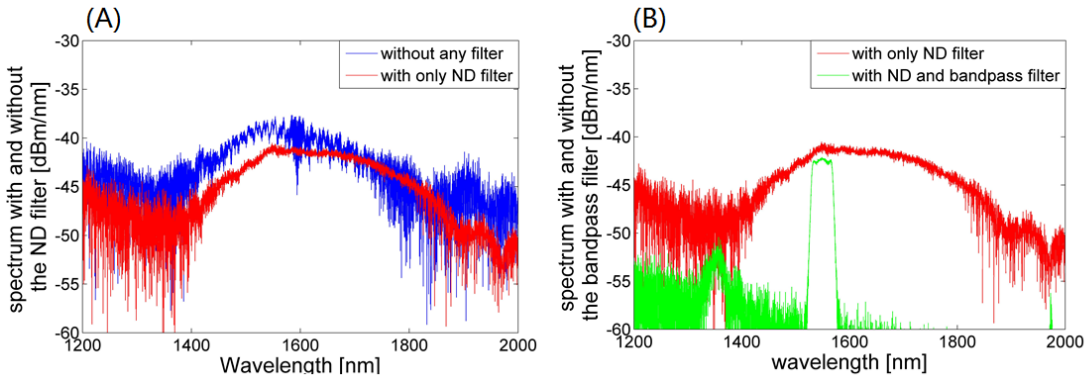

Fig. 69. Optical spectrum analyzer results: (A) with and without the ND filter; (B) with and without the bandpass filter.

Fig. 70 (A) shows the fringe patterns of the supercontinuum source, and Fig. 70 (B) shows the spectrum calculated from the fringe pattern, compared with the spectrum measured from a commercially available spectrum analyzer. It can be observed that the calculated spectrum fits the measured spectrum well.

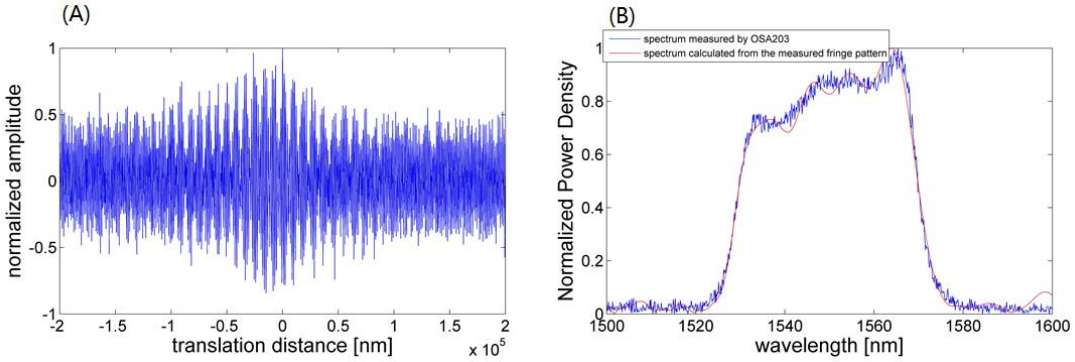

Fig. 70. (A) Fringe patterns of the low-coherent light, and (B) measured and extracted source spectrum with bandpass filter.

Phase response and group delay of a DUT can be individually extracted from the fringe patterns. For instance, Fig. 71 displays the phase and group delay of the bandpass filter in the near-infrared. The phase change near the center wavelength is less than π.

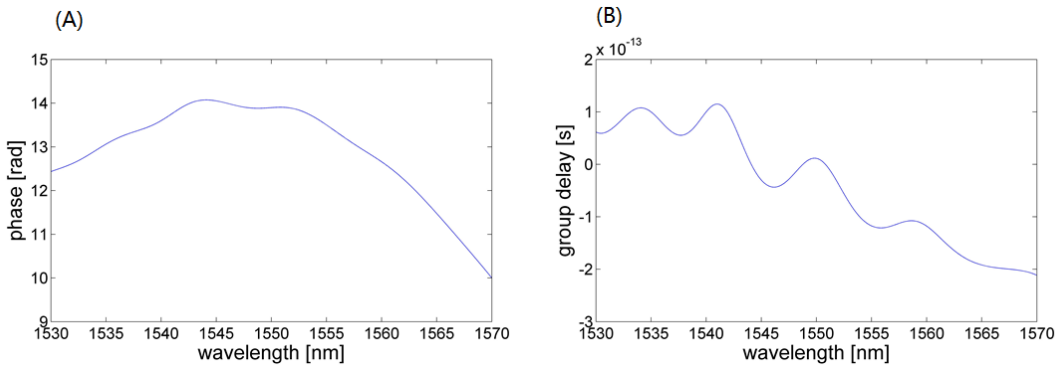

Fig. 71. Experimental measurements of a bandpass filter near 1550 nm: (A) phase response and (B) group delay.

CHAPTER V

CONCLUSION

5.1 Summary

The works in this dissertation have achieved efficient light coupling on As_2S_3-on-$LiNbO_3$ hybrid platform. Compared to a previous coupler that consists of a bus waveguide and a taper mode converter, the coupling method proposed herein requires one lithography step, cutting the fabrication cycle to one third of the previous coupler. The grating coupler developed here demonstrates superior performance to the previous coupler. It is also compatible with the measurement of grating cavity devices.

The As_2S_3 grating coupler on bulk $LiNbO_3$ has been demonstrated for the first time to our knowledge. The coupler loss is 3.75 dB, and it can be further improved through better control of Al_2O_3 layer deposition and sample surface planarization. The measured bandwidth of the grating coupler is approximately 80 nm, which is in good agreement with the simulation result. The fabricated cavity has transmission FWHM of 0.0375 nm at the resonance wavelength, making it a good candidate of optical filter.

The As_2S_3 grating coupler on thin film $LiNbO_3$ is designed, in order to open the door to multiple EO applications with thin film $LiNbO_3$ in the future. The theoretical coupling efficiency can be as high as 78.8% at 1550 nm with 60 nm bandwidth. An alternative grating coupler with a different design is fabricated. While the grating coupler loss could be reduced through further design optimization, the grating cavity reflection response is acquired by time truncation and inverse Fourier transformation. If

the loss of cavity can be reduced through fabrication optimization, smaller FSR with higher extinction ratio optical filter can be constructed. A FIMMWAVE simulation for different As_2S_3 waveguide widths indicates as high as 82.3% optical confinement in $LiNbO_3$ layer can be achieved if the As_2S_3 cavity width is reduced to 0.4 μm. This means that high EO tuning efficiency can be achieved once electrodes are patterned on both sides of the cavity.

An E-field measurement probe is experimentally demonstrated by coupling D-fiber to a slab $LiNbO_3$. The linear wavelength range is 0.2725 nm, with dynamic range of 1.35 MV/m. The sensitivity of the probe is 1.156 μW▪m/MV. The probe is packaged using 3-D printed parts and UV-sensitive epoxy, and then tested using wavelength tunable DFB laser. Within the tuning range (1531.42 – 1531.5 nm), the packaged probe has 29.6% higher sensitivity than the work reported in [62]. This probe can be potentially miniaturized and ready for in-situ E-field measurement once the DFB laser, the photodiode, and the PC are replaced by their miniaturized counterparts.

An OLCI setup is designed and built, and the measurement results are discussed. Within this setup, a low-coherence source is constructed by inserting a 40 nm bandpass filter into the optical path of a supercontinuum source. After inverse Fourier transformation, the source spectrum with the bandpass filter can be calculated, and the phase response of any DUT can also be extracted from the output fringe patterns. The setup has been used for near-IR measurement, and it is also capable of testing mid-IR optical passive devices.

5.2 Future works

The As_2S_3 grating couplers presented in this dissertation still require further optimization to have lower coupling loss and larger bandwidth. According to the current measurement results, the center wavelength of the As_2S_3 grating coupler on thin film $LiNbO_3$ is shifted towards the lower wavelength direction compared with grating coupler simulation. This shift is due to the difference between the actual mode effective refractive index and the simulation value. The mask layout of grating coupler structures can be altered to compensate for this difference.

According to Fimmprop simulation results, 200 μm is above the critical length for 12 μm – 1 μm As_2S_3 taper. Additional test structures should be included into the future patterns to confirm that the taper components do not contribute to overall loss experimentally.

Several techniques can be developed towards better device fabrication capabilities. For instance, new As_2S_3 and Si etching recipes are required in order to fabricate grating coupler structures with higher theoretical coupling efficiency; surface planarization is helpful to reduce grating coupler reflection due to sample surface roughness.

Once the grating coupler structures are optimized to its peak performance, a lot of promising applications are enabled, such as tunable optical filter and EO sensor. A tunable grating cavity filters can be achieved by patterning Al electrodes and applying voltage to the hybrid optical mode. A system-level design can also take advantage of the EO-tuning capabilities of the hybrid mode based on thin film $LiNbO_3$. By altering the

grating coupler design, two dimensional free-space beam-steering at different wavelength regions can be developed.

REFERENCES

[1] *Charles K. Kao - Facts*. Available: http://www.nobelprize.org/nobel_prizes/physics/laureates/2009/kao-facts.html

[2] A. E. Willner, S. Khaleghi, M. R. Chitgarha, and O. F. Yilmaz, "All-optical signal processing," *Journal of Lightwave Technology*, vol. 32, pp. 660-680, 2014.

[3] S. E. Miller, "Integrated optics: an introduction," *Bell System Technical Journal*, vol. 48, pp. 2059-2069, 1969.

[4] N. Gat, "Imaging spectroscopy using tunable filters: a review," in *AeroSense 2000*, 2000, pp. 50-64.

[5] M. Noro, K. Suzuki, N. Kishi, H. Hara, T. Watanabe, and H. Iwaoka, "CO_2/H_2O gas sensor using a tunable Fabry-Perot filter with wide wavelength range," in *Micro Electro Mechanical Systems, 2003. MEMS-03 Kyoto. IEEE The Sixteenth Annual International Conference on*, 2003, pp. 319-322.

[6] K. Van Acoleyen, W. Bogaerts, J. Jágerská, N. Le Thomas, R. Houdré, and R. Baets, "Off-chip beam steering with a one-dimensional optical phased array on silicon-on-insulator," *Optics Letters*, vol. 34, pp. 1477-1479, 2009.

[7] J. K. Doylend, M. Heck, J. T. Bovington, J. D. Peters, L. Coldren, and J. Bowers, "Two-dimensional free-space beam steering with an optical phased array on silicon-on-insulator," *Optics Express*, vol. 19, pp. 21595-21604, 2011.

[8] D. Kwong, A. Hosseini, J. Covey, Y. Zhang, X. Xu, H. Subbaraman, *et al.*, "On-chip silicon optical phased array for two-dimensional beam steering," *Optics Letters*, vol. 39, pp. 941-944, 2014.

[9] D. H. B. F. W. Glaze, J. S. Osmalov, D. Hubbard and M. H. Black, "Properties of arsenic sulfide glass," *Journal of Research of the National Bureau of Standards*, vol. 59, 1957.

[10] A. Zakery and S. R. Elliott, *Optical nonlinearities in chalcogenide glasses and their applications*, vol. 4, Springer, Berlin, 2007.

[11] M. R. Lamont, C. M. de Sterke, and B. J. Eggleton, "Dispersion engineering of highly nonlinear As_2S_3 waveguides for parametric gain and wavelength conversion," *Optics Express*, vol. 15, pp. 9458-9463, 2007.

[12] F. Luan, M. D. Pelusi, M. R. Lamont, D.-Y. Choi, S. Madden, B. Luther-Davies, *et al.*, "Dispersion engineered As_2S_3 planar waveguides for broadband four-wave mixing based wavelength conversion of 40 Gb/s signals," *Optics Express*, vol. 17, pp. 3514-3520, 2009.

[13] Q. Chen, X. Wang, and C. Madsen, "Phase-matching and parametric conversion for the mid-infrared in As_2S_3 waveguides," *Optics and Photonics Journal*, vol. 2, p. 260, 2012.

[14] M. E. S. W. C. Tan, J. Gardner, R. Atkins and C. Madsen, "Optical characterization of α-As_2S_3 thin films prepared by magnetron sputtering," *Journal of Applied Physics*, vol. 107, 2010.

[15] X. Wang, Y. Zhou, and C. K. Madsen, "Fabrication and measurement of sidewall gratings integrated in hybrid As_2S_3-Ti:$LiNbO_3$ optical waveguides," *Journal of Lightwave Technology*, vol. 32, pp. 2989-2995, 2014.

[16] W. T. Snider, "Electro-optically tunable microring resonators for non-linear frequency modulated waveform generation," Doctor of Philosophy Dissertation, Electrical and Computer Engineering, Texas A&M University, College Station 2012.

[17] W. T. Snider, D. D. Macik, and C. K. Madsen, "Electro-optically tunable Mach-Zehnder interferometer on $LiNbO_3$ substrate," *IEEE Photonics Technology Letters*, vol. 24, pp. 1415-1417, 2012.

[18] D. D. Macik and C. K. Madsen, "Fabrication of $LiNbO_3$-As_2S_3 waveguides for beam steering applications," in *SPIE Optical Engineering and Applications*, 2016, pp. 99700H-99700H-10.

[19] M. Lawrence, "Lithium niobate integrated optics," *Reports on Progress in Physics*, vol. 56, p. 363, 1993.

[20] M. N. Polyanskiy. *Refractive Index Database*. Available: http://refractiveindex.info

[21] X. Song, W. Tan, W. Snider, X. Xia, and C. Madsen, "Gain improvement of waveguide amplifier by an overlay waveguide," *IEEE Photonics Journal*, vol. 3, pp. 686-695, 2011.

[22] D. Marcuse, "Loss analysis of single-mode fiber splices," *Bell System Technical Journal*, vol. 56, pp. 703-718, 1977.

[23] M. Dakss, L. Kuhn, P. Heidrich, and B. Scott, "Grating coupler for efficient excitation of optical guided waves in thin films," *Applied Physics Letters*, vol. 16, pp. 523-525, 1970.

[24] D. Taillaert, W. Bogaerts, P. Bienstman, T. F. Krauss, P. Van Daele, I. Moerman, *et al.*, "An out-of-plane grating coupler for efficient butt-coupling between compact planar waveguides and single-mode fibers," *IEEE Journal of Quantum Electronics*, vol. 38, pp. 949-955, 2002.

[25] D. Taillaert, P. Bienstman, and R. Baets, "Compact efficient broadband grating coupler for silicon-on-insulator waveguides," *Optics Letters*, vol. 29, pp. 2749-2751, 2004.

[26] F. Van Laere, T. Claes, J. Schrauwen, S. Scheerlinck, W. Bogaerts, D. Taillaert, *et al.*, "Compact focusing grating couplers for silicon-on-insulator integrated circuits," *IEEE Photonics Technology Letters*, vol. 19, pp. 1919-1921, 2007.

[27] M. E. Solmaz, D. B. Adams, S. Grover, W. Tan, X. Xia, O. Eknoyan, *et al.*, "First demonstration of an As_2S_3-on-$LiNbO_3$ ring resonator," in *Optical Fiber Communication Conference*, 2009, p. OWV7.

[28] Y. Zhou, X. Xia, W. T. Snider, J. Kim, Q. Chen, W. C. Tan, *et al.*, "Two-stage taper enhanced ultra-high as S ring resonator on $LiNbO_3$," *IEEE Photonics Technology Letters*, vol. 23, pp. 1195-1197, 2011.

[29] X. Wang and C. K. Madsen, "Design of a hybrid As_2S_3-Ti: $LiNbO_3$ optical waveguide for phase-matched difference frequency generation at mid-infrared," *Optics Express*, vol. 22, pp. 27183-27192, 2014.

[30] X. Wang and C. K. Madsen, "Highly sensitive compact refractive index sensor based on phase-shifted sidewall Bragg gratings in slot waveguide," *Applied Optics*, vol. 53, pp. 96-103, 2014.

[31] A. Guarino, G. Poberaj, D. Rezzonico, R. Degl'Innocenti, and P. Günter, "Electro–optically tunable microring resonators in lithium niobate," *Nature Photonics,* vol. 1, pp. 407-410, 2007.

[32] "Refractive index," in *Wikipedia, The Free Encyclopedia*. Available: https://en.wikipedia.org/wiki/Refractive_index

[33] "Sellmeier equation," in *Wikipedia, The Free Encyclopedia* vol. 2016. Available: https://en.wikipedia.org/wiki/Sellmeier_equation

[34] "Corning SMF-28 Ultra Optical Fiber," Corning. Available: https://www.corning.com/media/worldwide/coc/documents/Fiber/SMF-28%20Ultra.pdf

[35] X. Wang, "Design and fabrication of integrated optical waveguides and sidewall bragg gratings," Doctor of Philosophy Dissertation, Electrical and Computer Engineering, Texas A&M University, College Station 2014.

[36] F. Grillot, L. Vivien, S. Laval, D. Pascal, and E. Cassan, "Size influence on the propagation loss induced by sidewall roughness in ultrasmall SOI waveguides," *IEEE Photonics Technology Letters,* vol. 16, pp. 1661-1663, 2004.

[37] G. Roelkens, D. Van Thourhout, and R. Baets, "High efficiency silicon-on-insulator grating coupler based on a poly-silicon overlay," *Optics Express,* vol. 14, pp. 11622-11630, 2006.

[38] A. Yariv and P. Yeh, *Optical waves in crystals: propagation and control of laser radiation*, vol. 2, John Wiley and Sons, Inc., New York, 1983.

[39] L. Chrostowski and M. Hochberg, *Silicon Photonics Design: From Devices to Systems*, vol. 4, Cambridge University Press, 2015.

[40] D. Marcuse, *Theory of dielectric optical waveguides*, vol. 3, Academic Press, New York, 2013.

[41] C. K. Madsen and J. H. Zhao, *Optical filter design and analysis: a signal processing approach*, vol 7, John Wiley & Sons, Inc., New York, 1999.

[42] "NANO PMMA and Copolymer," MicroChem. Available: http://microchem.com/pdf/PMMA_Data_Sheet.pdf

[43] L. Chang. *Welcome to Pythography*. Available: http://www.pythography.com/Roca/beamDrift.html

[44] R. Paschotta, "Finesse," in *Encyclopedia of Laser Physics and Technology*. Available: https://www.rp-photonics.com/finesse.html

[45] I. Kaminow, J. Carruthers, E. Turner, and L. Stulz, "Thin film $LiNbO_3$ electro-optic light modulator," *Applied Physics Letters*, vol. 22, pp. 540-542, 1973.

[46] T. A. Ramadan, M. Levy, and R. Osgood, "Electro-optic modulation in crystal-ion-sliced z-cut $LiNbO_3$ thin films," *Applied Physics Letters*, vol. 76, p. 1407, 2000.

[47] H. Lu, B. Sadani, N. Courjal, G. Ulliac, N. Smith, V. Stenger, *et al.*, "Enhanced electro-optical lithium niobate photonic crystal wire waveguide on a smart-cut thin film," *Optics Express*, vol. 20, pp. 2974-2981, 2012.

[48] M. Levy, R. Osgood, R. Liu, L. Cross, G. Cargill, A. Kumar, *et al.*, "Fabrication of single-crystal lithium niobate films by crystal ion slicing," *Applied Physics Letters,* vol. 73, 1998.

[49] R. Geiss, A. Sergeyev, H. Hartung, A. S. Solntsev, A. A. Sukhorukov, R. Grange, *et al.*, "Fabrication of free-standing lithium niobate nanowaveguides down to 50 nm in width," *Nanotechnology,* vol. 27, p. 065301, 2015.

[50] F. Niklaus, P. Enoksson, E. Kälvesten, and G. Stemme, "Low-temperature full wafer adhesive bonding," *Journal of Micromechanics and Microengineering,* vol. 11, p. 100, 2001.

[51] F. Niklaus, H. Andersson, P. Enoksson, and G. Stemme, "Low temperature full wafer adhesive bonding of structured wafers," *Sensors and Actuators A: Physical,* vol. 92, pp. 235-241, 2001.

[52] "Processing Procedures for BCB Adhesion," DOW. Available: http://www.dow.com/cyclotene/docs/bcb_adhesion.pdf

[53] "Polarization Analyzers Series," Schafer Kirchhoff. Available: http://www.sukhamburg.com/download/polAnalyzer_e.pdf

[54] "Polarization (waves)," in *Wikipedia, The Free Encyclopedia*. Available: https://en.wikipedia.org/wiki/Polarization_(waves)

[55] B. Wang, R. Zeng, B. Niu, X. Li, and J. Yu, "Sensitivity improvement of integrated optical E-field sensor based on common path interferometer," in *Sensors, 2012 IEEE,* pp. 1-5, 2012.

[56] P. Tien and R. Ulrich, "Theory of prism–film coupler and thin-film light guides," *JOSA,* vol. 60, pp. 1325-1337, 1970.

[57] P. Tien, "Light waves in thin films and integrated optics," *Applied Optics,* vol. 10, pp. 2395-2413, 1971.

[58] R. Ulrich and R. Torge, "Measurement of thin film parameters with a prism coupler," *Applied Optics,* vol. 12, pp. 2901-2908, 1973.

[59] S.M. Tseng and C.L. Chen, "Side-polished fibers," *Applied Optics,* vol. 31, pp. 3438-3447, 1992.

[60] R. Gibson, J. Kvavle, R. Selfridge, and S. Schultz, "Improved sensing performance of D-fiber/planar waveguide couplers," *Optics Express,* vol. 15, pp. 2139-2144, 2007.

[61] R. Gibson, R. Selfridge, S. Schultz, W. Wang, and R. Forber, "Electro-optic sensor from high Q resonance between optical D-fiber and slab waveguide," *Applied Optics,* vol. 47, pp. 2234-2240, 2008.

[62] R. Gibson, R. Selfridge, and S. Schultz, "Electric field sensor array from cavity resonance between optical D-fiber and multiple slab waveguides," *Applied Optics,* vol. 48, pp. 3695-3701, 2009.

APPENDIX A

MATLAB CODE FOR EIM

```
clc;
clear all;
close all;
% Calculate effective refractive index @ 1550 nm
% Database: refractiveindex.info
%=====Define wavelength=====
lambda0=1.55; %unit: um
k0=2*pi/lambda0;
lam1=1.5;
lam2=1.6;
spectral_resolution=0.001;
nlam=(lam2-lam1)/spectral_resolution;
lambda=lam1:spectral_resolution:lam2;
k=2*pi./lambda;
%=====Material Database=====
% LiNbO3(o) [0.4, 5.0] um
noLiNbO3=sqrt(1+2.6734./(1-0.01764./lambda.^2)+1.2290./(1-
0.05914./lambda.^2)+12.614./(1-474.60./lambda.^2));
% LiNbO3(e) [0.4, 5.0] um
```

```
neLiNbO3=sqrt(1+2.9804./(1-0.02047./lambda.^2)+0.5981./(1-
0.0666./lambda.^2)+8.9543./(1-416.08./lambda.^2));
%As2S3(amorphous) [0.57, 11.8] um
nAs2S3=sqrt(1+1.8983678./(1-0.0225./lambda.^2)+1.9222979./(1-
0.0625./lambda.^2)+0.8765134./(1-0.1225./lambda.^2)+0.1188704./(1-
0.2025./lambda.^2)+0.9569903./(1-750./lambda.^2));
%Si [1.357, 11.04] um
nSi=sqrt(1+10.6684293./(1-(0.301516485./lambda).^2)+0.0030434748./(1-
(1.13475115./lambda).^2)+1.54133408./(1-(1104./lambda).^2));
%SiO2 [0.21, 3.71] um
nSiO2=sqrt(1+0.6961663./(1-(0.0684043./lambda).^2)+0.4079426./(1-
(0.1162414./lambda).^2)+0.8974794./(1-(9.896161./lambda).^2));
%Al2O3(o) [0.2, 5.0] um
noAl2O3=sqrt(1+1.4313493./(1-(0.0726631./lambda).^2)+0.65054713./(1-
(0.1193242./lambda).^2)+5.3414021./(1-(18.028251./lambda).^2));
%Al2O3(e) [0.2, 5.0] um
neAl2O3=sqrt(1+1.5039759./(1-(0.0740288./lambda).^2)+0.55069141./(1-
(0.1216529./lambda).^2)+6.5927379./(1-(20.072248./lambda).^2));
% plot(lambda,noAl2O3);
%=====Define GC geometry=====
N=1000;
ff=0.3:0.05:0.7;
```

```
t=0.5; % waveguide thickness, unit: um
w=1.0; % waveguide width, unit: um
n_TE=zeros(1,nlam);
n_TM=n_TE;
hmin=0.01;
for t=0.4:0.05:0.5
   for r=1:nlam+1
      n1=nSiO2(1,r);
      n2=nAs2S3(1,r);
      n3=noAl2O3(1,r);
      k0=k(1,r);
      %=====Effective index of TE0=====
      hmax1=k0*sqrt(n2^2-n3^2)-hmin;
      h1=hmin:(hmax1-hmin)/N:hmax1;
      q1=sqrt(k0^2*(n2^2-n1^2)-h1.^2);
      p1=sqrt(k0^2*(n2^2-n3^2)-h1.^2);
      LHS1=tan(t*h1);
      RHS1=(q1+p1)./(h1-q1.*p1./h1);
      diff=100;
      for i=1:N
         if (abs(LHS1(i)-RHS1(i))<diff)&&(h1(1,i)*t>pi/2)&&(h1(1,i)*t<pi*3/2)
            % Guarantee fundamental mode
```

```
        % Need to refine the solution to the transcendental equation
        diff=abs(LHS1(i)-RHS1(i));
        diffx1=hmin+(hmax1-hmin)*i/N;
    end
    if diff<50/N
        break
    end
end
neff1_TE0=sqrt(k0^2*n2^2-diffx1^2)/k0;
hmax2=k0*sqrt(neff1_TE0^2-n1^2)-hmin;
h2=hmin:(hmax2-hmin)/N:hmax2;
q2=(neff1_TE0/n1)^2*sqrt(k0^2*(neff1_TE0^2-n1^2)-h2.^2);
p2=q2;
LHS2=tan(w*h2);
RHS2=(q2+p2)./(h2-q2.*p2./h2);
diff=100;
for i=1:N
    if (abs(LHS2(i)-RHS2(i))<diff)&&(h2(1,i)*w>pi/2)&&(h2(1,i)*w<pi*3/2)
        diff=abs(LHS2(i)-RHS2(i));
        diffx2=hmin+(hmax2-hmin)*i/N;
    end
    if diff<50/N
```

```
        break
    end
end
neff_TE0=sqrt(k0^2*neff1_TE0^2-diffx2^2)/k0;
%=====Effective index of TM0=====
hmax3=k0*sqrt(n2^2-n1^2)-hmin;
h3=hmin:(hmax3-hmin)/N:hmax3;
q3=(n2/n1)^2*sqrt(k0^2*(n2^2-n1^2)-h3.^2);
p3=(n2/n3)^2*sqrt(k0^2*(n2^2-n3^2)-h3.^2);
LHS3=tan(t*h3);
RHS3=(q3+p3)./(h3-q3.*p3./h3);
diff=100;
for i=1:N
    if (abs(LHS3(i)-RHS3(i))<diff)&&(h3(1,i)*t>pi/2)&&(h3(1,i)*t<pi*3/2)
        diff=abs(LHS3(i)-RHS3(i));
        diffx3=hmin+(hmax3-hmin)*i/N;
    end
    if diff<50/N
        break
    end
end
neff1_TM0=sqrt(k0^2*n2^2-diffx3^2)/k0;
```

```
    hmax4=k0*sqrt(neff1_TM0^2-n1^2)-hmin;
    h4=hmin:(hmax4-hmin)/N:hmax4;
    q4=sqrt(k0^2*(neff1_TM0^2-n1^2)-h4.^2);
    p4=q4;
    LHS4=tan(w*h4);
    RHS4=(q4+p4)./(h4-q4.*p4./h4);
    diff=100;
    for i=1:N
        if (abs(LHS4(i)-RHS4(i))<diff)&&(h4(1,i)*w>pi/2)&&(h4(1,i)*w<pi*3/2)
           diff=abs(LHS4(i)-RHS4(i));
           diffx4=hmin+(hmax4-hmin)*i/N;
        end
        if diff<50/N
            break
        end
    end
    neff_TM0=sqrt(k0^2*neff1_TM0^2-diffx4^2)/k0;
    n_TE(1,r)=neff_TE0;
    n_TM(1,r)=neff_TM0;
end
neff=neff1_TE0*ff+1.444*(1-ff);
period=1.550./(neff-1.444*sind(17));
```

```
    plot(ff,period);
    hold on;
end
% figure;
% plot(lambda(1,:),n_TE(1,:));
% hold on;
% plot(lambda(1,:),n_TM(1,:),'r');
% xlim([lam1,lam2]);
% ylim([nSiO2(1,1),nAs2S3(1,1)]);
% figure;
% plot(lambda(1,:),nSi,lambda(1,:),nSiO2,lambda(1,:),k);
```

APPENDIX B

PYTHON SCRIPT INTERFACING WITH FIMMPROP

```
from pdPythonLib import *
import math
import cmath
fimm = pdApp()
fimm.ConnectToApp("127.0.0.1",5101)
alpha = 14                                  # tilt angle of the fiber in degrees
FPpath = "app.subnodes[1].subnodes[11]"     # path of the FIMMPROP Device
Zmax = 20+15*0.85                           # length of FP Device
nx = 200                                    # nx for the cross-section
W = 20                                      # width of cross-section
xpos = -5                                   # x-position at which the overlap is calculated
Zsteps = 1001               # MUST BE ODD INTEGER
Zscansteps = 1000           # number of points for the scanning of the centre of the
Gaussian beam
Zscanmin = 0                # min Z value for centre of Gaussian beam
Zscanmax = Zmax             # min Z value for centre of Gaussian beam
alpha_rad = alpha/180.*cmath.pi
dZ = Zmax/(Zsteps-1)/math.cos(alpha_rad)
def overlap(Ey,MFD,Z0,Zsteps,dZ):
```

```
    integral = 0
    for i in range (1,Zsteps,2):
        integral = integral + dZ/3*(Ey[i-1]*math.exp(-((Z0-(i-
1)*dZ)/sigma)**2)+4*Ey[i]*math.exp(-((Z0-i*dZ)/sigma)**2)+Ey[i+1]*math.exp(-
((Z0-(i+1)*dZ)/sigma)**2))
    return integral
### Main script ###
wav = 1.55
MFD = 10.4
sigma = MFD/2.0
p=[0.85]
p1=[0.75]
p3=[0.7]
p5=[0.6]
pu1=[0.5]
f1 = open ('Apodized TFLN GC Opt 0627.txt','w')
print "0" + "  efficiency" + "   period" + "    p1" + "   p3" + "   p5" + "   pu1"
f1.write("etamax\t")
f1.write("Z0opt\t")
f1.write("period\t")
f1.write("p1\t")
f1.write("p3\t")
```

```
f1.write("p5\t")
f1.write("pu1\t")
f1.write('\n')
counter = 0
Np = 16 #2*3+10
#sangle = [14]
for ip in range (0,len(p)):
    for ip1 in range (0,len(p1)):
        for ip3 in range (0,len(p3)):
            for ip5 in range (0,len(p5)):
                for ipu1 in range (0,len(pu1)):
                    alpha_rad = alpha/180.*cmath.pi
                    dZ = Zmax/(Zsteps-1)/math.cos(alpha_rad)
                    counter = counter + 1
                    Zmax = 20.0+p[ip]*Np
                    Zscanmax = Zmax
                    dZ = Zmax/(Zsteps-1)/math.cos(alpha_rad)
                    fimm.Exec("app.subnodes[1].subnodes[1].setvariable(period,{p[ip]})")
                    fimm.Exec("app.subnodes[1].subnodes[1].setvariable(p1,{p1[ip1]})")
                    fimm.Exec("app.subnodes[1].subnodes[1].setvariable(p3,{p3[ip3]})")
                    fimm.Exec("app.subnodes[1].subnodes[1].setvariable(p5,{p5[ip5]})")
                    fimm.Exec("app.subnodes[1].subnodes[1].setvariable(pu1,{pu1[ipu1]})")
```

```
        fimm.Exec("{FPpath}.update")
        ### Input power calculation ###
        Powerin = 0
        fimm.Exec("{FPpath}.calcfieldprofile(0,1,1,0)")
    # Calcfieldprofile: stores field Xsection in fieldprofile. refpt,refelt default to 0,0
        fimm.Exec("Set field = {FPpath}.fieldprofile.getfieldarray(2)")
        inputEy = fimm.Exec("field.fieldarray")
        fimm.Exec("Set field = {FPpath}.fieldprofile.getfieldarray(4)")
        inputHx = fimm.Exec("field.fieldarray") #given in mA/m
        for i in range (0,int(nx),1):
            inputHx[i][0]=inputHx[i][0]/1000 #now given in A/m
        for i in range (1,nx+1,2):
            Powerin = Powerin + W/float(nx)/3*(inputEy[i-1][0]*inputHx[i-
1][0]+4*inputEy[i][0]*inputHx[i][0]+inputEy[i+1][0]*inputHx[i+1][0])
        Powerin = math.sqrt(Powerin.real**2+Powerin.imag**2)
        ### Output power calculation ###
        Powerout = 0
        EyIntegral = 0
        fimm.Exec("{FPpath}.calczfield({Zsteps},0,{Zmax},{xpos},0,1)")
        Ey = fimm.Exec("{FPpath}.zfieldcomp.EyTotal") # first term Ey[0] is None
        Ey = Ey[1:] # Ey[0] -> z = 0, Ey[i] -> z = i*Zmax/(Zsteps-1)
        Hz = fimm.Exec("{FPpath}.zfieldcomp.HzTotal")
```

```
            # first term Ey[0] is None
        Hz = Hz[1:] #Unit conversion: A/m
        if not alpha == 0: # if there is tilt we need to project the field profile
            for i in range (0,len(Ey),1):
            # we introduce a phase shift of 2*pi*(zmax-z)*tan(alpha)/wav
                Ey[i] = Ey[i]*cmath.exp(cmath.pi*2j*Zmax*(len(Ey)-i-1)/(len(Ey)-
1)*math.tan(alpha_rad)/wav)
                Hz[i] = Hz[i]*cmath.exp(cmath.pi*2j*Zmax*(len(Hz)-i-1)/(len(Hz)-
1)*math.tan(alpha_rad)/wav)
        for i in range (1,len(Ey),2):
            Powerout = Powerout + dZ/3*(Ey[i-1]*Hz[i-
1]+4*Ey[i]*Hz[i]+Ey[i+1]*Hz[i+1])
            EyIntegral = EyIntegral + dZ/3*(Ey[i-
1].real**2+4*Ey[i].real**2+Ey[i+1].real**2+Ey[i-
1].imag**2+4*Ey[i].imag**2+Ey[i+1].imag**2)
        Powerout = math.sqrt(Powerout.real**2+Powerout.imag**2)
        ### Overlapping Integral Calculation ###
        etamax = 0
        Z0opt = 0
        for j in range (0,Zscansteps,1):
            Z0 = Zscanmin+j*(Zscanmax-Zscanmin)/(Zscansteps-1)
            OV = overlap(Ey,MFD,Z0,Zsteps,dZ)
```

```
                GaussianIntegral = 0
                for i in range (1,Zsteps,2):
                    GaussianIntegral = GaussianIntegral + dZ/3*(math.exp(-2*((Z0-(i-
1)*dZ)/sigma)**2)+4*math.exp(-2*((Z0-i*dZ)/sigma)**2)+math.exp(-2*((Z0-
(i+1)*dZ)/sigma)**2))
#                   eta = (Powerout/Powerin)
                eta =
Powerout/Powerin)*((OV.real**2+OV.imag**2)/(GaussianIntegral*EyIntegral))
                if (eta>etamax):
                    etamax = eta
                    eta1 = Powerout/Powerin
                    eta2 = (OV.real**2+OV.imag**2)/(GaussianIntegral*EyIntegral)
                    Z0opt = Z0
            ### Data Output ###
            print str(counter) + "  " + str(etamax) + "   " + str(p[ip]) + "   " + str(p1[ip1])
+ "   " + str(p3[ip3]) + "   "  + str(p5[ip5]) + "   " + str(pu1[ipu1])
            f1.write(str(etamax))
            f1.write('\t')
            f1.write(str(Z0opt))
            f1.write('\t')
            f1.write(str(p[ip]))
            f1.write('\t')
```

```
                f1.write(str(p1[ip1]))
                f1.write('\t')
                f1.write(str(p3[ip3]))
                f1.write('\t')
                f1.write(str(p5[ip5]))
                f1.write('\t')
                f1.write(str(pu1[ipu1]))
                f1.write('\n')
f1.close()
del fimm
```

APPENDIX C

EBL STEP-BY-STEP PROCEDURE

0. Preparations before logging in: Take the resist bottle out of the fridge and let it sit at the room temperature for at least 10 min. Spin-coat the samples (2500rpm for 1 min) and soft-bake them for 2 min at 180 °C on a hotplate. Load the first sample in the chamber.

1. Log in → Pattern designer → Convert the GDSII file into .v30 file

2. Select → Select → "M4_A2_1nA" (Note: it takes 2 hours to stabilize after the mode switch)

3. Calibration→ Main Tab→ "M4_A2_1nA" → Load → Execute → Restore

4. FC→ Move → Beam On → Adjust LENS2/3 value to make the value 1nA → Beam off (Note: the initial current value should be very close to 1nA, unless something is wrong.)

5. BE → Move → SE image → Center BE mark → Wobble adjustment (Table 4) → Center BE mark again → Entry & BE (if BE coordinates have been changed) → Beam Off (Note: BE mark is for deflection correction)

6. AE → Move → Beam On → Center AE mark → Entry & AE (if AE coordinates have been changed) → Beam off (Note: AE mark is for auto-focusing)

7. Calibration → Std. Mark Detection Tab → Check "Current Measurement", "Std. Mark Detection", "Automatic Focusing" and "Deflection Correction" boxes on the left; check "AE mark" and "BE mark" on the right → Execute → Deselect (after calibration is finished) → Apply parameters → Close & Save

Note: Step 1-7 are only carried out for the first run.

8. Alignment (refer to section 3.2.4 Alignment)

9. Move to the focus mark → Adjust focus value to make the best focus (Table 4)

10. Calibration → Std. Mark Detection Tab → Check “Current Measurement”, “Std. Mark Detection”, and “Deflection Correction” boxes on the left; check “BE mark” on the right → Execute → Deselect (after calibration is finished) → Apply parameters → Close & Save

11. Expose (refer to section 3.2.6 Exposure for parameters) → Beam off (after exposure is finished)

12. Repeat step 2 for the next user and log off